UTS UNIVERSITY OF TECHNOLOGY SYDNEY

Real-Time Extraction of Stiffness of Layered Granular Soil Using Machine Learning Considering Dynamic Soil-Roller Interaction for Intelligent Compaction

by Zhengheng Xu

Thesis submitted in fulfilment of the requirements for the degree of

Doctor of Philosophy

under the supervision of Prof. Hadi Khabbaz, A/Prof. Behzad Fatahi and Dr. Di Wu

University of Technology Sydney
Faculty of Engineering and Information Technology

August 2023

Certificate of Original Authorship

I, *Zhengheng Xu*, declare that this thesis, is submitted in fulfilment of the requirements for the award of *the degree of Doctor of Philosophy*, in the *School of Civil and Environmental Engineering, Faculty of Engineering and Information Technology* at the University of Technology Sydney.

This thesis is wholly my own work unless otherwise referenced or acknowledged. In addition, I certify that all information sources and literature used are indicated in the thesis. This document has not been submitted for qualifications at any other academic institution.

This research is supported by the Australian Government Research Training Program.

Signature: Production Note:
Signature removed prior to publication.

Date: 01/08/2023

To my father, mother and family, who gave me the life and strength

To my friends, who encouraged me throughout the journey

And

To Yiwei, who taught me the meaning of love.

“我相信你们的爱。”

Acknowledgements

Writing this dissertation has been a meaningful experience when it recollects four years of my challenging journey, but highly enjoyable. I would like to take this opportunity to express my sincere gratitude and appreciation to those who encouraged and supported me throughout my PhD study.

Firstly, I am very indebted to my thoughtful supervisors, Professor Hadi Khabbaz and Associate Professor Behzad Fatahi, who gave me an opportunity to pursue a PhD, and continuously supported, guided, and accompanied me throughout the journey. They lived by example and compelled me to feel the world through unique perspectives. I would also like to sincerely appreciate my co-supervisor, Dr Di Wu, for his technical assistance and encouragement whenever possible.

I also wish to express my deep appreciation to my friends and colleagues for sharing their experiences and friendship. Besides, I convey my special thanks to Alex Dong and Ruby Kang for their kind assistance during these memorable times. In addition, I am grateful to Ms. Van Le, Dr Larissa Koroleva and other administrative staff, who committedly assisted me during my study in the School of Civil and Environmental Engineering at UTS.

I would like to extend my heartfelt gratitude to my beloved family. Despite not having the opportunity to be in my hometown for over three years because of the pandemic, their thoughtful kindness and invaluable support have been instrumental in helping me achieve this significant milestone. I am also deeply thankful to my partner, Yiwei Gu, for her unwavering and constant spiritual support, making her my most reliable ally throughout this journey. Without the love and encouragement from my family and Yiwei, the completion of this work would not have been possible.

Finally, I would also like to take a moment to pay tribute to my late grandfather, who peacefully passed away in June 2023. His love and encouragement have played a vital role in shaping the person I am today. He served as a constant source of inspiration, instilling in me the value of staying curious about knowledge and embracing lifelong learning. My grandpa's memory will forever hold a special place in my heart, guiding me throughout all my life and career endeavors. I am eternally grateful for the profound impact he had in my life.

List of Publications

Journal Articles

- **Xu, Z.**, Khabbaz, H., Fatahi, B. and Wu, D., 2023. Double-layered granular soil modulus extraction for intelligent compaction using extended support vector machine learning considering soil-structure interaction. *Engineering Structures*, *274*, p.115180.

- **Xu, Z.**, Khabbaz, H., Fatahi, B. and Wu, D., 2022. Real-time determination of sandy soil stiffness during vibratory compaction incorporating machine learning method for intelligent compaction. *Journal of Rock Mechanics and Geotechnical Engineering*, *14*(5), pp.1609-1625.

Conference Papers or Book Chapters

- **Xu, Z.**, Khabbaz, H., Fatahi, B., Lee, J. and Bhandari, S., 2022. Numerical Assessment of Impacts of Vibrating Roller Characteristics on Acceleration Response of Drum Used for Intelligent Compaction. In *Advances in Transportation Geotechnics IV* (pp. 231-245). Springer, Cham.

- Bhandari, S., Fatahi, B., Khabbaz, H., Lee, J., **Xu, Z.** and Zhong, J., 2022. Evaluating the Influence of Soil Plasticity on the Vibratory Roller—Soil Interaction for Intelligent Compaction. In *Advances in Transportation Geotechnics IV* (pp. 247-260). Springer, Cham.

Table of Contents

List of Figures

List of Tables

List of Symbols

A	Measured vibration amplitude
$A_{0.5\Omega}$	Sub-harmonic acceleration amplitude
B	Contact width of the interaction between the soil and drum
b	Internal loss coefficient of machine
C	Constant value which is used to calculate CMV, and commonly selected as 300
C_1	Relaxation coefficient where C_1 = 1 in this study
C_2	Relaxation coefficient where C_2 = 1 in this study
C_p	P-wave velocity
C_s	S-wave velocity
c	Soil cohesion
c_f	Suspension damping (MNs/m)
c_i	Cohesion of interface
c_{ref}	Reference cohesion
c_s	Cohesion of soil
D	Diameter of compacted drum
$\hat{d}$	Order of the polynomial
E_{50}	Primary deviatoric loading (kPa)
E_{50}^{ref}	Secant stiffness related to the reference pressure (p^{ref} = 100 kPa)
E_D	Dissipated energy
E_{loss}	Energy loss which is used to calculate machine drive power
E_n	Modulus of the subgrade layer
E_{oed}	Tangent stiffness modulus from an oedometer test (kPa)

E_{oed}^{ref}	Tangent stiffness related to the reference pressure (p^{ref}= 100 kPa)
E_S	Cyclic maximum strain energy in a single load cycle
E_{ur}	Unloading and reloading stress-depend stiffness (kPa)
E_{ur}^{ref}	Unloading-reloading stiffness related to the reference pressure
e_0	Arm of the rotating mass
err_{ϑ}	Mean squared error
F_c	Drum-soil system contact force (kN)
F_{ecc}	Centrifugal force (kN)
f	Frequency of vibratory drum
G	Shear modulus
G_0	Small-strain shear stiffness
G_0^{ref}	Shear modulus at the reference pressure p^{ref} (p^{ref}= 100 kPa)
G_i	Shear modulus of interface
G_s	Secant shear stiffness
G_{soil}	Shear modulus of soil
G_t	Small strain tangent shear modulus
G_{ur}	Unloading-reloading shear modulus
g	Gravitational acceleration (9.81 m/s2)
H	Symmetric tensor utilised to show the material's deviatoric strain history
H_{CMV}^k	Thickness of compacted geomaterial in CMV
$\boldsymbol{I}$	Identity matrix
I_1	Primary invariant stress tensor
i	Wheel slippage
J_2	Second invariant stress tensor

K_0^{nc}	Stress ratio in primary compression
k	Model parameter determined from the triaxial shear tests
$\hat{k}$	Predicted soil stiffness
k_c	Fictional modulus
k_f	Suspension stiffness (MN/m)
k_n	Roller-measured stiffness
$\hat{k}_n$	Finite element model predicted stiffness
k_s	roller-integrated stiffness introduced by Ammann
k_φ	Cohesion of soil settlement
L	Length of the drum
l	Horizontal distance rolling by roller
M	Mass of the roller
M_R	Resilient modulus
m	Power for the stress-level dependency of the soil stiffness
m_0	Equipment rotating mass (kg)
m_d	Drum mass (kg)
m_f	Frame mass (kg)
m_r	Roller mass (kg)
N_c	Minimum number of loading cycles
n	Exponent of the soil sinkage
$n_{CMV}^{k,t}$	Passes of the cyclic rolling in CMV
P_a	Atmospheric pressure
P_g	Minimum required total energy to facilitate the roller movement
P_{ml}	Internal machine power loss

P_s	Portion of the power applied to overcome resistance
P_{sa}	Additional machine power
p^{ref}	Reference pressure (p^{ref} = 100 kPa)
q	Deviatoric stress
R	Radius of the vibrated drum
R^2	Coefficient of determination
R_{el}	Ratio of eccentric mass to drum length
R_f	Failure ratio
R_{inter}	Interface strength reduction factor
R_{ml}	Ratio of roller mass to drum length
s	Number of samples
T	One period for calculating the peak interaction force between drum and soil
T_i	Minimum input working period for superior machine learning precision
t	Time (s)
t_{CMV}	Compaction roller passing time in CMV
$t_{l.o.c}$	Loss of contact time between the soil and drum during one period T
t_n	Tractions in the normal direction
t_s	Tractions in the shear direction
$\dot{u}^{ff}$	Soil particle velocities in the free-field
$\dot{u}^{m}$	Soil particle velocities in the main element
V_n	Normal component of velocity
V_s	Shear component of velocity

v_{CMV}^{t}	Speed of the compaction roller in CMV
W	Weight of roller which is used to calculate compacted distance in MDP
$\boldsymbol{w}$	Support vector
$\boldsymbol{x}$	Column vector of input variables
y	Values of benchmark
$\hat{y}$	Prediction
$\overline{y}$	Mean of the true values
$Z_{CMV}^{k,0}$	Initial elevation of compacted grid in CMV
$Z_{CMV}^{k,1}$	Final elevation of compacted grid in CMV
z	Sinkage depth
z_d	Displacement of drum
$\dot{z}_d$	Velocity of drum
$\ddot{z}_d$	Acceleration of drum
z_f	Displacement of frame
$\dot{z}_f$	Velocity of frame
$\ddot{z}_f$	Acceleration of frame
z_{CMV}^{t}	Elevation at time t_{CMV}

Greek Symbols

α	Constant value (α = 0.385)
α_i	Numerical model coefficient ($\alpha_i = 0.25$ is employed in this study)
β_i	Numerical model coefficient ($\beta_i = 0.50$ is employed in this study)
$\Gamma(\bullet)$	Gamma function
$\gamma_{0.7}$	Shear strain at which the secant shear modulus G_s is reduced to 0.7 G_0
γ_c	Shear strain
δ	Bias
δ_{ij}	Kronecker delta
ε_1	Vertical strain
ε_x	Normal strain along the x-axis
ε_z	Normal strain along the z-axis
θ	Interface contact angle
$\widehat{\boldsymbol{\kappa}}(\boldsymbol{x}_i)$	The i-th training sample for constructing the learning model
ξ	Hysteretic damping ratio
$\boldsymbol{\xi}^*$	Negative vector in support vector regression
ξ_i	Allowable negative deviation
ξ_i^*	Positive excessive deviation
ρ	Density of medium
σ_1	Greatest stress in Drucker-Prager model
σ_2	Intermediate stress in Drucker-Prager model
σ_3	Minor principal stress
σ_h	Horizontal stress

σ_{ij}^{dev}	Stress sensor in Drucker-Prager model
σ_n	Effective normal stress
σ_t	Tensile strength
σ_v	Vertical stress
σ_x	Normal stress along the x-axis
σ_z	Normal stress along the z-axis
τ_{oct}	Octahedral shear stress
τ_s	Shear stress
τ_{xz}	Shear strain in the $x-z$ plane
v	Poisson's ratio
$\boldsymbol{\Phi}(\boldsymbol{x}_i)$	Implicit mapping function
$\boldsymbol{\varphi}$	Lagrange multiplier vector
φ	Friction angle
φ_i	Friction angle of interface
φ_s	Friction angle of soil
φ_{soil}	Failure-peak value of φ in HS-Small model
ψ_i	Dilation angle of interface
ψ_{soil}	Dilation angle of soil
ω	Angular frequency (Hz)
$\|\bullet\|_2$	L2-norm of $\bullet$

List of Acronyms

ANN	Artificial neural network
BEM	Boundary element model
BO	Bayesian optimisation
CCC	Continuous compaction control
CCV	Compaction control value
CDF	Cumulative distribution function
CMV	Compaction meter value
CNN	Convolutional neural network
CPT	Cone penetration
CV	Cross validation
DCP	Dynamic cone penetrometer
DEM	Discrete element model
DOM	Degree of freedom
Dr-SVM	Doubly regularised support vector machine
EI	Expected improvement
FEM	Finite element model
FWD	Falling weight deflectometer
GA	Genetic algorithm
GGK	Generalised Gegenbauer kernel
GP	Gaussian process
GPRS	General packet radio service
GPS	Global positioning system
KKT	Karush-Kuhn-Tucker
PDF	Probability density function

HS	Hardening soil model
HS-Small	Hardening soil with small strain model
IC	Intelligent compaction
ICMV	Intelligent compaction meter value
LWD	Light weight deflectometer
MDP	Machine drive power
MEPDG	Mechanistic-empirical pavement design guide
MLP	Multi-layer perceptron
MV	Measurement value
NCHRP	National cooperative highway research program
NDT	Non-destructive testing
NN	Neural network
PDA	Personal digital assistant
QC	Quality control
QP	Quadratic programming
RD	Relative density
RE	Relative error
RF	Random forest
RMSE	Root mean square error
RMV	Resonant meter value
RTK-GPS	Real time kinematics global navigation satellite
SDMT	Seismic dilatometer Marchetti test
SVM	Support vector machine
SVR	Support vector regression
X-SVR	Extended support vector regression

Abstract

Intelligent Compaction (IC) has been acquiring a growing interest in real-time quality control of compacted soil layers because of its high efficiency and full-area coverage. However, accurate real-time determination of the soil modulus during compaction based on roller acceleration impacted by soil characteristics has been challenging due to the multi-layered composite nature of the soil and the nonlinearities of the dynamic equation of motion and soil response.

The main goal of this study is to implement rigorous numerical modelling to simulate the multi-layered granular soil response subjected to cyclic loading, ranging from small to large strain amplitudes and account for stiffness degradation via adopting the finite element method. The benefits of adopting the finite element method are attributed to its capability to simulate interaction problems by achieving more realistic geometries. True scale three-dimensional models with the isotropic hardening elastoplastic hysteretic model were implemented to carefully simulate the boundary conditions and soil behaviour under cyclic loading.

More than 5,000 sets of three-dimensional numerical simulations were run to cover a wide range of frequencies, amplitudes, weights, lift thicknesses and various states of granular soils. The results were adopted in conjunction with the newly proposed extended support vector regression (X-SVR) to establish a robust and accurate method for predicting the real-time unloading-reloading modulus of the compacted soil during compaction.

The findings confirm that the adopted numerical models with the HS-Small constitutive soil model were able to evaluate the nonlinear stress-strain response of the soil subjected to cyclic loading, particularly variations of damping and soil stiffness with shear strain. Moreover, the proposed method could predict both the single and double-layered soil stiffness based on the X-SVR algorithm with the Gegenbauer kernel and Gaussian kernel, using the acceleration response of the drum and basic roller properties. Both training and testing unloading/reloading moduli (E_{ur}), obtained from the machine learning method, correlated well with the 3D finite element predictions considering the nonlinear elastoplastic soil model and dynamic soil-drum interaction.

This research can prove that the inverse solver developed in this study can predict the soil stiffness using the novel kernel-based X-SVR machine learning in a reasonably short time, required for real-time quality control by roller operators on the site. The findings of this study can be employed by practicing engineers to interpret roller drum acceleration data for estimating the level of compaction and ground stiffness during compaction.

Chapter 1

Introduction

1.1. General

The rapid population growth has triggered the increased urban sprawl, directly leading to intensive infrastructure construction activities. As the basic infrastructures, the pavement and road are critical in promoting logistics, resource development, industrial structure adjustment and investment attraction. Therefore, there has been an enormous surge in demand for high-quality road compaction to avoid pavement deterioration because of permeability and potential consolidation. The irregular vehicle behaviour would cause the nonlinear dynamic load to be directly transferred to the underneath soil, rearranging the non-uniform soil particles to the unsatisfied elastic and plastic deformation. Thus, densification through mechanical energy such as vibrated roller compaction minimises the inter-particle air voids and rearranges the underlying soil particles into a dense status. In a simple explanation, the excitation force derived from

compacted roller cyclic loading resulted in plastic or permanent deformation, which is beneficial for road construction.

Efficient, reliable and stable Quality Control (QC) techniques are required to provide high-standard construction quality. The traditional compaction QC approaches are mainly depending on the in-situ spot tests and on-site supervision, which are limited to the discrete testing locations, resulting in less than 1% of the full area being tested and potentially unreliable on-site recordings (Xu et al., 2022b; Nazarian et al., 2020; Wang et al., 2022b). As a comprise, the novel and freshly developed Intelligent Compaction (IC) or Continuous Compaction Control (CCC) can overcome the abovementioned problems, which denotes an innovative practice for pavement construction with a comprehensive and real-time feedback assessment for the compacted process. In addition, the demand for real-time quality control compaction is increasing, particularly for infrastructure projects. Hence, developing an effective and robust model to determine the soil properties during roller compaction using emerging techniques such as Machine Learning (ML) is of great interest to practicing engineers.

The CCC technologies for vibratory rollers, which have been employed in the construction field for over 40 years (Sandström, 1994, Anderegg and Kaufmann, 2004; Xu et al., 2012), are associated with the dynamic analysis of interactions of roller and soil. Indeed, properties of the compacted layer during roller compaction can be detected by analysing the data collected from the accelerometer attached to the drum. Within CCC techniques, roller-integrated monitoring can measure underlying soil properties during compaction by incorporating the Global Positioning System (GPS) and using the response of the vibratory roller changing due to the soil stiffness to be

used for real-time quality control during compaction and avoid early pavement deterioration (Xu et al., 2012; Asif Imran et al., 2018). The Intelligent Compaction (IC) technique is able to exhibit more uniform compaction and a more endurable performance (Xu et al., 2012). Hence, it is of prime importance to allow practicing engineers to thoroughly understand the mechanism of the interaction between the drum and underlying soil (Xu et al., 2022a; Bhandari et al., 2022).

This study primarily concentrated on developing the rigorous finite element modelling for addressing the interactions between the compacted soil and vibratory roller, studying the characteristics of granular soil response under cyclic loading ranging from small to large strain amplitudes and accounts for stiffness degradation. Moreover, thousands of three-dimensional numerical simulations were adopted in conjunction with the newly proposed machine learning technique for achieving real-time unloading-reloading modulus predictions.

1.2. Statement of Problem

Despite the roller compaction techniques developed in the past in assessing the compaction level of underlying materials, the heterogeneity of compacted material and non-uniform degree of compaction remains the main sources of infrastructure and design uncertainties due to the lack of real-time assessment of compacted soil properties.

To simulate the stability of the underlying geomaterial and its load-bearing capacity, field tests are commonly used for conventional compaction QC (Wang et al., 2022b). In particular, in-situ methods, such as Falling Weight Deflectometer (FWD) (Alshibli et al., 2005; Asli et al., 2012), Dynamic Cone Penetrometer (DCP) (Siekmeier et al.,

2000) and Light Weight Deflectometer (LWD) (Fleming et al., 2007; Ryden and Mooney, 2009) are used to estimate the stiffness of geomaterials, but some manual quality control methods are destructive, low efficiency and time-consuming (Zhu et al., 2018; Zhang et al., 2019). These QC approaches cannot provide real-time monitoring during compaction, minimising their efficiency in terms of providing the opportunity to adjust the number of passes and roller settings required in an efficient fashion.

Furthermore, Non-Destructive Testing (NDT) as well as invasive testing, such as sand cone devices, are also generally used to certify the satisfactory subgrade quality at discrete spots. However, these specific in-situ methods are limited to the discrete testing locations, which cannot precisely assess the full-area compaction level, resulting in less than 1% of the full area being tested, and potentially remaining regions may be ‘over-compacted’ or ‘under-compacted’ (Wang et al., 2022b; Nazarian et al., 2020). As a consequence, it can negatively impact long-term performance. Gomes Correia et al. (2013) illustrated that conventional compaction might exacerbate the performance of the roadway's compaction, especially in the serviceability phase – an essential phase of infrastructure works. Other drawbacks include possible damage to the compact due to the manual measurement; and the cost-consuming nature of in situ tests.

Moreover, according to Mooney and Facas (2013), the relationship between Measurement Values (MVs) and soil response is complicated; However, numerous measurements have been proposed to estimate the status of soil properties associated with the IC technology. One shortcoming is that a standard-size vibratory roller (12 – 15 tons) provides the simulated soil stiffness, of which the measurement is composite

with the 1.0 – 1.2 m depth of total layer properties. A considerable result of layer properties is that the measured thickness of soil varies from 150 – 300 mm via an in-situ correlation. However, many previous studies can only investigate the one-layered stiffness or the composite natural stiffness on the two-layered pavement because of the coupled lumped parameter vibration model. Thus, the measured stiffness can be impacted by the underlying layers or previous lifts because the impact depth of the vibratory roller exceeds the thickness of the measured layer. The independent stiffness of the subgrade, subbase, and base is advantageous for improving compacting and identifying the weak layer more efficiently. Therefore, developing an efficient and precise extracting soil methodology based on the dynamic soil-drum responses is necessary.

1.3. Objectives

The primary goal of the research is to establish a rigorous and efficient method that can rapidly and accurately extract the compacted soil stiffness according to the vibratory response of the drum. The established method can be used as potential guidance by practicing engineers and construction teams to achieve high-quality compaction.

To better understand the responses of the geomaterial underneath the roller, representative dynamic 3D finite element models are developed to evaluate the sophisticated interaction between the layered soil and the vibratory drum. The detailed objectives are shown as follows:

- Identifying the gap through literature review and research addressed previously to develop a proper, novel, and specific methodology to achieve the real-time extraction of soil stiffness.
- Finding a proper constitutive model to establish the nonlinear sophisticated contact problem to prove the effectiveness, capability and feasibility of the adopted numerical methods in studying soil and drum interactions.
- Investigating the nonlinear behaviour of soil underneath the vibratory roller subjected to dynamic loading, particularly variations of damping and soil stiffness with the cyclic shear strain to evaluate the effects of the characteristics of roller parameters.
- Simulating the single-layered soil stiffness of the compacted soil by adopting an innovative machine learning approach, incorporating the drum acceleration records.
- Investigating a real-time back-calculation method with the 3D Finite Element Model (FEM), accounting for soil-drum interaction to address the soil stiffness extraction from the double-layered soil profile.

1.4. Scope and Limitations of the Work

This study investigates the advanced 3D FEM, combined with the newly proposed machine learning technique, to predict underlying modulus during compaction. The isotropic hardening elastoplastic hysteretic model is implemented to carefully establish boundary conditions and capture compacted geomaterial behaviour subjected to cyclic loading. The soil deposit for all models is considered above the water table. The study employs the FEM and machine learning approach to back-calculate

compacted sandy soil stiffness, and the relative density of compacted soil varies between 20% and 90%.

1.5. Organisation of the Thesis

The thesis is organised into seven chapters, with the introduction, problem statement, research objectives, scope, and work limitations, presented in this chapter. The brief introduction of the resting six chapters is presented as follows:

Chapter 2 describes a systematic and concise review of the literature on past techniques adopted in extracting the underlying soil properties, assessing the existing research studies implemented on the various Intelligent Compaction Measurement Values (ICMVs), numerical methods, and different constitutive models.

Chapter 3 assesses the function of recently proposed machine learning methods, which incorporates the data acquired from the finite element method, adopted for capturing the interactions between a vibratory roller and underlying materials. Two different regression approaches are presented: linear Extended Support Vector Regression (X-SVR) and kernel-based nonlinear X-SVR.

Chapter 4 assesses the effectiveness of the Hardening Soil model with Small Strain Stiffness (HS-Small) constitutive model adopted in a 3D FEM to evaluate the impacts of selection of vibration frequency, amplitude and roller weight in sandy soil. The obtained numerical predictions are compared with previously analytical data and recommendations to practicing engineers on choosing the best roller parameters during the compaction process.

Chapter 5 presents details of a robust FEM in conjunction with the advanced kernel-based Machine Learning (ML) method for extracting the compacted soil modulus during compaction in the single-layer sandy soil deposit. The outcomes exhibit that the proposed approach can accurately predict the soil stiffness based on the X-SVR algorithm with the Generalised Gegenbauer kernel (GGK) in the reasonably short time required for real-time quality control by practicing engineers.

Chapter 6 evaluates the real-time extraction of double-layered soil stiffness during the compaction by X-SVR in conjunction with Gaussian kernel and GGK functions. Furthermore, a further study was employed to research the influences of the double-layer soil modulus ratio of the soil settlement as well as the impacts of the roller length and the increase in the upper layer modulus on cumulative surface displacement. The results in this chapter show that the proposed approach can capture the double-layer soil moduli, offering recommendations for further study on soil moduli of multi-layered soil profiles.

Chapter 7 summaries the acquired observations of this study and comprises some recommendations for future research.

Chapter 2

Literature Review

2.1. Introduction

Pavement performance is significantly affected by the layered soil permeability and strength, as well as the moduli of the subgrade layers. Along with the substantial expansion in the number of vehicles, the stability of the pavement should be ensured in the construction process to avoid road surface collapse, overcoming the tremendous amount of irregular dynamic behaviour of vehicles. Sandström (1994) stated that vibratory roller compaction could be the most prevalent methodology to improve pavement strength. An ideal compaction process can permanently reduce permeability and undesirable settlement, while improving the strength of the compacted layers. According to Asif Imran et al. (2018), proper vibratory compaction on the foundation is required to provide sufficient strength to withstand the traffic load and support the top layers of the pavement. An adequate and entirely compaction on the base, subbase

and subgrade layers can increase the performance of the pavement, improve the ability to decrease the distress and withstand the load.

A desirable compaction process can increase compacted layer strength and decrease undesirable settlement and permeability. However, Zhu et al. (2018) demonstrated that the conventional compaction roller measurement is not fully reliable for the following reasons:

- The operator might control the roller under-compacted or over-compacted the soil because they lack real-time compaction information during the conventional compaction work.
- The limited number of in-situ test spots cannot cover the full area of the construction site. It is incapable of figuring out the full area compacted soil status.
- The manual measurements are destructive to the compaction, and many in situ tests are time and cost-consuming.

In-situ spot tests, a significant stage in conventional compaction, are required to verify the layered soil compaction status after soil compaction. Kumar et al. (2016) indicated that strict conditions should be considered when applying the in-situ spot tests. One example is that less than 1% of the compacted geomaterial properties could be assessed by applying in-situ tests for quality control and quality assurance (Gallivan et al., 2011). It means the results might be unconvincing; thus, its performance can worsen in the long-term. Gomes Correia et al. (2013) demonstrated that conventional compaction would possibly exacerbate the compaction of roadway performance,

especially during the serviceability phase, and the problem was addressed by the use of the IC technique.

In general, on the basis of the conventional vibratory roller technologies, the IC is developed (Anderegg and Kaufmann, 2004), attaching the advanced measurement system to continuously capture equipment performance. As part of the measurement system, the accelerometer is attached to the roller drum, which can detect and analyse the properties of the compacted layer during roller compaction. Additionally, roller-integrated monitoring in conjunction with GPS can reflect the real-time feedback of compacted soil on the accurate position after analysing the captured soil signal; thus, the operator can adjust the roller to avoid early pavement deterioration to optimise compaction quality and improve the efficiency of the ground compaction. Figure 2.1 demonstrates the overview of the intelligent compaction structure.

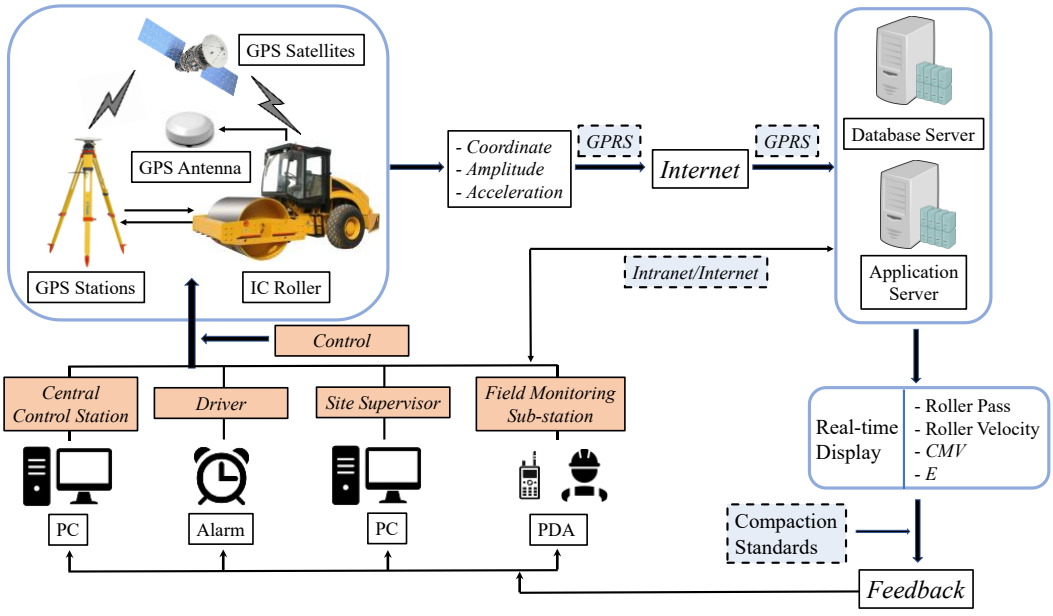

Figure 0.1 Framework of the CMV real-time monitoring (modified after Liu, Lin & Li, 2016)

The working procedure of employing intelligent compaction on the infrastructure site can be explained as the IC roller operates under an auto-feedback system. The experienced roller operator can adjust the roller according to the feedback control and underneath soil properties information from the system during the compaction. The eccentric masses attached inside the drum rotate at a constant frequency around the axis and are shafted concentrically to the roller drum axis; then, the cyclic translational vibration will be led by period eccentric mass rotation. In addition, according to Newton's second law theory, when the excitation force is vertically acted on the soil, there will be an equivalent value of the reacted force response from the soil. After applying the pre-determined dynamic load value to the roller, the accelerometer will record the contacted force, acceleration and frequency, and the captured data can be analysed to exhibit the soil properties. Each type of roller has different ICMVs; for example, Ammann soil stiffness k_s is back-calculated the soil properties by establishing a relationship between reacted force and drum displacement and then extracting the soil modulus by analysing the gradient of the curve. The details of different ICMVs are represented in the following part.

2.2. History of Intelligent Compaction

The development of roller compaction integrated the measurement values with the roller operation to achieve "intelligent" compaction, namely Intelligent Compaction (IC). The initiated IC techniques can be historically traced to the 1970s for soil compaction in Europe and an increasing interest in employing IC rollers on the construction site until now (Chang and Gallivan, 2011; Mooney, 2010). In 1974, Dr Herinz Thurner initially conceptualised the roller-integrated measurement by applying the 5-tonne roller instrumented with the accelerometer to identify the compacted soil

status by utilising drum harmonics signals as the indicator (Thurner and Sandstrom, 2000). Furthermore, the analysed results could be correlated to the soil stiffness and level of compaction. Then, a dimensionless parameter measurement value was developed, namely Compaction Meter Value (CMV), by Dr Herinz Thurner and his partner Åke Sandström in 1978 (Thurner, 1980; Forssblad, 1980), followed by Dynapac company firstly providing the CMV-based Compactometer in 1980.

With the commercially available CMV-based instrument, several other roller manufacturers established different roller-integrated vibration compactor systems. In the early 1980s, Bomag company introduced an indicator – Omega value to continuously reflect the underlying soil energy during roller compaction, which was replaced later by a measurement technology value vibratory modulus (E_{vib}), which can capture the dynamic soil stiffness (Krober et al., 2001). Ammann explained the mechanical soil stiffness modulus k_s (Anderegg and Kaufmann, 2004), which is similar to E_{vib}, and it utilised the spring dashpot system to extract the soil modulus via the slope of quasi-static estimated excitation force and drum movement during compaction. Furthermore, Sakai introduced a dimensionless parameter measurement values based on the CMV, namely Compaction Control Value (CCV*)* (Scherocman et al., 2007), which employs the sub-harmonic and fundamental frequencies to estimate the compaction degree. Additionally, an alternative measurement value was developed by Caterpillar, namely Machine Drive Power (MDP), in the early 2000s, which is a mathematically determined value of internal power consumption to predive the level of compaction rather than utilising vibratory compaction.

2.3. Intelligent Compaction Measurement Values (ICMVs)

Several ICMVs are obtained during the roller compaction to reflect the quality of the underlying compacted soil.

Table 0.1 Summary of roller measurement values (modified after Chang & Gallivan, 2011 and Tehrani, 2009)

Machine value	Name	Manufacturer	Description
CMV (unitless)	Compaction Meter Value	Geodynamik, Dynapac, Volvo, Hamm	Based on roller operation parameters (e.g., speeds, frequencies, and amplitudes), as well as the roller dimensions (e.g., the diameter of drum and weight of roller).
CCV (unitless)	Compaction Control Value	Sakai	In the frequency domain, the vertical drum vibration is the algebraic relationship of multiple amplitudes.
E_{vib} (MPa)	Vibratory modulus	Bomag	In the time domain, the dynamic elasticity stiffness of underlying layered soil. The modulus is able to be derived from the inclination of contacted force – vertical drum displacement curve regarding the soil-drum interaction system.
k_s (MN/m)	Stiffness	Ammann	The spring stiffness of the underlying compacted soil beneath the drum is in the time domain. The stiffness can be derived from the maximum drum deflection of contacted force – vertical drum displacement curve regarding the soil-drum interaction system.
MDP (kW)	Machine Drive Power	Caterpillar	Empirical relationship between mechanical behaviours of a drum to the compacted underlying geomaterial.

The mechanistic measurements, number of roller passes, vibratory roller position, and speed derived from intelligent compaction roller allow engineers to study the compaction uniformity; hence, a thorough understanding of qualitative control of the soil-drum system is of prime importance. The various common roller-integrated Measurement Values (MVs) incorporated with different equipment manufacturers have been summarised in Table 2.1.

2.3.1. Compaction Meter Value (CMV)

2.3.1.1. CMV Measurement

The main purpose of the above-mentioned ICMVs with different vendors is to evaluate the level of compaction or extract the underlying compacted geomaterial properties during roller compaction. Since the vibratory drum periodically blew the underlying geomaterial, similar to the dynamic plate load test (Tehrani, 2009; Hu, 2018). Therefore, a reasonable simulation is proposed that utilises the blows from the cylindrical vibratory drum as a load test of the underlying geomaterial. Several researchers or companies approved a strong relationship to represent the level of compaction by evaluating the different harmonic amplitude, such as Sandström (1994); Thurner and Sandstrom (2000); Adam (1997). The deformation modulus E_{cd} then can be demonstrated as Equation 2.1.

$$E_{cd} = c_1 \times \frac{F}{d} = c_2 \times \omega^2 \times \frac{A_{2\Omega}}{A_{\Omega}} \quad (2.1)$$

where F is the force of the blows; d represents the surface soil settlement; ω is the fundamental angular frequency; c_1 and c_2 are constants; $A_{2\Omega}$ and A_{Ω} are the acceleration of the vibration's first and fundamental harmonic components.

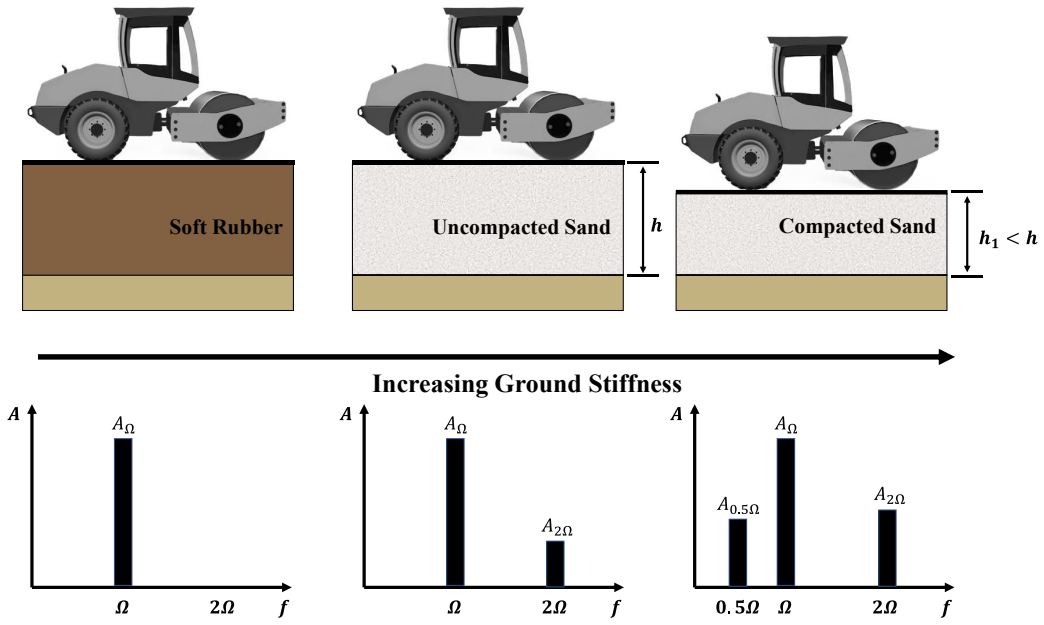

Figure 0.2 Explanation of increasing soil stiffness results in changing in amplitude spectrum (modified after White and Vennapusa, 2010)

According to the general framework of the concept mentioned above, a dimensionless indicator CMV was established by Geodynamik, which can be denoted as the frequency analysis, and it is capable of assessing the level of the compaction by recording variable acceleration with different dynamic drum responses. It should be noted that the increasing layer stiffness results in changing roller harmonics, and it can be explicitly observed that the CMV is increasing with the status of soil from loose to dense, as shown in Figure 2.2. The ratio between the $A_{2\Omega}$ and A_{Ω} could be applied to evaluate the level of the CMV, which is shown in the following equation.

$$CMV = C \times \frac{A_{2\Omega}}{A_{\Omega}} \tag{2.2}$$

where C is a constant value commonly selected as 300. It should be observed that the relationship between A_{Ω} and $A_{2\Omega}$ is the measure of nonlinearity or degree of distortion. In addition, the detailed spectral analysis is shown in Figure 2.3 to determine the CMV values of the drum over two cycles of vibration. The modelled equation is empirical

and potentially impacted by the frequency, forward velocity, amplitude, characteristics of the drum and various types of soil (Floss et al., 1991). Thus, the calibrations are required after the compaction.

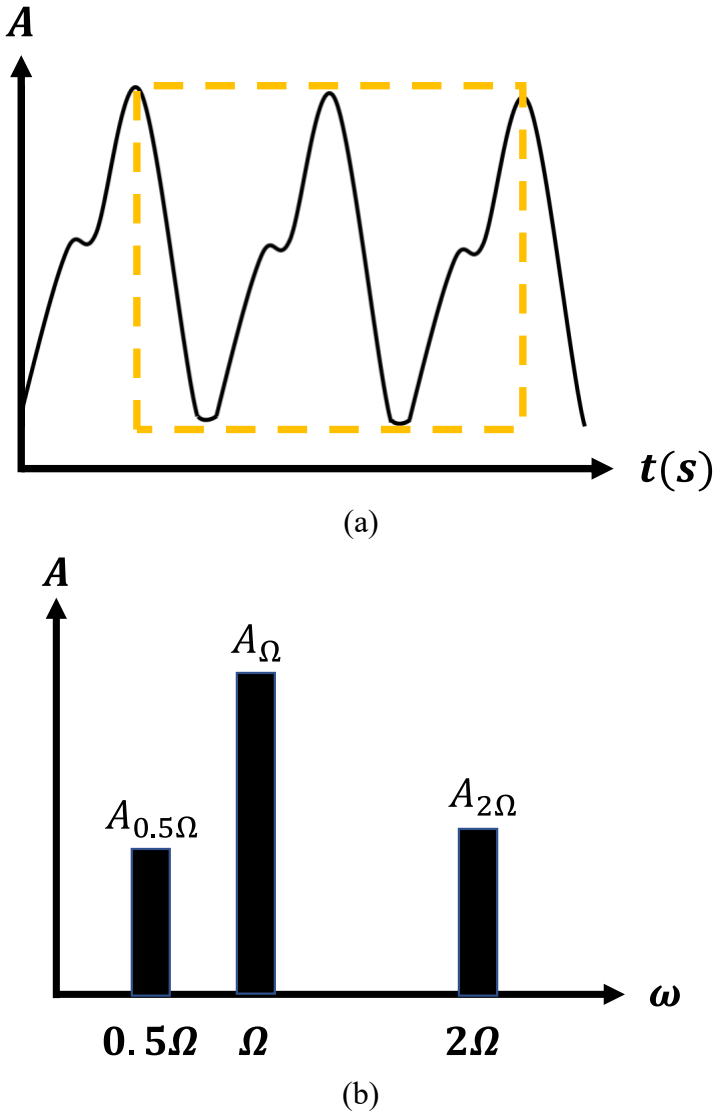

Figure 0.3 (a) Fast Fourier Transform (FFT) analyses to determine CMV of (b) two cycles of vertical acceleration of drum time history data (modified after Mooney and Adam, 2007)

2.3.1.2. Resonant Meter Value (RMV)

Furthermore, Geodynamik developed the RMV, commonly applied as an indicator in Compactometer systems to avoid unstable drum behaviour, where a signal from loss

of contact interaction between soil and drum will cause a sub-harmonic acceleration amplitude $A_{0.5\Omega}$. It is proportional to the quotient of $A_{0.5\Omega}$ divided by A_{Ω} as shown in Equation (2.3), where a non-zero value means the drum is not continuously compact the soil (Adam, 1997):

$$RMV = \frac{A_{0.5\Omega}}{A_{\Omega}} \tag{2.3}$$

Adam and Kopf (2004) conducted several numerical and experimental investigations on interaction behaviour between drum-soil systems. Then five different operation modes of the roller were introduced, mainly depending on its operational settings (speed, frequency and amplitude) and the nonlinearity of soil behaviour under vibration. Drum behaviour is the primary factor in defining the different modes of compaction. When the roller-drum system kept continuous compaction during compaction, the value of RMV equals 0. When the value of RMV is larger than 0, the drum suffers unstable motions.

2.3.1.3. The procedure of conducting the real-time CMV determination

The framework of the CMV real-time monitoring is demonstrated in Figure 2.1. The complete structure consists of the roller-integrated vibration compactor, the Real Time Kinematics Global Navigation Satellite (RTK-GPS) locating system, the remote monitoring centre, the application and database server, the wireless control centre, and the Personal Digital Assistant (PDA). According to Liu et al. (2016), the procedure of applying a real-time CMV roller can be briefly explained as follows:

(1) Real-Time Kinematics can be applied to capture the accurate position in 10-30 mm horizontally and 20-50 mm vertically, which achieves in conjunction with GPS to provide real-time vibratory roller coordinates. Then the collected data will be packed and transferred to the application and database services.

(2) The compacted layer is divided into numbered grids. Equations (2.4) to (2.7) are applied to reflect the speed of the compaction roller v_{CMV}^{t} at the time t_{CMV}, passes of cyclic rolling $n_{CMV}^{k,t}$ in grid k_{CMV} at time t_{CMV}, and thickness of compacted geomaterial H_{CMV}^{k} in grid k_{CMV}.

$$v_{CMV}^{t} = \frac{|P_t - P_{t-1}|}{T_t - T_{t-1}} = \frac{|P_t - P_{t-1}|}{\Delta t} \tag{2.4}$$

where $|P_t - P_{t-1}|$ denotes the Euclidean distance between P_t and P_{t-1}, and Δt denotes the time interval between samplings.

$$n_{CMV}^{k,t} = \begin{cases} n_{CMV}^{k,n-1} + 1, (x_{CMV}^{t}, y_{CMV}^{t}) \in \Omega_{CMV}^{k}, \\ n_{CMV}^{k,t-1}, \quad (x_{CMV}^{t}, y_{CMV}^{t}) \notin \Omega_{CMV}^{k}, \end{cases} n_{CMV}^{k,0} = 0 \tag{2.5}$$

where $(x_{CMV}^{t}, y_{CMV}^{t}) \in \Omega_{CMV}^{k}$ indicates in the $t-th$ time interval, and $(x_{CMV}^{t}, y_{CMV}^{t})$ is the $k-th$ grid Ω_{CMV}^{k}. Moreover, the compacted thickness in the CMV technique $h_{CMV}^{k,t}$ in grid k_{CMV} at time t_{CMV} is calculated by applying the following equation:

$$h_{CMV}^{k,t} = z_{CMV}^{t} - Z_{CMV}^{k,0} \tag{2.6}$$

Thus, the thickness of the compacted underlying geomaterial in the $k-th$ grid can be explained by Equation (2.7):

$$H_{CMV}^{k} = \max_{t}\{h_{CMV}^{k,t}\} = Z_{CMV}^{k,1} - Z_{CMV}^{k,0} \tag{2.7}$$

where z_{CMV}^{t} is the elevation at time t_{CMV}, $Z_{CMV}^{k,0}$ indicates the initial elevation of grid k_{CMV} and it follows the road design. However, the $Z_{CMV}^{k,0}$ is not a constant value, where different coordinates of compaction points may have various initial elevations. $Z_{CMV}^{k,1}$ indicates the elevation after compaction of the grid k_{CMV}, which can be expressed as Equation (2.8)

$$Z_{CMV}^{k,1} = \underset{t}{max}\left\{Z_{CMV}^{t} \middle| (x_{CMV}^{t}, y_{CMV}^{t}) \in \Omega_{CMV}^{k}\right\} \tag{2.8}$$

(3) The accelerometer is attached to the vibrated drum to capture and record the vertical acceleration responses from the interaction between soil and drum during compaction. The recorded signal will be converted from the time domain to the frequency domain through FFT. Equation (2.2) is then employed to compute the CMV values in the application and database server.

(4) The excitation force of the vibrating roller can be extracted through the equation $F_{CMV}^{e} = m_0 e_0 \omega^2$, $m_0 e_0$ is the eccentric mass moment and ω represents angular frequency. According to step (2), the value of v_{CMV}^{t}, $n_{CMV}^{k,t}$, and H_{CMV}^{k} can be computed, respectively, and then the compaction information can be monitored.

(5) The remoted control centre can analyse the compaction parameters in the real-time (e.g., compacted thickness, compaction elevation, rolling passes and roller trajectory). Once there are any deviations from the provided standards, the operator can adjust the machine based on the warning information.

(6) The compacted soil thickness, rolling passes, roller speed and trajectory will be stored in the database, which can be utilised later for overall compaction quality control.

2.3.2. Compaction Control Value (CCV)

A dimensionless determination of Sakai CCV takes the acceleration data into account to figure out the compaction level, expanding from the CMV index. The analog bandpass filtering can be used to capture the excitation frequencies of acceleration from the first acceleration data, fundamental, to higher-order harmonics, as shown in Equation (2.9).

$$CCV = \left[\frac{A_{3\Omega} + A_{2.5\Omega} + A_{2\Omega} + A_{1.5\Omega} + A_{0.5\Omega}}{A_{\Omega} + A_{0.5\Omega}}\right] \times 100 \tag{2.9}$$

In addition, Figure 2.4 demonstrates the relationship between the increased ground stiffness and the results in changing in the amplitude spectrum.

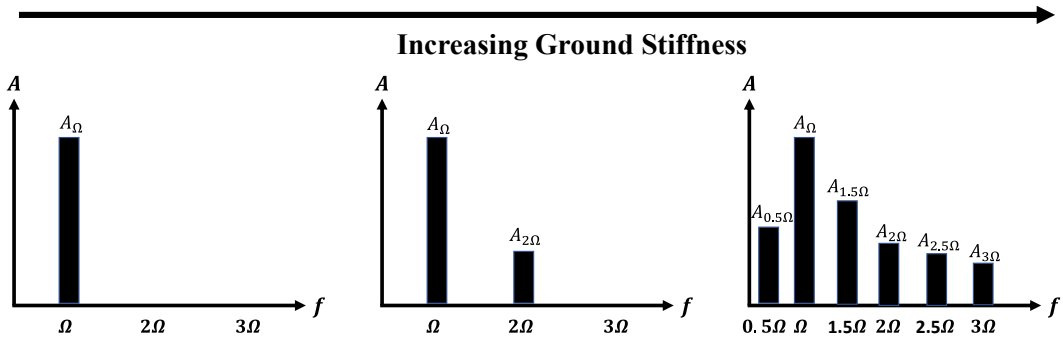

Figure 0.4 Explanation of increasing soil stiffness results in changing in amplitude spectrum (modified after Scherocman et al., 2007)

2.3.3. Roller-Integrated Stiffness (k_s)

The factor of the roller-integrated stiffness system k_s could be used to capture the soil stiffness during each cycle of roller vibration, which was introduced by Ammann according to the lumped parameter system (Anderegg and Kaufmann, 2004). Figure 2.5 describes using a free-body diagram with a spring dashpot model to study the soil and roller behaviour during compaction, while the spring dashpot model can capture the soil responses during roller compaction effectively, which was approved by Yoo and Selig (1980). The independent roller frame mass was represented as m_f, which was supported by the elastic suspension element with damping c_f and stiffness k_f. The compacted soil underneath the vibratory roller is simulated as a spring with the viscous damper c_s and stiffness k_s.

The eccentric drum force (F_{ecc}) and inertia force time histories are computed through drum eccentric position and acceleration responses reflected by the interaction between the soil-drum system. It should be noted that the increased value of stiffness resulted in the decreased damping value during compaction and when considering the constant machine parameters. The dynamic behaviour of the drum and underlying compacted geomaterial could be explained by applying the following equations (Anderegg and Kaufmann, 2004)

$$F_c = -m_d\ddot{z}_d + m_e e_e (2\pi f)^2 \cos(2\pi f t) + c_f(\dot{z}_d - \dot{z}_f) + k_f(z_d - z_f) + m_d g \quad (2.10)$$

$$0 = -m_f\ddot{z}_f + m_f g + c_f(\dot{z}_f - \dot{z}_d) + k_f(z_f - z_d) \quad (2.11)$$

where the interaction force between soil and drum F_c can be represented as:

$$F_c = \dot{z}_d c_s + z_d k_s \quad \text{if } F_c \geq 0 \tag{2.12}$$

$$F_c = 0 \quad \text{else} \tag{2.13}$$

where $m_e e_e$, f and t are the eccentric mass moment, vibration roller frequency, and dynamic time, respectively, F_c is the contact force; z, $\dot{z}$ and $\ddot{z}$ denote the displacement, velocity and acceleration of the vibratory roller frame or drum, respectively;

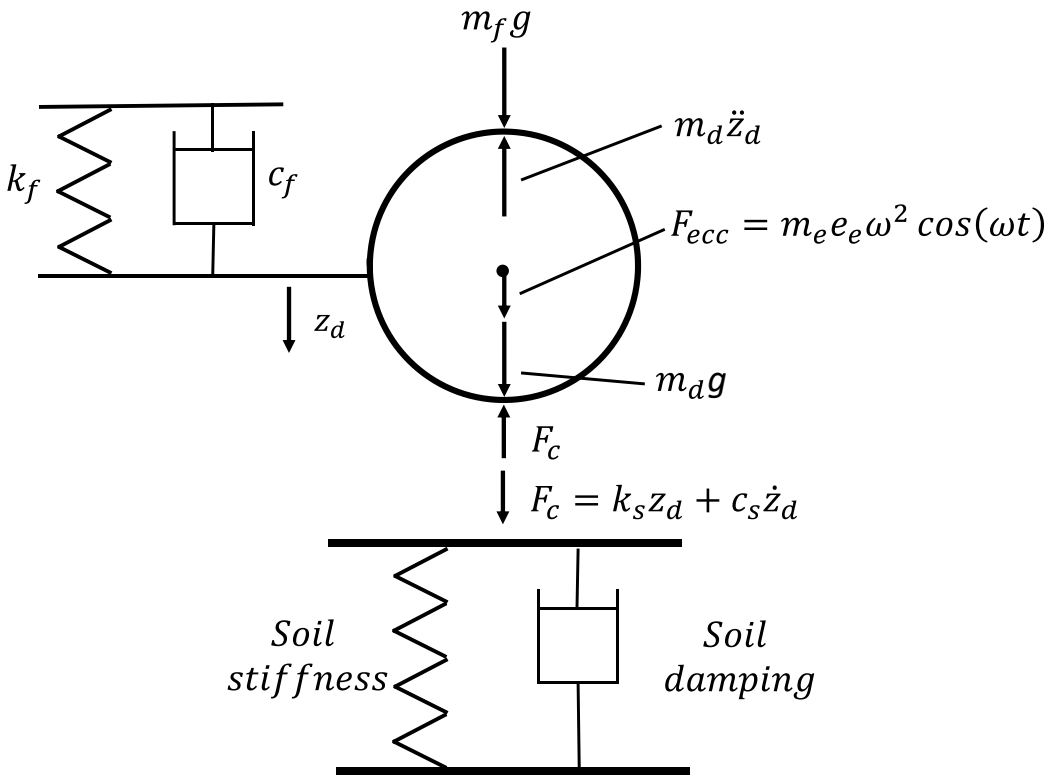

Figure 0.5 The free-body diagram of the simplified vibratory roller compactor

However, the drum is independent from the compactor frame by the equipped low-stiffness rubber, leading to insignificant influences of the dynamic frame, and thus neglected in the analysis (Kenneally et al., 2015; Herrera et al., 2018; Xu et al., 2022a). Thus, when neglecting the dynamic behaviour of the roller frame, the contact force can be obtained as the following equation:

$$F_c = -m_d\ddot{z}_d + m_e e_e (2\pi f)^2 \cos(2\pi f t) + (m_f + m_d)g \qquad (2.14)$$

The correlation between the contact force F_c and drum displacement z_d is valid to capture the soil behaviour accordingly and could be utilised as the indicator to identify the modulus of the compacted underlying soil in the continuous compaction control system (Anderegg and Kaufmann, 2004). Therefore, the relationship between F_c and z_d can be graphically utilised to indicate the soil stiffness of continuous contact and partial uplift, respectively (Figures 2.6 and 2.7).

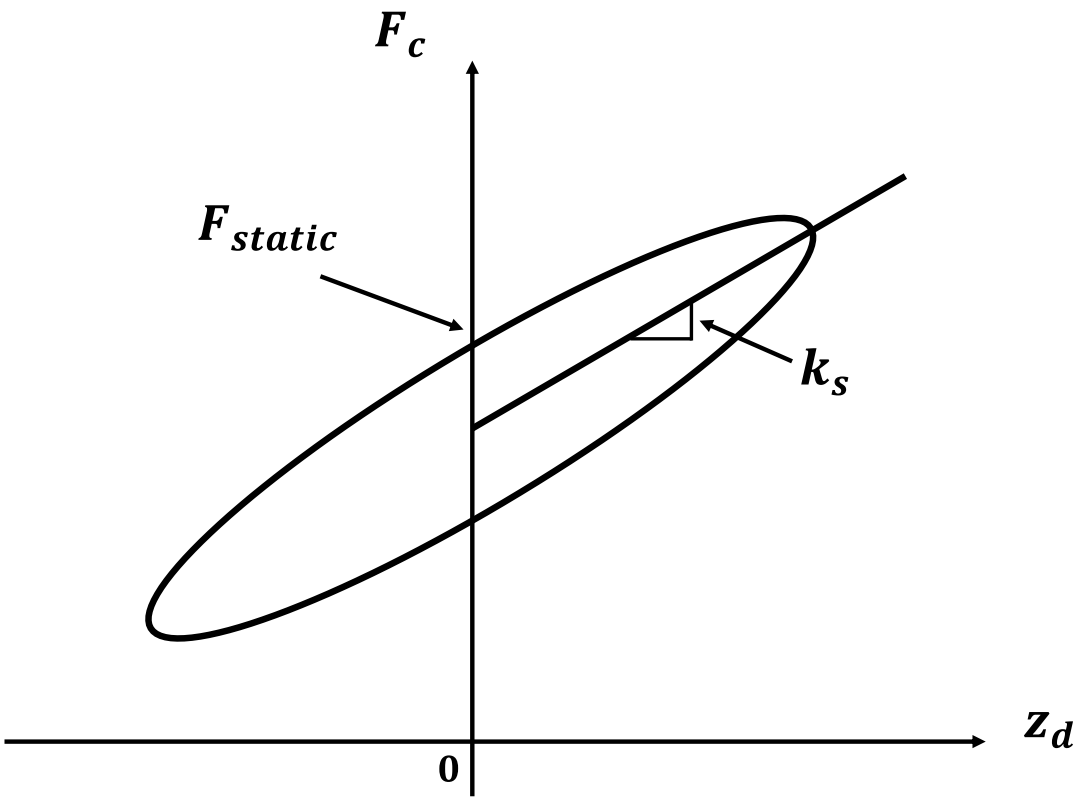

Figure 0.6 The correlation between F_c and z_d representing the soil stiffness k_s during continuous contact behaviour (modified after Mooney and Adam, 2007)

The roller-integrated stiffness k_s introduced by Ammann is the ratio between the contact force F_c and drum displacement z_d. The roller-integrated stiffness measures the composite static stiffness of the compacted geomaterials.

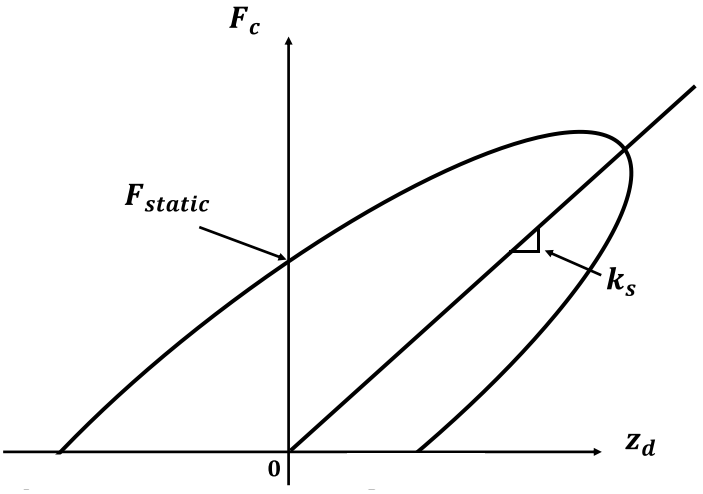

Figure 0.7 The correlation between F_c and z_d representing the soil stiffness k_s during partial uplift behaviour (modified after Mooney and Adam, 2007)

Furthermore, when considering the linear elastic soil model with the nonlinearity of the vibrated drum, the measurement value of amplitude and phase angle can calculate the corresponding value of k_s (Anderegg and Kaufmann, 2004)

$$k_s = \frac{F_c|_{\dot{z}_d=0} - (m_f + m_d)g}{A} \tag{2.15}$$

where A is the measured vibration amplitude, additionally, continuous contact between soil and drum, the roller-integrated stiffness can be computed applying the Equation (2.16):

$$k_s = (2\pi f)^2 \left[m_d + \frac{m_e e_e \, cos(\varphi)}{A} \right] \tag{2.16}$$

where, φ denotes the measured phase angle. Then subject to the condition of: $F_c|_{max} \leq 2 \times (m_f + m_d)g$:

$$F_c|_{max} = (m_f + m_d) \cdot g \cdot \pi \frac{1 + cos\left(\frac{t_{l.o.c}}{T} \cdot \pi\right)}{\left(1 - \frac{t_{l.o.c}}{T}\right) \cdot \pi \cdot cos\left(\frac{t_{l.o.c}}{T} \cdot \pi\right) + sin\left(\frac{t_{l.o.c}}{T} \cdot \pi\right)} \tag{2.17}$$

where, $F_c|_{max}$ represents the peak interaction force between underlying soil and vibratory drum during one period T, the $t_{l.o.c}$ represents the loss of contact time (Anderegg and Kaufmann, 2004).

2.3.4. Vibratory Modulus (E_{vib})

Vibratory modulus E_{vib} was proposed by IC roller manufacturer Bomag (German), which employed Lundeberg's theoretical solution (Lundberg, 1939) and lumped parameter model regarding a rigid cylinder resting on the elastic half-space earth to determine the level of the compaction from the force-displacement hysteresis loops (Krober et al., 2001).

The two accelerometers were attached to the drum with an $\pm 45°$ from vertical to record the drum's acceleration. Then the applied force F_c can be determined according to Equation (2.14) and the vibratory modulus enabling to be determined from the combination of F_c and z_d. The introduction of vibratory modulus and stiffness value exhibited a significant innovation in measuring more performance-related, mechanistic soil stiffness/modulus.

The vibratory modulus has similar definitions and assumptions for computing soil modulus with the stiffness value. When computing the soil properties, E_{vib} employed the slope to the hysteresis loops at 20% and 80% of the changes between the minimum and maximum contact forces to define the modulus. While k_s is the secant stiffness which is the gradient line connected by the point of the peak vibratory drum displacement and the point of the zero vibratory drum displacement.

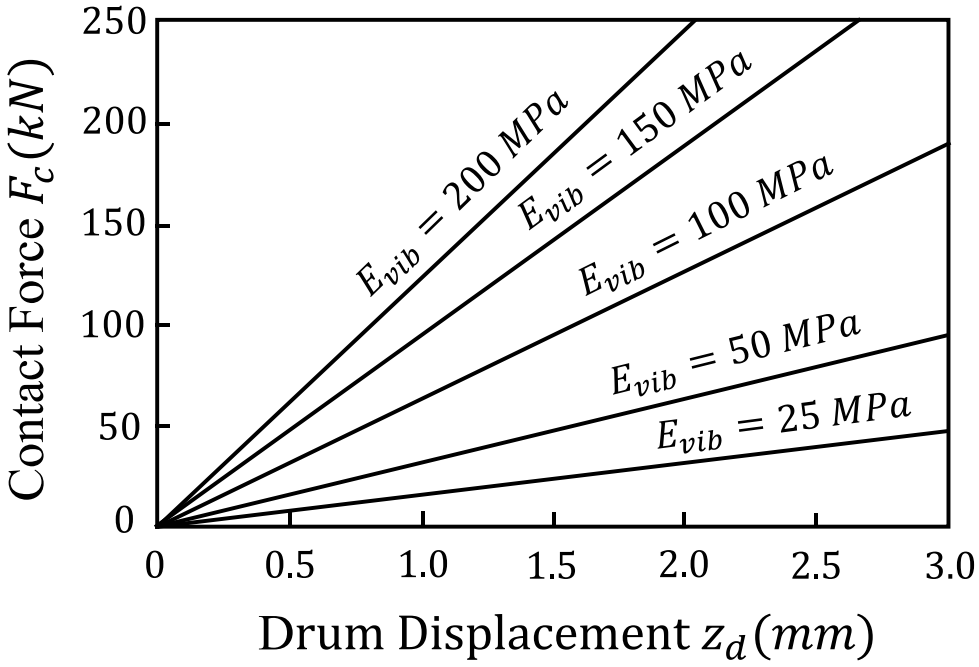

Figure 0.8 The correlation between F_c and z_d (modified after Mooney and Adam, 2007)

To correlate the contact force F_c versus drum displacement z_d during roller compaction and extract the soil modulus E_{vib}, Lundberg's solutions (Lundberg, 1939) were applied, as shown in Figure 2.8. The concept is based on the number of closed-form solutions related to the estimations of indentation depth of the rigid object lying on the homogeneous, isotropic, elastic half-space earth. Equations (2.18) and (2.19) have to be solved simultaneously to obtain the E_{vib}.

$$z_d = \frac{1-\vartheta^2}{E_{vib}} \cdot \frac{F_c}{L} \cdot \frac{2}{\pi}(1.8864 + ln\frac{L}{B}) \tag{2.18}$$

$$B = \sqrt{\frac{16}{\pi} \cdot \frac{R(1-\vartheta^2)}{E_{vib}} \cdot \frac{F_c}{L}} \tag{2.19}$$

where the contact width is represented as B, drum length is represented as L, material Poisson's ratio is represented as ϑ, and R is the drum's radius.

2.3.5. Machine Drive Power (MDP)

MDP can be defined as a compaction technology that associates the compacted geomaterial underneath the drum with the mechanical performance of the vibratory roller. Based on the semi-empirical method, Caterpillar developed the proposed technology to measure the necessary compaction energy to overcome the resistance to motion.

The MDP system was designed based on the theory that the requirement of roller moving energy is significantly impacted by the drum's sinkage into the compacted soil, which can effectively be operated on fine-grained and cohesive soils. Bekker (1969) illustrated that Schuring established workable formulas to indicate the motion resistance with the energy loss in soil.

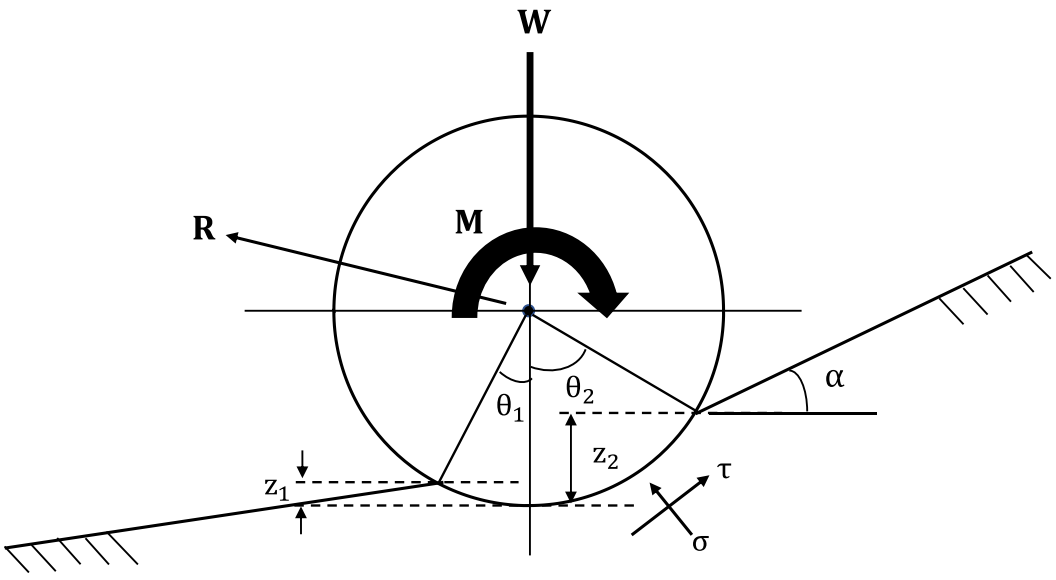

Figure 0.9 Detailed 2D sketch of the vibratory drum for MDP (modified after White et al., 2005)

Therefore, to identify the relationship between the energy loss E_{loss} in compacted soil and torque M applied to the drum (Figure 2.9), which can be given as:

$$E_{loss} = \frac{l}{1-i}\left(iR - R + \frac{M}{r}\right) \tag{2.20}$$

where r denotes the radius of the vibratory drum, i denotes the wheel slippage, R denotes the drawbar pulling force, and l denotes the horizontal distance rolling by roller. Furthermore, the abovementioned equation can also be rewritten according to the resultant vertical stress σ_v and horizontal stress σ_h applying on the drum (Bekker, 1969), which is shown as:

$$E_{loss} = \frac{l}{1-i} br \left(\int_{\theta_1}^{\theta_2} \sigma_v \theta d\theta + i \int_{\theta_1}^{\theta_2} \sigma_h \theta d\theta \right) \tag{2.21}$$

where θ represents the interface contact angle, and it has a positive relationship with the sinkage depth z (Equation (2.22)). The sinkage depth changes with the compressibility of the compacted soil and shear strength shown in Equation (2.23), which also can be observed z is dependent on the weight W, the width b and the diameter D of the vibratory drum, the friction modulus and cohesion of soil settlement k_c and k_φ, as well as the exponent of soil sinkage n.

$$\theta_i = cos^{-1}\left(\frac{r - z_i}{r}\right) \tag{2.22}$$

$$z_i = \left[\frac{3W}{\sqrt{D}(-n+3)\left(bk_\varphi + k_c\right)}\right]^{\frac{1}{2n+1}} \tag{2.23}$$

The determination of the empirical parameters such as n, k_φ, and k_c are complex to capture without PLT (Bekker, 1956). In addition, k_φ, and k_c are mainly depending on the soil shear strength, but sinkage is highly sensitive to changes in soil density (Bell, 1977), which directly resulted in soil compaction.

The semi-empiricism approach was provided to predict the energy soil loss as shown below:

$$P_g = P_{sa} + P_s + P_{ml} \tag{2.24}$$

where P_g illustrates the minimum required total energy to facilitate the roller movement, P_{sa}, P_s, and P_{ml} is the additional machine power, the part of the power applied to overcome resistance and the internal machine power loss, respectively. Furthermore, Equation (2.24) can be altered to represent the E_{loss} as a function of the unit time t:

$$E_{loss} = P_g t - t\left(sin\,\alpha + \frac{a}{g}\right) Wv - P_{ml} t \tag{2.25}$$

where a denotes the acceleration of the vibratory roller, α is the slope angle, W (KN) and v (m/s) is the total weight and velocity of the roller, respectively. Then the MDP can be calculated according to Equation (2.26):

$$MDP = P_g - Wv\left(Sin\,\theta + \frac{a}{g}\right) - (mv + b) \tag{2.26}$$

where m (kJ/s) and b (kJ/s) are the internal loss coefficients of machine, respectively.

2.3.6. Oscillatory

Near-surface compaction is a significant technique that can be applied for fields such as dams and high-density buildings to avoid the impacts of dynamic vibration on nearby constructions. Oscillatory roller plays an important role in near-surface compaction, including an oscillating and vibrating drum.

The oscillating drum enables horizontal load application, resulting in a lower compaction depth than the same weight and size vibration roller, which is an ideal selection for asphalt construction. Furthermore, the asphalt requires a significantly smaller thickness which can be compacted by producing a horizontal load to make very smooth and homogenous layered soil (Pistrol et al., 2015). Besides, it adopts sensitive areas such as the bridge or inner city because of its significantly smaller ambient vibrations.

Figure 2.10 illustrates the oscillatory roller drum excitation behaviour, the two eccentric masses with the same eccentricity rotate in the same direction with a 180° mounting shift to cancel the vertical and horizontal forces (Adam and Pistrol, 2016). Without two orthogonal direction loads, a drum axis has a sinusoidal moment that leads the torsional motion in rapid forward-backward rotation.

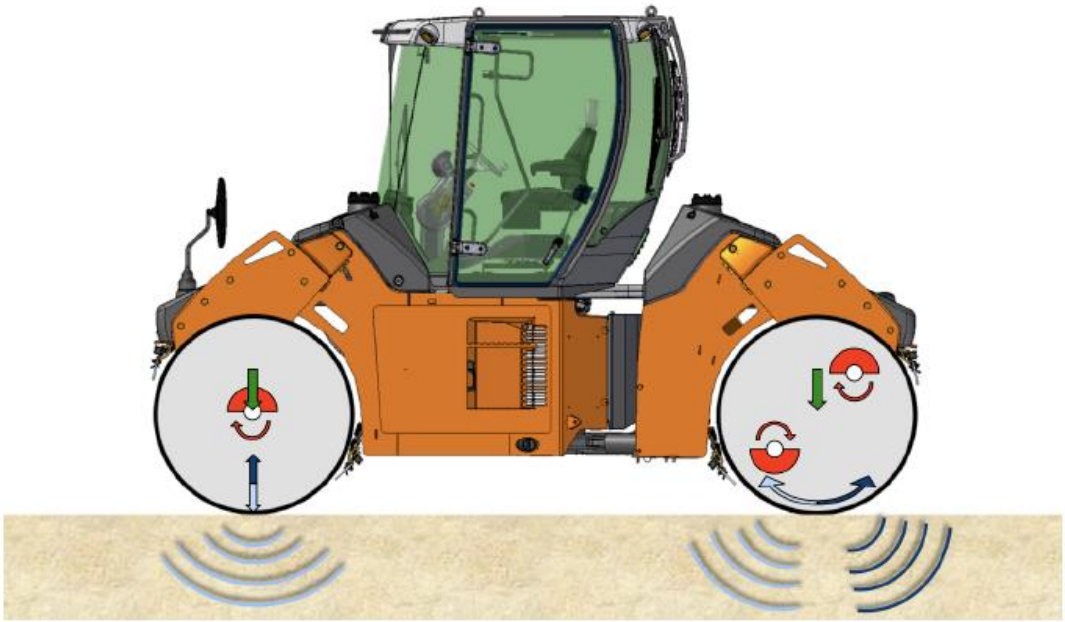

Figure 0.10 The sketch of dynamic drum structure with a right-hand side oscillating drum and left-hand side vibrating drum (Pistrol et al., 2013)

The oscillatory roller's main principle is transmitting tangential force into the underlying layer, such as the friction between the layered soil surface and vibration drum, the total weight of the roller frame. The shear stresses are the primary impact factor for oscillatory roller soil compaction.

2.4. Numerical Models for Roller Data Interpretation

The captured soil properties underneath the vibratory drum have revealed complex nonlinear responses with irregular behaviour for the soil-drum system (Anderegg and Kaufmann, 2004). Therefore, applying accurate and robust numerical models to address the interaction between soil and drum is important. US Department of Transportation (US DOTs) (Torres and Arasteh, 2017) identified five levels and precisions for roller data interpretation, i.e. (i) empirical models based on frequency response, (ii) empirical energy models with rolling resistance, (iii) simplified static mechanistic models, (iv) dynamic mechanistic models and (v) dynamic models with artificial intelligence (Table 2.2).

The empirical solutions, according to the frequency responses and rolling resistance, are the most basic ICMVs, which require specific machine parameters such as energy loss and machine movement angle. These empirical approaches are computationally time-consuming and very sensitive to machine parameters, which are complex to determine. In more recent studies (Beainy et al., 2014; Adam and Pistrol, 2016), the dynamic roller behaviour is employed to assess the compaction quality according to the roller vibration displacement, velocity and acceleration.

Table 0.2 Five levels and precisions for roller data interpretation (modified after Torres and Arasteh, 2017)

Level	Description	Measurement value	Correlation	Model type
1	Empirical models based on frequency response	Harmonic ratio	Poor or week	N/A
2	Empirical energy models with rolling resistance	Energy index	Poor or weak	Dynamic/static
3	Simplified static mechanistic models	Stiffness, modulus, the resistance force	Satisfactory	Dynamic
4	Dynamic models	Modulus, the resistance force	Good	Dynamic
5	Dynamic models with artificial intelligence	Modulus, density	Excellent	Dynamic

The numerical models, such as physical-based models, have been applied in commercially available IC rollers in the past to develop predictive models analysing roller-soil systems, such as lumped parameter model (Krober et al., 2001; Anderegg and Kaufmann, 2004), Discrete Element Model (DEM) (Smith and Peng, 2013), Boundary Element Model (BEM) (Mooney and Facas, 2013), or FEM (Fathi et al., 2018; Zhu et al., 2018; Kenneally et al., 2015; Xu et al., 2022a). Among the approaches mentioned above, the lumped parameter model is the simplest, which can rapidly provide results but requires time-consuming site-specific calibration. DEM is capable of capturing the performance of vibratory roller on the granular soils; but the computational time are prohibitive at realistic scales. BEM can efficiently reduce the executive time by decreasing the complexity of the model dimensionality, but the operated information, roller parameters and the plastic responses of the compacted soil have to be solved with iterative computations and indirect means to adjust soil responses. FEM has been used more frequently to capture the complex geometries,

boundary conditions and nonlinear interaction between the vibratory drum and soil strata in recent studies.

2.4.1. Lumped Parameter Model

The mass-spring dashpot lumped parameter model is commonly applied to characterise the soil-drum system to simulate the procedure of roller compaction, which transforms the vibrated load into compacted soil from the loose state into the dense state. Figure 2.11 represents a three-degree-of-freedom (3DOF) Kelvin-Voigt spring-mass-dashpot model to capture the composite stiffness of the underlying layers during roller compaction.

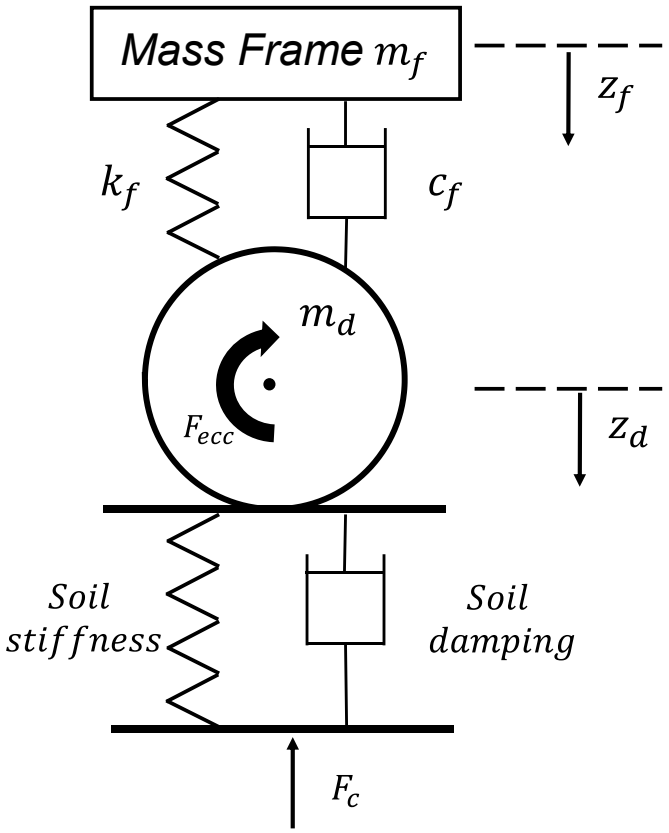

Figure 0.11 The lumped parameter three-degree-of-freedom (3DOF) spring-mass-dashpot model explaining simplified roller-soil system

Yoo and Selig (1979) provided a two-degree-of-freedom (2DOF) model to represent the steady-state frame and vertical drum kinematics in early efforts. The modelling conditions were considered as keeping full contact between the soil and drum with linear viscous damping and parallel a linear spring to emulate soil stiffness; however, the drum loses contact with soil is commonly generated in the field, which more than half of the time in practice (Mooney, 2010). Therefore, Adam (1997) and Anderegg (1997) applied the lumped parameter approaches to address the different roller modes during compaction, such as chaotic and nonlinear vibratory.

Then, Anderegg (1997) clarified the rocking and jump modes of vibration as chaotic states which occurred above certain combinations of the soil modulus and centrifugal force. Furthermore, Anderegg and Kaufmann (2004) experimentally indicated that the chaotic vibration and periodic loss of contact vibration result in a nonlinear signal in jump mode exhibiting a periodic and subharmonic vibration phenomenon. This phenomenon can be controlled by adjusting the centrifugal force via a feedback control system to prevent the operator's danger and harm to the machine.

More recently, Van Susante and Mooney (2008) have illustrated both 3DOF and 4DOF nonlinear models to recognise the dynamic behaviour between soil and drum during roller compaction. In addition. Mooney (2010) represented the lumped parameter model to reflect the compacted soil responses during the decoupling of the drum. To capture the partial loss of contact behaviour during roller compaction, the relationships between the soil, the frame and the drum can be represented by Equations (2.27) to (2.29), and the downward direction is positive.

$$\ddot{z}_d = \frac{m_0 e_0 \omega^2 sin\,(\omega t) - k_{df}(z_d - z_f) - c_{df}(\dot{z}_d - \dot{z}_f)}{m_d} + g \tag{2.27}$$

$$\ddot{z}_s = \frac{m_s g - k_s z_d - c_s \dot{z}_d}{m_s} \tag{2.28}$$

$$\ddot{z}_f = \frac{m_f g + k_{df}(z_d - z_f) + c_{df}(\dot{z}_d - \dot{z}_f)}{m_f} \tag{2.29}$$

The correlation between the calculated stiffness and measured stiffness reveals the positive when applying the lumped-parameter models to calculate the soil stiffness derived from the force-displacement hysteresis curves.

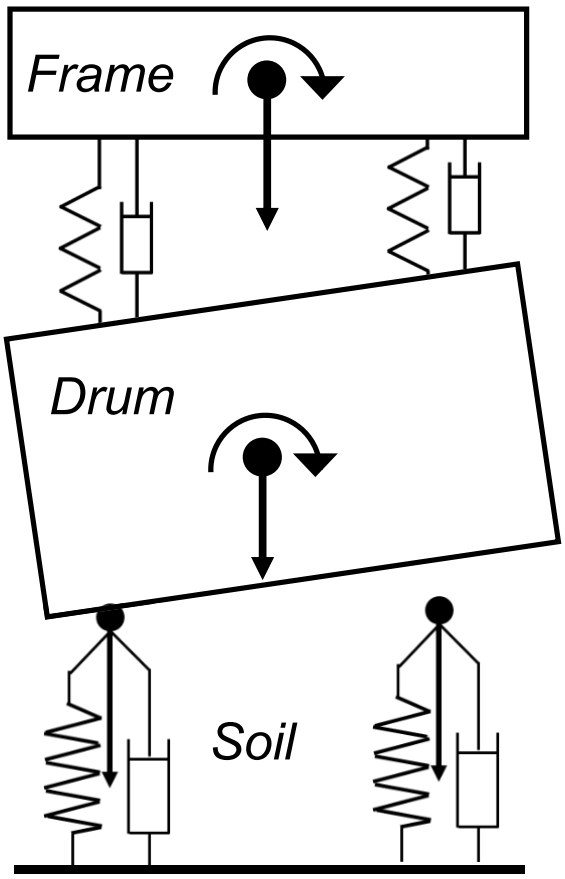

Figure 0.12 The rocking mode of the lumped parameter model (modified after Facas et al., 2010)

The extraction of the compacted geomaterial modulus is evaluated according to the behaviour of the drum; however, the drum's rocking motion is negligible. Therefore,

Facas et al. (2010) proposed a model to extract the compacted soil stiffness under partial uplift and rocking motion conditions.

Figure 2.12. demonstrates the rocking behaviour of the lumped parameter approach, where the right and left are respectively modelled as the individual degree of freedom to adapt to the different soil stiffness beneath different sides of the drum. The proposed model was validated with laboratory and field-collected data from Sakai SV510D intelligent compaction roller.

Table 2.3 summarises the various methods and results of previous research that applied the lumped parameter methods for roller compaction modelling.

Table 0.3 Summary of research applying the lumped parameter model

Bibliography	**Method and objective**	**Description and results**	**Model conditions**
Facas et al. (2010)	The multi-degree of freedom model was employed to evaluate the effects of rotational motion on the compacted layered geomaterial modulus.	The proposed approach was established to model the rotational kinematics of the compaction roller. The predicted results were compared with the Sakai vibratory roller, which exhibits that the model is capable of addressing the difference between the acceleration and phase of the vibratory roller on both the right and left sides during compaction.	The total mass of roller: $7{,}000\ kg$ Eccentric mass: $4.21–9.74\ kg.m$ Frequency: $20-35\ Hz$ Frame inertia: $1{,}696\ kg.m^2$ Drum inertia: $2{,}174\ kg.m^2$
Beainy et al. (2014)	The viscoelastic-plastic (VEP) model was applied to predict the stiffness of asphalt pavements.	In the viscoelastic-plastic model, rubber dampers are employed to connect the frame and drum to isolate the influences of drum vibration on the frame. The simulated results represent that the newly proposed VEP method is able to	Drum width: $2.0\ m$ Roller mass: $6{,}596\ kg$ Eccentric rotational frequency $50\ Hz$

		simulate the compaction level with agreeable accuracy.	Suspension drum/frame (stiffness) $3{,}400\ N/m$ Suspension drum/frame (damping) $544\ N/m$
Li et al. (2018)	The 5DOF lumped parameter model was applied considering the impacts of the roller frame on its horizontal vibration to analyse the oscillating wheel on the amplitude-frequency characteristics.	The dynamic model is developed to simulate the soil-whole machine system to investigate the proposed roller's characteristics during compaction. The developed 5DOF model exhibits that the frame's horizontal vibration significantly influences the swing amplitude of the oscillating wheel.	The front wheel: Stationary The rear wheel: Oscillating Total mass of roller: $12{,}000\ kg$ Frequency: $5 - 44\ Hz$
Paulmichl et al. (2019)	The three-degree-of-freedom lumped parameter model was applied to estimate the oscillation roller.	Findings from the proposed model can be employed to establish the relationship between the compaction level of soil and the area inside the $\ddot{x}_M - \ddot{z}_M$ plot.	Drum radius: $0.6\ m$ Drum width: $1.68\ m$ Drum mass: $1{,}851\ kg$ Drum inertia $411.78\ kg.m^2$ Excitation frequency $39\ Hz$ Suspension drum/frame (stiffness) $4 \times 10^6\ N/m$ Suspension drum/frame (damping) $3 \times 10^3\ N/m$

2.4.2. Discrete Element Model (DEM)

DEM as a specialised methodology has been extensively adopted to deal with the relation between the discontinuous nature of granular materials and structure. DEM,

as an explicit time-stepping algorithm, has utilised the rigid elements to discretise the material into simple shapes and study the interaction between neighbouring elements based on the interaction laws (Tavarez and Plesha, 2007). Early efforts of DEM were put forward by Cundall (1971), who first theoretically introduced the numerical approach to study rock mechanics based on the relationship within the internal particles of soil to study the behaviour of granular soil under macroscopic mechanical level. The internal structure of deformable material is microscopic and represented by an assembly of discrete blocks with various shapes.

In addition, Buechler et al. (2012) explored the setup of a numerical method to give a basic understanding of particle kinematics, which follows three principal analytical steps: (a) internal force evaluation; (b) integration of equations of motion and (c) contact detection. Newton's second and force-displacement laws are alternately utilised to evaluate the interaction of elements (Tavarez and Plesha, 2007). Therefore, the proper constitutive model is required to precisely describe each block's contact behaviour during the moving process.

The measurements from the numerical method exhibit reasonable results on using the DEM to address the interaction of the soil-drum system. The model can accurately model macroscale features by analysing the drum-soil contact width, their contact strain and stress distributions, and variable microstructure and interactions. For instance, Micaelo et al. (2010) employed a two-dimensional DEM to address the roller compaction on the field, and the proposed method showed that the predictions agreed reasonably with the field data. Besides, Wang et al. (2007) applied a three-dimensional discrete element software, Particle Flow Code (PFC3D), to study the compaction mechanisms.

2.4.3. Boundary Element Model (BEM)

The BEM is a powerful computational method for compacted geomaterials displacement and stress analysis. Mooney and Facas (2013) assessed the impacts of the beneath compacted soil support related to IC modulus and interaction between soil and drum during compaction through BEM of a smooth single drum compaction roller. The compacted soil profile consisting of the silty sand and crushed rock was modelled, indicating that the underlying soil stiffness is dependent on the lower Young's modulus of the impacts of underlying support and compacted layer. Furthermore, Musimbi et al. (2010) applied an iterative computational procedure for estimating the contact width by combining BEM and roller-drum geometry. The proposed method agrees reasonably with Hertz's theory simulations on half space of the sandy materials. The authors also examined the contact width dependency on layer characteristics and concluded the influences on the soil-drum contact problem for the stiffer materials.

2.4.4. Finite Element Model (FEM)

FEM is an effective tool based on integral and differential analysis and the primary mechanistic approach for solving complicated engineering problems. Generally, the concept of the FEM can be explained as using lots of interconnected subregions and small elements to describe a complex geometrical shape, where an approximate and more straightforward solution can be approximately found from these composed pieces (Rao, 2017). Therefore, the FEM technique has been customary to analyse advanced drum-soil interaction.

Different finite element models have been employed, such as two-dimensional and three-dimensional approaches, which can be applied to investigate the interactions of

soil and drum; however, the precision of computational results might be different because of the modelling complexity. In addition, the measured results could be impacted by the different types of constitutive soil models, such as linear elastic, National Cooperative Highway Research Program (NCHRP) model, and HS-Small. Several researchers used the FEM, adopting a continuum-based computational technique to explain the interaction mechanism between drum and soil (Xu et al., 2012; Erdmann and Adam, 2014; Kenneally et al., 2015; Herrera et al., 2018; Fathi, 2020; Nazarian et al., 2020). Applying the linear elastic model can efficiently simplify the soil-drum structure as well as the computational time with reasonable results. Mooney and Facas (2013) illustrated the interactions of soil and drum by a 2D plane strain dynamic linear elastic model. The constant 30 Hz vibratory frequency was applied to produce the vertical harmonic force located at the centre of the rigid cylinder. In addition, the infinite boundary elements were used to avoid unnormal reflections and absorb wave energy. To calibrate the results of FEM simulations, the independent LWD test was applied to measure soil modulus, and the ICMVs on layered soil were fitted to the experimental results.

In addition, Kenneally et al. (2015) applied a 2D FEM adopting a linear elastic constitutive soil model for a uniform soil profile to explore the impacts of the compacted layer modulus and thickness on the dynamic response of the roller. FEM was developed using ABAQUS to evaluate the relationship between the ICMVs and the compacted soil stiffness. The soil's constitutive properties were meshed using 20 mm square uniform linear elastic finite elements with infinite boundary conditions to quantify the radiation-damping effects. The roller was modelled as a 0.75 m radius rigid cylinder with a static weight (16.35 kN) and a varied vertical harmonic excitation

force. A discontinuous frictionless surface boundary constraint was activated to acquire the nonlinear interaction of the vibratory roller and layered geomaterial. The numerical model was proven to capture the contact force and roller displacement characteristics on the compacted geomaterial surface and the relationship of roller time-varying loading after calibrating against two construction field compaction data.

Although the 2D finite element model is computationally less expensive, many studies are interested in 3D modelling to investigate the drum characteristics of soil reflections. Kim et al. (2009) illustrated both the axisymmetric and full 3D FE modellings via the ABAQUS program to explore the compacted pavement responses. A nonlinear stress-dependent constitutive model, NCHRP model, was applied to find geomaterial stiffness under the repeated roller load stress. The findings indicated the proper 3D FE modelling with the nonlinear stress-dependent constitutive model, significantly affecting precise simulations of critical pavement reflections.

A different dynamic 3D FE program called LS-DYNA was chosen by Carrasco et al. (2014) to analyse the drum and soil interaction behaviour. In the study, a drum modelled as a 0.75 radius rigid cylinder with a 2 m length, vibrating on a 2.5 m in-depth geomaterial. The underlying material meshed as $50 \times 50 \times 50$ mm brick elements. The constant 30 Hz harmonic frequency was distributed uniformly on the roller, providing a sinusoidal dynamic eccentric force. Rayleigh damping was applied to emulate underlying geomaterial damping.

According to the previous literature review, establishing a robust FEM can efficiently capture close results while calibrating with construction field data. Thus, developing

accurate roller-soil interaction behaviour with the appropriate constitutive model is significant.

2.5. Underlying Soil Constitutive Models

The main object of using a numerical method for investigating the interactions is addressing the behaviour of the vibratory drum and underlying soil. Therefore, accurate stress-strain relationships are required to account for soil characteristics. Several constitutive models have been increasingly proposed in previous studies, such as linear elastic, Mohr-Coulomb, NCHRP model and HS-Small to simulate the features and properties of the underlying soil.

2.5.1. Linear Elastic Constitutive Model

Linear elastic soil has been widely used in soil-drum interaction analysis, which can significantly simplify the soil responses to avoid some theoretical and computational limitations. Hooke's law of linear stress-strain relation is the main concept of a linear elastic model.

2.5.2. Elastic-Plastic Constitutive Model

Mohr-Coulomb is an elastic-perfectly plastic model according to Poisson's ratio, ν, and elasticity modulus, E, and using the friction angle, φ, and cohesion, c, to represent the failure criteria. Referring to Figure 2.13, Mohr-Coulomb's plastic behaviour can be expressed by the three-dimensional stress space model; however, Nazarian (2020) indicated that this model is cumbersome in finite element coding and the Drucker-Prager criterion is provided using a modified Mohr-Coulomb model

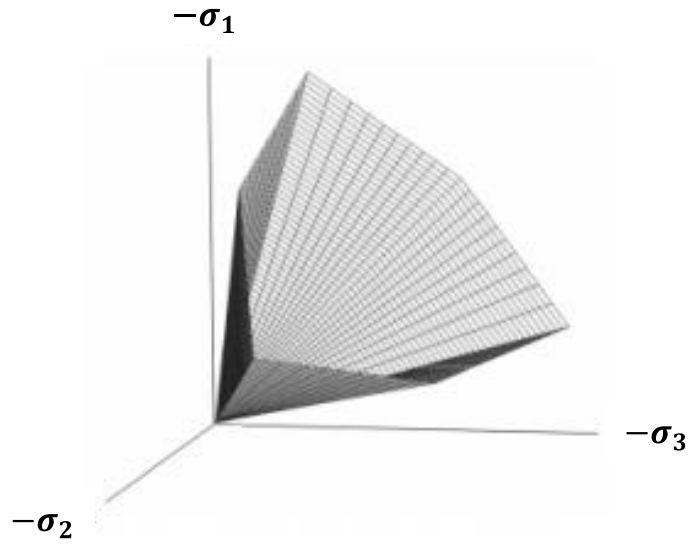

Figure 0.13 A Mohr-Coulomb yield surface (Ti et al. 2009)

The Drucker-Prager is instrumental in increasing the modelling stability, and its plastic yielding starts while the critical combination is reached by the second stress and the mean stress (Nazarian, 2020). Equations (2.30) to (2.32) exhibit plastic-yielding behaviour:

$$f(I_1,J_2) = \alpha I_1 + \sqrt{J_2} - k \tag{2.30}$$

$$I_1 = \sigma_1 + \sigma_2 + \sigma_3 \tag{2.31}$$

$$J_2 = \frac{1}{2}\sigma_{ij}^{dev}\sigma_{ji}^{dev} = \frac{1}{6}[(\sigma_3 - \sigma_1)^2 + (\sigma_2 - \sigma_3)^2 + (\sigma_1 - \sigma_2)^2] \tag{2.32}$$

where I_1 and J_2 are the primary and the second invariant stress tensor; σ_1, σ_2, σ_3 represented the greatest, intermediate and least stress, respectively. In terms of stress senor σ_{ij}^{dev}, the following equation can be applied to define:

$$\sigma_{ij}^{dev} = \sigma_{ij} - \frac{I_1}{6}\delta_{ij} \tag{2.33}$$

where δ_{ij} is the Kronecker delta.

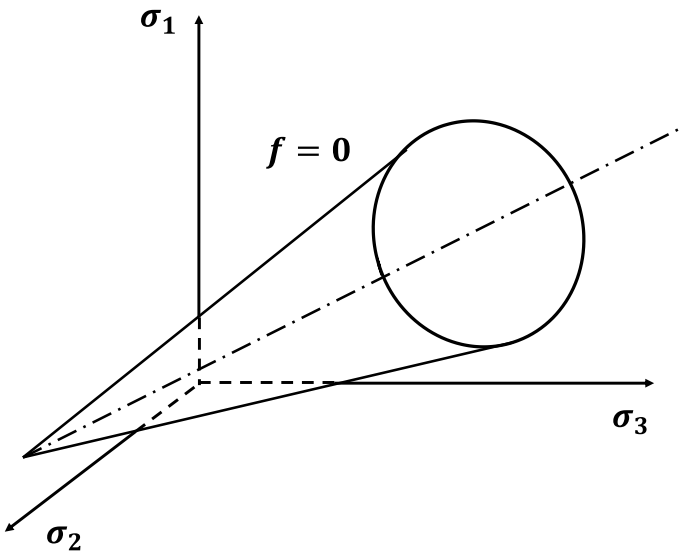

Figure 0.14 The Drucker-Prager yield surface in principal stress (modified after Yesuf, 2014)

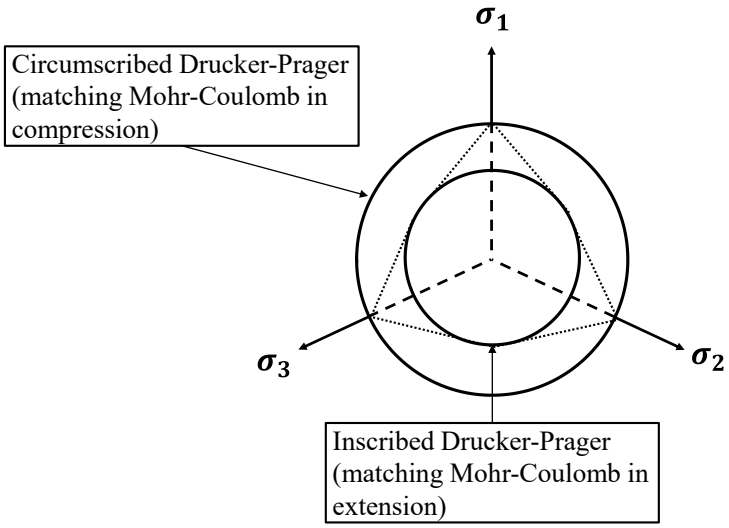

Figure 0.15 The comparison between the Mohr-Coulomb and alternative Drucker-Prager surface (modified after Yesuf, 2014)

Figures 2.14 and 2.15 demonstrate the graphical presentation of the Drucker-Prager yield surface and the comparison between the Mohr-Coulomb and alternative Drucker-Prager surfaces.

The model parameters α and k decided from the triaxial shear tests and simulated by finding the interactions of the Mohr-Coulomb and Drucker-Prager yield functions in 3D space, explained by Equations (2.34) and (2.35)

$$\alpha = \frac{2sin\varphi}{\sqrt{3}(3 - sin\varphi)} \tag{2.34}$$

$$k = \frac{6csin\varphi}{\sqrt{3}(3 - sin\varphi)} \tag{2.35}$$

The Drucker-Prager failure criterion has been widely used by Kim (2010), Li and Su (2014) Yesuf (2014) to research vibrated roller and layered soil behaviour in finite element modelling.

2.5.3. Hardening Soil and Hardening Soil with Small Strain Stiffness Models

Ti et al. (2009) indicated that the cap hardening and friction hardening in the HS model is assessed to account for plastic volumetric strain and plastic shear strain. Figure 2.16 illustrates the yield contour of the model in 3D space.

HS-Small model can evaluate stress-dependent and plasticity-induced soil stiffness degradation (Benz, 2007; Schanz et al., 1999). Referring to Brinkgreve et al. (2016), three major factors can be employed to characterise the soil behaviour, including (i) the one-dimensional (1D) tangent stiffness modulus (E_{oed}), (ii) the stress-dependent stiffness modulus for highly nonlinear primary deviatoric loading (E_{50}), and (iii) the unloading and reloading stress-dependent stiffness (E_{ur}), as expressed in Equations (2.36) to (2.38), respectively.

$$E_{oed} = E_{oed}^{ref}\left(\frac{c\,cos\varphi - \frac{\sigma_3'}{K_0^{nc}}sin\varphi}{c\,cos\varphi + p^{ref}sin\varphi}\right)^m \quad (2.36)$$

$$E_{50} = E_{50}^{ref}\left(\frac{c\,cos\varphi - \sigma_3' sin\varphi}{c\,cos\varphi + p^{ref}sin\varphi}\right)^m \quad (2.37)$$

$$E_{ur} = E_{ur}^{ref}\left(\frac{c\,cos\varphi - \sigma_3' sin\varphi}{c\,cos\varphi + p^{ref}sin\varphi}\right)^m \quad (2.38)$$

where E_{50}^{ref}, E_{ur}^{ref} and E_{oed}^{ref} are the secant, unloading/reloading and tangent stiffness related to the reference pressure p^{ref} (a default setting of p^{ref} = 100 kPa), respectively; K_0^{nc} is the stress ratio in primary compression; m is the factor defining the level of stress dependency; σ_3' prime is the minor principal stress.

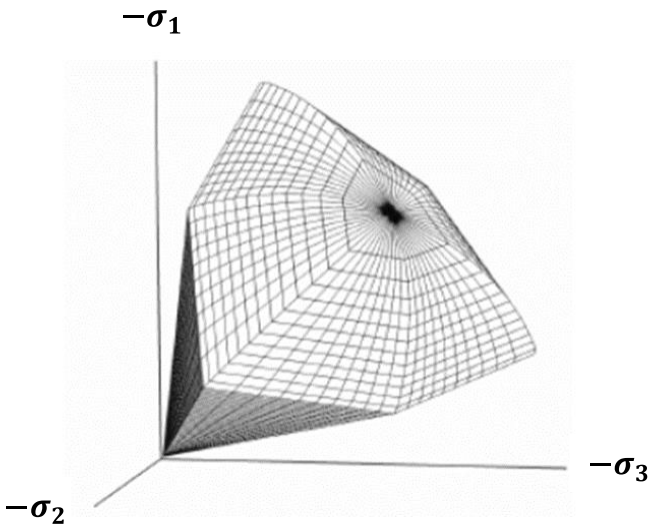

Figure 0.16 The HS mode yield surface in principal stress (modified after Yesuf, 2014)

The HS-Small model can exhibit the nonlinear behaviour of the natural subsoil in the small and large strain ranges. Additionally, the HS-Small model is favourable to simulating the modulus degradation of the soil and damping characteristics with the cyclic shear strain mobilised in the soil (Benz et al., 2009). The HS-Small model can simultaneously consider hysteretic soil damping (at small strains) and soil plasticity

behaviour (at large strains). The function developed by Hardin and Drnevich (1972), was utilised to represent the correlation between the cyclic shear strain (γ_c) and secant shear modulus (G_s) in this study, is expressed as below;

$$G_s = \frac{G_0}{1 + \frac{\alpha\gamma_c}{\gamma_{0.7}}} \tag{2.39}$$

where, parameters G_0 and $\gamma_{0.7}$ represent the small-strain shear stiffness and the shear strain at which the secant shear modulus (G_s) is reduced to $0.7G_0$, respectively. The recommended value for α, resulting in good agreement with laboratory measurements, is 0.385 (Hardin and Drnevich, 1972).

2.5.4. NCHRP Model

Resilient modulus (M_R) is a nonlinear stress-dependent geomaterial basic mechanical property, which is commonly clarified as the ratio of repeatedly employed wheel deviator stress, σ_d, to recoverable elastic strain, ε_d. In the laboratory, the triaxial tests are generally applied to simulate the value of M_R of cohesive subgrade soils (Kim et al., 2009). The Mechanistic-Empirical Pavement Design Guide (MEPDG) employs a modified version of Uzan's constitutive equation (Uzan et al., 1992) to develop the correlation between the M_R and stress state, which was advocated by the NCHRP. Referring to Nazarian et al. (2020), in a mechanistic-empirical (M-E) pavement design guide, M_R is utilised as the main pavement design parameter, which is defined as:

$$M_R = k_1 P_a (\frac{\theta}{P_a})^{k_2} (\frac{\tau_{oct}}{P_a} + 1)^{k_3} \tag{2.40}$$

$$\theta = \sigma_1 + \sigma_2 + \sigma_3 \tag{2.41}$$

$$\tau_{oct} = \frac{1}{3}\sqrt{(\sigma_3 - \sigma_1)^2 + (\sigma_2 - \sigma_3)^2 + (\sigma_1 - \sigma_2)^2} \quad (2.42)$$

where M_R is the resilient modulus; θ is the normal bulk stress; τ_{oct} is the octahedral shear stress; and P_a is the atmospheric pressure. k_1, k_2, k_3 are parameters from laboratory triaxial test data.

The nonlinear stress-dependent resilient modulus constitutive equation has been widely incorporated into mechanistic underlying soil analysis via FEM to research the soil responses beneath the vibratory roller. Kim et al. (2009) developed a FEM using the resilient modulus constitutive equation to properly simulate the unbound aggregate base soil layer characterisations. The simulating results precisely capture the nonlinear layered soil responses. Besides, Carrasco et al. (2014) employed a resilient modulus FEM to research the sensitivity and theoretical limitations of the continuous compact control by correlating to the LWD modulus-based device.

2.6. Extraction of Soil Stiffness Using Intelligent Compaction

Mooney and Facas (2013) analytically utilised a combination of the forward modelling and inverse method to back-calculate the soil properties. The roller dynamic load model is explicitly applied to the simulated cylindrical drum. The forward method includes boundary element and continuum-based FE analysis to simulate the drum and soil behaviour during roller compaction.

The model emulates one of the linear or nonlinear behaviours of soil under dynamic loading, particularly variations of damping and soil stiffness with the cyclic shear strain induced by the applied load. Although the forward method can predict the

lumped behaviour on the soil-drum system, this method only calculates the composite stiffness values and cannot analyse the individual layer properties.

Furthermore, a simulation of individual layer properties can be supported by the inverse method; namely, the back-calculation method, which is capable of extracting the single-layer elastic modulus from intelligent compaction roller measured data. Figure 2.17 indicates a procedure of the back-calculation method, the simulation of each layer modulus for a multiple-layer system progression that starts from the bottom layer and moves left to the right.

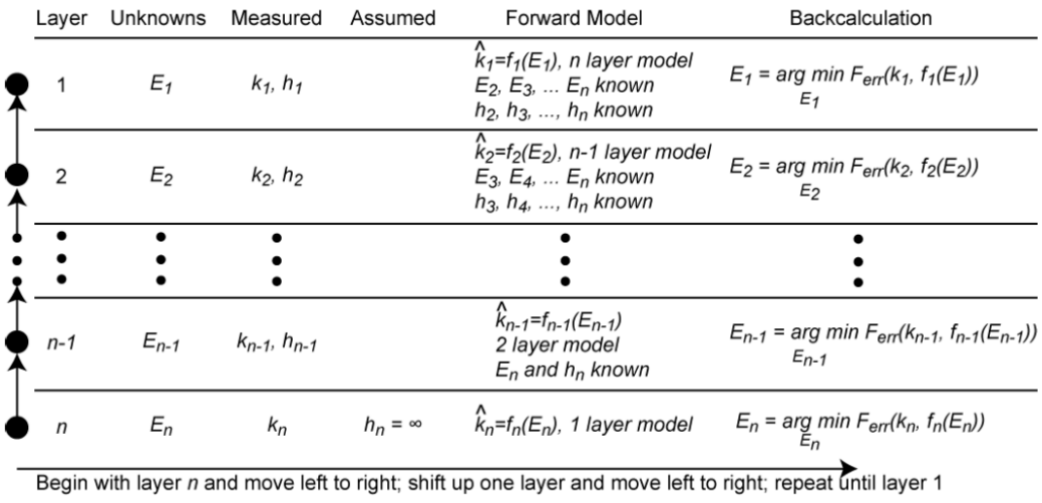

Figure 0.17 The procedure of the inverse method (Mooney and Facas, 2013)

The inverse method starts from the base layer n, which can be seen as the 1.0 – 2.0 m thick subgrade layer, and it is assumed as a half-space and semi-infinite. Then, a finite element modelling (forward method) will be employed to establish a function based on the soil-drum system, which relates to the roller-measured stiffness (k_n) and the modulus of the subgrade layer (E_n), providing a correlation between predicted soil stiffness ($\hat{k}$) and Young's modulus of the layer E_n, i.e. $\hat{k} = f_n(E_n)$.

In this investigation, homogeneous, isotropic and linear elastic soil conditions are considered to decrease the errors that could occur during forwarding modelling. Then an error function will be employed to minimise the error between the roller-measured stiffness k_n and the FEM predicted stiffness ($\hat{k}_n$). The extracted layer modulus can achieve the best estimated E_n after minimising the error.

A two-layer model (layer n & $n-1$) can be modelled after extracting the bottom layer properties with a second layer function f_{n-1} which relies on the thickness of underlying layer n and upper layer $n-1$ and the stiffness on E_{n-1} and E_n. The thickness of layer n-1 can be determined by using GPS with an accuracy of around 10 mm from the vibratory roller operating on the bottom layer. Based on the known h_{n-1} and E_n. f_{n-1} is only corresponding to the unknown value E_{n-1}.

According to the previous method, E_{n-1} can be determined after comparing the FEM predicted $\hat{k}_{n-1}$ to the measured k_n in error minimising function. This inverse calculation procedure can be continued to the upper layer with forwarding modelling to the top layer. Equation (2.43) is used to represent the secant method to inverse calculate the top layer modulus, E_1.

$$F_{err}(E_1) = k - f_1(E_1) \tag{2.43}$$

where f_1 can be represented as the function of E_1, and $h_1$and E_2 are assumed known values. Where E_1 can be evaluated as (integer value i indicates the current iteration)

$$[E_1]_{i+1} = \frac{-[E_1]_i + [E_1]_{i-1}}{F_{err}([E_1]_{i-1}) - F_{err}([E_1]_i)} F_{err}([E_1]_i) + [E_1]_i \tag{2.44}$$

where $[E_1]_i$ is the value of E_1 after the i^{th} iteration.

2.7. Summary and Gap Identification

The review of current literature shows that roller compaction, as one of the most common procedures in construction projects, is required to provide a well-compacted multi-layered pavement structure to stabilise the subgrade and distribute the dynamic vehicular loads from the trains or vehicles to the ground, while minimising surface deformation. Although in-situ testings are commonly used for predicting the properties of compacted soil, the discrete testing locations cannot precisely assess the full-area compaction level and potentially remain regions inaccessible.

Implementing the intelligent soil compaction technique has recently gained increasing interest during earthworks due to its desire to adjust the number of passes or roller frequency to consistently satisfy the early pavement deterioration and prescribed soil stiffness requirements. Various ICMVs could represent it by evaluating the uniformity of the compacted region and correlating it to geomaterial for its physical and mechanical characteristics.

The physical models are generally considered the important technique to capture the drum characteristics and the properties of underlying geomaterial to predict the interactions of soil and drum. The simplified numerical model based on the added mass technique for soil modelling to evaluate the roller-integrated experimental data exhibits relatively good results; however, due to the excessively simplified assumptions for dissipative and inertial properties in this model, a site-specific calibration would be necessary.

Additionally, the DEM can simulate the soil-structure interaction and evaluate the mechanical responses and macroscopic deformations based on microstructural

interactions. However, the very long computational time for DEM does not yet allow this technique to be used for the real-time assessment of compaction levels.

In recent years, finite element methods are gaining greater popularity in adopting a continuum-based computational technique to explain the interaction mechanism between drum and soil. They have been proven capable of considering more realistic geometries and boundary conditions to capture the cumulative plastic deformation during cyclic loading.

The majority of finite element studies simulating the dynamic behaviour of roller-drum interaction have explicitly considered the linear elastic or viscoelastic soil models. Extensive previous studies have consistently shown the criticality of accounting for soil nonlinearity under cyclic loading conditions, particularly when soil deformation or reaction forces need to be predicted. Furthermore, FEM can provide the determination of the uniformity level of compaction over large areas according to the dynamic drum response, however accurate real-time determination of geomaterial stiffness during compaction based on roller acceleration impacted by soil characteristics has been challenging due to the multi-layered composite nature of the soil and the nonlinearities of the dynamic equation of motion and soil response.

In addition, practicing engineers need accurate constitutive models with fewer parameters obtained from common geotechnical tests or from the existing correlations to other soil parameters. Thus, a reasonable soil constitutive model needs to capture the cumulative plastic deformations during cyclic loading.

Chapter 3

Details of Extended Support Vector Regression (X-SVR) for Machine Learning

3.1. Introduction

To real-time extract the compacted soil stiffness, the X-SVR machine learning method was applied in this study; hence the main aspects of the developed approach are explained here.

The kernelised surrogate model X-SVR was applied in conjunction with orthogonal polynomial kernel function Generalised Gegenbauer kernel (GGK) and Gaussian kernel in approximating the function of the dynamic interactions between compacted soil and vibratory drum. The first-passage failure theorem underpins the analysis framework of the X-SVR. After the development of the proposed algorithm with a

specific kernel, the limit state function was adopted, which is capable of being explicitly approximated from the obtained results (Feng et al., 2019).

Moreover, by offering the sampling schemes, the X-SVR method can efficiently provide the probability density functions, the statistical moments, and the cumulative distribution functions. In addition, by means of applying the identical size of training datasets, the adopted X-SVR is able to construct a more accurate regression model between the inputs and outputs when compared with classical Support Vector Regression (SVR) (Wang et al., 2020). Furthermore, in comparison with conventional Support Vector Machine (SVM), satisfying does not define the condition of Mercer as a prerequisite applied in the nonlinear proposed algorithm (Feng et al., 2019).

Additionally, the kernelised nonlinear X-SVR was introduced by extending the linear X-SVR approach with the empirical kernel map method (Scholkopf et al., 1999; Hofmann et al., 2008), which can convert the proposed linear X-SVR to a kernel-based learning method efficiently (Wang et al., 2020). It is recommended to refer to Wang et al. (2020) for an in-depth theoretical description of the X-SVR. The following section briefly introduces this machine learning approach.

3.2. Linear Extended Support Vector Regression

In typical double-class classification, the selected input $\boldsymbol{x}_{\text{train}} = [\boldsymbol{x}_1, \boldsymbol{x}_2, \boldsymbol{x}_3, \ldots, \boldsymbol{x}_m]^{\text{T}} \in \Re^{m \times n}$, and the corresponding output $\boldsymbol{y}_{\text{train}} \in \Re^{m}$, are considered as the training samples, where n indicates the corresponding input samples, m denotes the quality of the selected training dataset. The hyperplane that classifies the classes are denoted by Vapnik (1999) and Drucker et al. (1996):

$$\hat{f}(\boldsymbol{x}) = \boldsymbol{x}\boldsymbol{w}^T - \delta \tag{3.1}$$

where $\boldsymbol{w} = [w_1, w_2, \ldots, w_\ell, \ldots, w_n]^T \in \Re^n$ is the support vector, and $\delta \in \Re$ denotes the bias. Equation (3.1) could be alternatively considered as the targeted regression function.

Figure 3.1 demonstrates the ε-insensitive band for the SVR and adopted ε is the tolerance deviation between the prediction $\hat{f}(\boldsymbol{x})$ and true value $\boldsymbol{y}_{\text{train}}$.

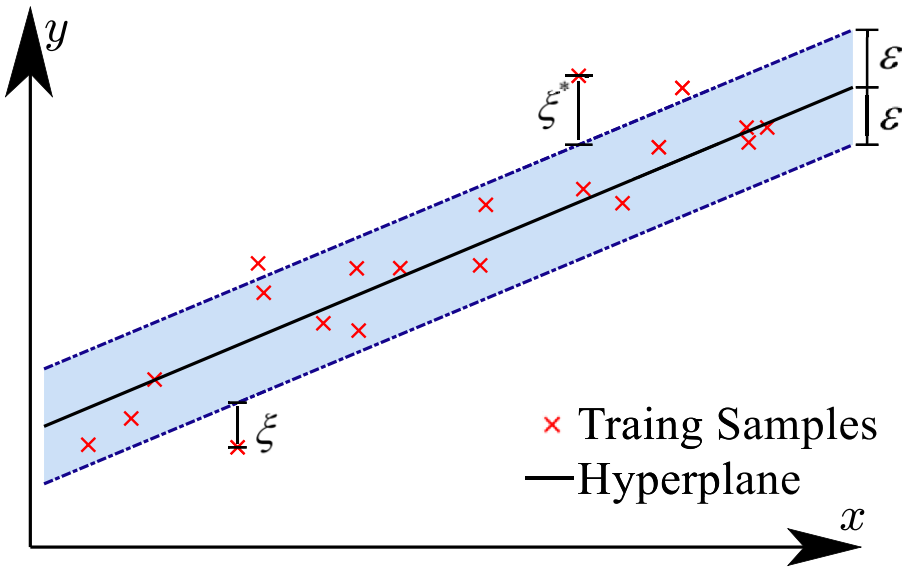

Figure 0.1 The ε-insensitive band for a 1D linear regression function

The linear regression function Equation (3.1) could be alternatively considered as solving the following mathematical programming problem:

$$\min_{\boldsymbol{w},\delta,\xi^*,\xi} : C\sum_{i=1}^{m}(\xi_i^* + \xi_i) + \frac{1}{2}\|\boldsymbol{w}\|_2^2 \tag{3.2a}$$

$$\text{s.t.}\begin{cases} y_i + \delta - \boldsymbol{x}_i\boldsymbol{w}^{\mathrm{T}} \le \xi_i^* + \varepsilon \\ y_i - \delta + \boldsymbol{x}_i\boldsymbol{w}^{\mathrm{T}} \le \xi_i + \varepsilon \\ \xi_i^*, \xi_i \ge 0 \end{cases} \tag{3.2b}$$

where $\|\bullet\|_2$ is the L_2-norm of $\bullet$; $C \in \Re^+ := \{x \in \Re \mid x > 0\}$ represents the penalty constant; ξ_i, ξ_i^*, denote the slack variables.

By implementing a similar idea presented in the doubly regularised support vector machine (Wang et al., 2006), both L_1-norm and L_2-norm penalties are applied in combination with the hinge loss function. Moreover, a decomposition process (Dunbar et al., 2010) is utilised to avoid the computation of L_1-norm $\|\boldsymbol{w}\|_1$. A quadratic ε-insensitive loss function (i.e. $l_2^{\varepsilon}(\cdot)$) is also used to increase the computational stability of the optimisation problems:

$$l_2^{\varepsilon}\left[y_i - \hat{f}(\boldsymbol{x}_i)\right] = \left|-\hat{f}(\boldsymbol{x}_i) + y_i\right|^2 \tag{3.3}$$

As a result, the governing equation for the X-SVR method is simplified and formulated as:

$$\min_{\boldsymbol{p},\boldsymbol{q},\delta,\boldsymbol{\xi},\boldsymbol{\xi}^*} : \frac{\lambda_1}{2}(\|\boldsymbol{p}\|_2^2 + \|\boldsymbol{q}\|_2^2) + \lambda_2 \boldsymbol{e}_n^T(\boldsymbol{p}+\boldsymbol{q}) + \frac{C}{2}(\boldsymbol{\xi}^T\boldsymbol{\xi} + \boldsymbol{\xi}^{*T}\boldsymbol{\xi}^*) \tag{3.4a}$$

$$s.t. \quad \begin{cases} \boldsymbol{x}_{train}(\boldsymbol{p}-\boldsymbol{q}) - \delta \boldsymbol{e}_m - \boldsymbol{y}_{train} \le \varepsilon \boldsymbol{e}_m + \boldsymbol{\xi} \\ \boldsymbol{y}_{train} - \boldsymbol{x}_{train}(\boldsymbol{p}-\boldsymbol{q}) + \delta \boldsymbol{e}_m \le \varepsilon \boldsymbol{e}_m + \boldsymbol{\xi}^* \\ \boldsymbol{p}, \boldsymbol{q} \ge \boldsymbol{0}_n \,;\; \boldsymbol{\xi}, \boldsymbol{\xi}^* \ge \boldsymbol{0}_m \end{cases} \tag{3.4b}$$

where $\lambda_1, \lambda_2 \in \Re^+$ denote two tuning parameters; $\boldsymbol{\xi}, \boldsymbol{\xi}^* \in \Re^m$ are two non-negative vectors; $\boldsymbol{e}_n = [1,1,\ldots,1]^T \in \Re^n$ and $\boldsymbol{0}_n = [0,0,\ldots,0]^T \in \Re^n$ represent one- and zero-vectors in dimensions of n; and $\boldsymbol{p}, \boldsymbol{q} \in \Re^n$ include the non-negative variables, more specifically:

$$p_\ell := (w_\ell)_+ = \begin{cases} 0, & w_\ell \le 0 \\ w_\ell, & w_\ell > 0 \end{cases} \; and \; q_\ell := (w_\ell)_- = \begin{cases} -w_\ell, & w_\ell < 0 \\ 0, & w_\ell \ge 0 \end{cases}, \quad for \; \ell = 1,2,\ldots,n \tag{3.5}$$

From the definition expressed in Equation (3.5), $p_\ell q_\ell = 0$ is guaranteed $\forall \ell$. Therefore, the $\|\boldsymbol{w}\|_1$ and $\|\boldsymbol{w}\|_2^2$ could be alternatively evaluated as:

$$\begin{aligned}\|\mathbf{w}\|_1 &= |w_1| + |w_2| + \ldots + |w_n| \\ &= p_1 + q_1 + p_2 + q_2 + \ldots + p_n + q_n \\ &= \mathbf{e}_n^T(\mathbf{p} + \mathbf{q})\end{aligned} \tag{3.6}$$

$$\begin{aligned}\|\mathbf{w}\|_2^2 &= \|\mathbf{p} - \mathbf{q}\|_2^2 \\ &= \|\mathbf{p}\|_2^2 + \|\mathbf{q}\|_2^2 - 2\mathbf{p}^T\mathbf{q} \\ &= \|\mathbf{p}\|_2^2 + \|\mathbf{q}\|_2^2\end{aligned} \tag{3.7}$$

Equation (3.4) can be simplified as:

$$\min_{\hat{\boldsymbol{z}},\delta} : \frac{1}{2}\left(\hat{\boldsymbol{z}}^T\widehat{\boldsymbol{C}}\hat{\boldsymbol{z}} + \delta^2\right) + \lambda_2\hat{\boldsymbol{a}}^T\hat{\boldsymbol{z}} \tag{3.8a}$$

$$s.t.\left(\widehat{\boldsymbol{A}} + \boldsymbol{I}_{(2m+2n)\times(2m+2n)}\right)\hat{\boldsymbol{z}} + \hat{\boldsymbol{d}} + \hat{\boldsymbol{b}}\left(\delta\widehat{\boldsymbol{G}} + \varepsilon\boldsymbol{I}_{(2m+2n)\times(2m+2n)}\right) \geq \mathbf{0}_{2m+2n} \tag{3.8b}$$

where $\boldsymbol{I}_{(2m+2n)\times(2m+2n)} \in \Re^{(2m+2n)\times(2m+2n)}$ represents an identity matrix. In addition, to provide the advantages of simultaneously optimising the location and orientation of the proposed model, a squared bias parameter (i.e. δ^2) is introduced (Dunbar et al., 2010; Mangasarian and Musicant, 2001). The matrices $\widehat{\boldsymbol{G}}$, $\widehat{\boldsymbol{C}}$, and $\widehat{\boldsymbol{A}} \in \Re^{(2n+2m)\times(2n+2m)}$ are defined as:

$$\begin{aligned}\widehat{\boldsymbol{G}} &= \begin{bmatrix}\mathbf{0}_{2n\times 2n} & \mathbf{0}_{2n\times m} & \mathbf{0}_{2n\times m} \\ \mathbf{0}_{m\times 2n} & \boldsymbol{I}_{m\times m} & \mathbf{0}_{m\times m} \\ \mathbf{0}_{m\times 2n} & \mathbf{0}_{m\times m} & -\boldsymbol{I}_{m\times m}\end{bmatrix}, \widehat{\boldsymbol{C}} = \begin{bmatrix}\lambda_1\boldsymbol{I}_{2n\times 2n} & \\ & C\boldsymbol{I}_{2m\times 2m}\end{bmatrix}, \\ \widehat{\boldsymbol{A}} &= \begin{bmatrix}\mathbf{0}_{2n\times n} & \mathbf{0}_{2n\times n} & \mathbf{0}_{2n\times 2m} \\ -\boldsymbol{x}_{train} & \boldsymbol{x}_{train} & \mathbf{0}_{m\times 2m} \\ \boldsymbol{x}_{train} & -\boldsymbol{x}_{train} & \mathbf{0}_{m\times 2m}\end{bmatrix}\end{aligned} \tag{3.9}$$

then the vectors $\hat{\boldsymbol{a}}$, $\hat{\boldsymbol{b}}$, $\hat{\boldsymbol{d}}$, and $\hat{\boldsymbol{z}} \in \Re^{2n+2m}$ can be represented as:

$$\hat{\mathbf{a}} = \begin{bmatrix} \mathbf{e}_{2n} \\ \mathbf{0}_{2m} \end{bmatrix}, \quad \hat{\mathbf{b}} = \begin{bmatrix} \mathbf{0}_{2n} \\ \mathbf{e}_{2m} \end{bmatrix}, \quad \hat{\mathbf{d}} = \begin{bmatrix} \mathbf{0}_{2n} \\ \mathbf{y}_{train} \\ -\mathbf{y}_{train} \end{bmatrix}, \quad \hat{\mathbf{z}} = \begin{bmatrix} \mathbf{p} \\ \mathbf{q} \\ \boldsymbol{\xi} \\ \boldsymbol{\xi}^* \end{bmatrix} \tag{3.10}$$

Alternatively, the dual formulation of Equation (3.8) could be used to solve as

$$\min_{\varphi} : \frac{1}{2}\boldsymbol{\varphi}^T \boldsymbol{Q}\boldsymbol{\varphi} - \boldsymbol{m}^T\boldsymbol{\varphi} \tag{3.11a}$$

$$\text{s.t.}\ \boldsymbol{\varphi} \geq \mathbf{0}_{2m+2n} \tag{3.11b}$$

where $\boldsymbol{\varphi} \in \Re^{2m+2n}$ represents the Lagrange multiplier vector; and $\boldsymbol{m} \in \Re^{2m+2n}$ and $\boldsymbol{Q} \in \Re^{(2m+2n)\times(2m+2n)}$ are shown in the form of

$$\boldsymbol{m} = \lambda_2\left(\widehat{\boldsymbol{A}} + \boldsymbol{I}_{(2m+2n)\times(2m+2n)}\right)\widehat{\boldsymbol{a}}\widehat{\boldsymbol{C}}^{-1} - \varepsilon\widehat{\boldsymbol{b}} - \widehat{\boldsymbol{d}} \tag{3.12}$$

$$\boldsymbol{Q} = \widehat{\boldsymbol{C}}^{-1}\left(\boldsymbol{I}_{(2m+2n)\times(2m+2n)} + \widehat{\boldsymbol{A}}\right)^{\mathrm{T}} \times \left(\widehat{\boldsymbol{A}} + \boldsymbol{I}_{(2m+2n)\times(2m+2n)}\right) + \widehat{\boldsymbol{G}}\widehat{\boldsymbol{b}}\widehat{\boldsymbol{b}}^{\mathrm{T}}\widehat{\boldsymbol{G}} \tag{3.13}$$

The constraints have been significantly simplified. Since Equation (3.11) is convex, the corresponding dual problem could be effectively solved using any available quadratic programming (QP) solution to achieve the global optimum of the newly proposed method. Let $\varphi^* \in \Re^{2m+2n}$ be the result of Equation (3.11); then the variables $\hat{\boldsymbol{z}}$ and δ can be expressed as:

$$\hat{\boldsymbol{z}} = \widehat{\boldsymbol{C}}^{-1}\left[\left(\widehat{\boldsymbol{A}} + \boldsymbol{I}_{(2m+2n)\times(2m+2n)}\right)^{\boldsymbol{T}}\boldsymbol{\varphi}^* - \boldsymbol{\lambda_2}\widehat{\boldsymbol{a}}\right] \tag{3.14}$$

$$\boldsymbol{\delta} = \widehat{\boldsymbol{b}}^{\boldsymbol{T}}\widehat{\boldsymbol{G}}\boldsymbol{\varphi}^* \tag{3.15}$$

Moreover, the coefficient **w** is able to express as:

$$\boldsymbol{w} = \boldsymbol{p} - \boldsymbol{q} = \hat{\boldsymbol{z}}(\mathbf{1}:\boldsymbol{n}) - \hat{\boldsymbol{z}}(\boldsymbol{n}+\mathbf{1}:\mathbf{2}\,\boldsymbol{n}) \tag{3.16}$$

As a result, the developed linear regression function is capable of expressing as:

$$\hat{f}(x) = (\boldsymbol{p} - \boldsymbol{q})^{\mathrm{T}}\boldsymbol{x} - \widehat{\boldsymbol{b}}^{\mathrm{T}}\widehat{\boldsymbol{G}}\boldsymbol{\varphi}^{*} \tag{3.17}$$

3.3. Kernel Based Nonlinear X-SVR

The applied empirical kernelisation could be shown as

$$\mathbf{x}_i = [x_{i,1}, x_{i,2}, ..., x_{i,n}]^T \mapsto \hat{\boldsymbol{\kappa}}(\mathbf{x}_i) = \begin{bmatrix} \boldsymbol{\Phi}(\mathbf{x}_1)^T \boldsymbol{\Phi}(\mathbf{x}_i) \\ \boldsymbol{\Phi}(\mathbf{x}_2)^T \boldsymbol{\Phi}(\mathbf{x}_i) \\ \vdots \\ \boldsymbol{\Phi}(\mathbf{x}_m)^T \boldsymbol{\Phi}(\mathbf{x}_i) \end{bmatrix} = \begin{bmatrix} \kappa(\mathbf{x}_1, \mathbf{x}_i) \\ \kappa(\mathbf{x}_2, \mathbf{x}_i) \\ \vdots \\ \kappa(\mathbf{x}_m, \mathbf{x}_i) \end{bmatrix}, \; for \; i = 1, 2, ..., m \tag{3.18}$$

where $\boldsymbol{\Phi}(\boldsymbol{x}_i)$ illustrates the implicit mapping function, which converts the i^{th} input data $\boldsymbol{x}_i \in \Re^n$ into Hilbert feature space or Euclidian space. The $\hat{\boldsymbol{\kappa}}(\boldsymbol{x}_i)$ illustrates the i^{th} component with the empirical degree m of the empirical feature vector (Scholkopf et al., 1999). The following figure illustrates the general structure of a nonlinear regression function.

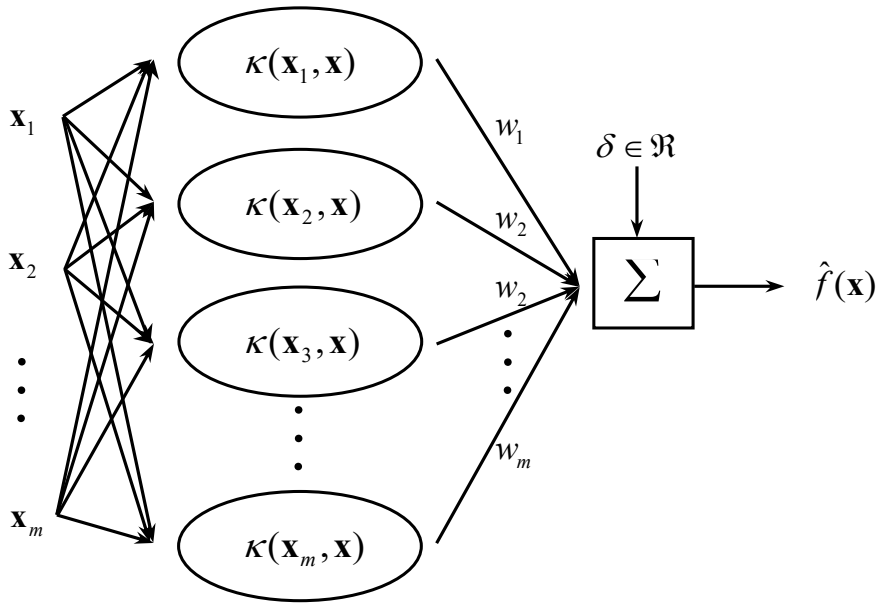

Figure 0.2 The general structure of a nonlinear regression function

Therefore, for a generalised training dataset $\boldsymbol{x}_{\text{train}}$ and a pre-selected kernel function $\boldsymbol{\kappa}(\cdot,\cdot)$, the initially selected training samples are transformed through the kernel matrix $\boldsymbol{\kappa}_{\text{train}} \in \Re^{m\times m}$, which can be expressed as

$$\boldsymbol{\kappa}_{train} = \begin{bmatrix} \kappa(\mathbf{x}_1,\mathbf{x}_1) & \kappa(\mathbf{x}_1,\mathbf{x}_2) & \cdots & \kappa(\mathbf{x}_1,\mathbf{x}_m) \\ \kappa(\mathbf{x}_2,\mathbf{x}_1) & \kappa(\mathbf{x}_2,\mathbf{x}_2) & \cdots & \kappa(\mathbf{x}_2,\mathbf{x}_m) \\ \vdots & \vdots & \ddots & \vdots \\ \kappa(\mathbf{x}_m,\mathbf{x}_1) & \kappa(\mathbf{x}_m,\mathbf{x}_2) & \cdots & \kappa(\mathbf{x}_m,\mathbf{x}_m) \end{bmatrix} \tag{3.19}$$

Furthermore, the equation could be written as

$$\min_{\boldsymbol{p}_\kappa,\boldsymbol{q}_\kappa,\delta,\boldsymbol{\xi},\boldsymbol{\xi}^*} : \frac{\lambda_1}{2}(\|\boldsymbol{p}_\kappa\|_2^2 + \|\boldsymbol{q}_\kappa\|_2^2) + \lambda_2 \boldsymbol{e}_m^T(\boldsymbol{p}_\kappa + \boldsymbol{q}_\kappa) + \frac{C}{2}\left(\boldsymbol{\xi}^T\boldsymbol{\xi} + \boldsymbol{\xi}^{*T}\boldsymbol{\xi}^*\right) \tag{3.20a}$$

$$s.t. \quad \begin{cases} \boldsymbol{\kappa}_{train}(\boldsymbol{p}_\kappa - \boldsymbol{q}_\kappa) - \delta\boldsymbol{e}_m - \boldsymbol{y}_{train} \le \varepsilon\boldsymbol{e}_m + \boldsymbol{\xi} \\ \boldsymbol{y}_{train} - \boldsymbol{\kappa}_{train}(\boldsymbol{p}_\kappa - \boldsymbol{q}_\kappa) + \delta\boldsymbol{e}_m \le \varepsilon\boldsymbol{e}_m + \boldsymbol{\xi}^* \\ \boldsymbol{p}_\kappa, \boldsymbol{q}_\kappa, \boldsymbol{\xi}, \boldsymbol{\xi}^* \ge \mathbf{0}_m \end{cases} \tag{3.20b}$$

where $\boldsymbol{p}_\kappa$, $\boldsymbol{q}_\kappa \in \Re^m$ are the nonlinear counterparts of $\mathbf{p}$ and $\mathbf{q}$ of the linear X-SVR. Then, the kernel-based X-SVR could be expressed as:

$$\min_{\hat{\boldsymbol{z}}_\kappa,\delta} : \frac{1}{2}\left(\hat{\boldsymbol{z}}_\kappa^{\mathrm{T}}\widehat{\boldsymbol{C}}_\kappa\hat{\boldsymbol{z}}_\kappa + \delta^2\right) + \lambda_2\hat{\boldsymbol{a}}_\kappa^{\mathrm{T}}\hat{\boldsymbol{z}}_\kappa \tag{3.21a}$$

$$\text{s.t.} \left(\widehat{\boldsymbol{A}}_\kappa + \boldsymbol{I}_{4m\times 4m}\right)\hat{\boldsymbol{z}}_\kappa + \left(\varepsilon\boldsymbol{I}_{4m\times 4m} + \delta\widehat{\boldsymbol{G}}_\kappa\right)\widehat{\boldsymbol{b}}_\kappa + \widehat{\boldsymbol{d}}_\kappa \ge \mathbf{0}_{4m} \tag{3.21b}$$

the matrices $\widehat{\boldsymbol{C}}_\kappa$, $\widehat{\boldsymbol{G}}_\kappa$, and $\widehat{\boldsymbol{A}}_\kappa \in \Re^{4m\times 4m}$ could be formulated as:

$$\widehat{\boldsymbol{C}}_\kappa = \begin{bmatrix} \lambda_1\boldsymbol{I}_{2m\times 2m} & \\ & C\boldsymbol{I}_{2m\times 2m} \end{bmatrix}, \widehat{\boldsymbol{G}}_\kappa = \begin{bmatrix} \mathbf{0}_{2m\times 2m} & \mathbf{0}_{2m\times m} & \mathbf{0}_{2m\times m} \\ \mathbf{0}_{m\times 2m} & \boldsymbol{I}_{m\times m} & \mathbf{0}_{m\times m} \\ \mathbf{0}_{m\times 2m} & \mathbf{0}_{m\times m} & -\boldsymbol{I}_{m\times m} \end{bmatrix}$$
$$, \widehat{\boldsymbol{A}}_\kappa = \begin{bmatrix} \mathbf{0}_{2m\times m} & \mathbf{0}_{2m\times m} & \mathbf{0}_{2m\times 2m} \\ -\boldsymbol{\kappa}_{train} & \boldsymbol{\kappa}_{train} & \mathbf{0}_{m\times 2m} \\ \boldsymbol{\kappa}_{train} & -\boldsymbol{\kappa}_{train} & \mathbf{0}_{m\times 2m} \end{bmatrix} \tag{3.22}$$

and the kernelised vectors $\widehat{\boldsymbol{a}}_\kappa$, $\widehat{\boldsymbol{b}}_\kappa$, $\widehat{\boldsymbol{d}}_\kappa$, and $\hat{\boldsymbol{z}}_\kappa \in \Re^{4m}$ are defined as:

$$\hat{\mathbf{a}}_{\kappa}=\begin{bmatrix}\mathbf{e}_{2m}\\ \mathbf{0}_{2m}\end{bmatrix},\ \hat{\mathbf{b}}_{\kappa}=\begin{bmatrix}\mathbf{0}_{2m}\\ \mathbf{e}_{2m}\end{bmatrix},\ \hat{\mathbf{d}}_{\kappa}=\begin{bmatrix}\mathbf{0}_{2m}\\ \mathbf{y}_{train}\\ -\mathbf{y}_{train}\end{bmatrix},\ \hat{\mathbf{z}}_{\kappa}=\begin{bmatrix}\mathbf{p}_{\kappa}\\ \mathbf{q}_{\kappa}\\ \boldsymbol{\xi}\\ \boldsymbol{\xi}^{*}\end{bmatrix} \tag{3.23}$$

The optimisation program described in Equation (3.21) could also be addressed by applying the Lagrange approach to its dual under the Karush-Kuhn-Tucker conditions. Consequently, the proposed method is able to be alternatively determined through its dual. That is,

$$\min_{\varphi_{\kappa}}:\frac{1}{2}\varphi_{\kappa}^{T}\boldsymbol{Q}_{\kappa}\varphi_{\kappa}-\boldsymbol{m}_{\kappa}^{T}\varphi_{\kappa} \tag{3.24a}$$

$$s.t.\ \varphi_{\kappa}\geq\mathbf{0}_{4m} \tag{3.24b}$$

where $\boldsymbol{Q}_{\kappa}\in\Re^{4m\times 4m}$ and $\boldsymbol{m}_{\kappa}\in\Re^{4m}$ are defined as:

$$\boldsymbol{Q}_{\kappa}=\left(\widehat{\boldsymbol{A}}_{\kappa}+\boldsymbol{I}_{4m\times 4m}\right)\widehat{\boldsymbol{C}}_{\kappa}^{-1}\left(\widehat{\boldsymbol{A}}_{\kappa}+\boldsymbol{I}_{4m\times 4m}\right)^{T}+\widehat{\boldsymbol{G}}_{\kappa}\widehat{\boldsymbol{b}}_{\kappa}\widehat{\boldsymbol{b}}_{\kappa}^{T}\widehat{\boldsymbol{G}}_{\kappa} \tag{3.25}$$

$$\boldsymbol{m}_{\kappa}=\lambda_{2}\left(\widehat{\boldsymbol{A}}_{\kappa}+\boldsymbol{I}_{4m\times 4m}\right)\widehat{\boldsymbol{C}}_{\kappa}^{-1}\widehat{\boldsymbol{a}}_{\kappa}-\varepsilon\widehat{\boldsymbol{b}}_{\kappa}-\widehat{\boldsymbol{d}}_{\kappa} \tag{3.26}$$

Let $\boldsymbol{\varphi}_{\kappa}^{*}\in\Re^{4m}$ be the solution of Equation (3.24), and the $\hat{\boldsymbol{z}}_{\kappa}$ and δ_{κ} are expressed as:

$$\hat{\boldsymbol{z}}_{\kappa}=\widehat{\boldsymbol{C}}_{\kappa}^{-1}\left[\left(\widehat{\boldsymbol{A}}_{\kappa}+\boldsymbol{I}_{4m\times 4m}\right)^{T}\varphi_{\kappa}^{*}-\lambda_{2}\widehat{\boldsymbol{a}}_{\kappa}\right] \tag{3.27}$$

$$\delta_{\kappa}=\widehat{\boldsymbol{b}}_{\kappa}^{T}\widehat{\boldsymbol{G}}_{\kappa}\varphi_{\kappa}^{*} \tag{3.28}$$

The coefficient $\boldsymbol{w}$ can be calculated as:

$$\boldsymbol{w}=\boldsymbol{p}_{\kappa}-\boldsymbol{q}_{\kappa}=\hat{\boldsymbol{z}}_{\kappa}(1:m)-\hat{\boldsymbol{z}}_{\kappa}(m+1:2\,m) \tag{3.29}$$

Then, the nonlinear regression function is determined by:

$$\hat{f}(\boldsymbol{x}) = (\boldsymbol{p}_\kappa - \boldsymbol{q}_\kappa)^{\mathrm{T}}\boldsymbol{\kappa}(\boldsymbol{x}) - \widehat{\boldsymbol{b}}_\kappa^{\mathrm{T}}\widehat{\boldsymbol{G}}_\kappa\boldsymbol{\varphi}_\kappa^* \tag{3.30}$$

The nonlinear counterpart of the X-SVR preprocesses the input samples by the kernelised method into the empirical space. Consequently, the convexity of the model is well retained since the X-SVR with the kernel is similar to the linear model with the manipulated input variables (Wang et al., 2019).

The series expansion of the Gegenbauer polynomial (Yin et al., 2016; Wu et al., 2006) is applied to the X-SVR as its kernelised model, and $P_{\hat{d}}^{\alpha}(x)$ satisfy the following relation:

$$P_0^{\alpha}(x) = 1 \tag{3.31a}$$

$$P_1^{\alpha}(x) = 2\alpha x \tag{3.31b}$$

$$P_{\hat{d}}^{\alpha}(x) = \frac{1}{\hat{d}}\left[2x\left(\hat{d} + \alpha - 1\right)P_{\hat{d}-1}^{\alpha}(x) - \left(\hat{d} + 2\alpha - 2\right)P_{\hat{d}-2}^{\alpha}(x)\right] \ (\hat{d} = 2,3,4,\dots) \tag{3.31c}$$

where $\hat{d} \in \mathbb{Z}_0^+ := \{x \in \mathbb{Z} | x \geq 0\}$ denotes the polynomial sequence, and α denotes the parameter with a positive value. The Gegenbauer weight function $\rho^{\alpha}(x)$ is orthogonal to the Gegenbauer polynomials for a given α over $x \in [-1,1]$, which can be described as

$$\int_{-1}^{1} \rho^{\alpha}(x)P_{\hat{\imath}}^{\alpha}(x)P_{\hat{\jmath}}^{\alpha}(x)dx = h_{\hat{\imath}}^{\alpha}\delta_{\hat{\imath}\hat{\jmath}} \ \ (\hat{\imath},\hat{\jmath} = 0,1,\dots,\hat{d}) \tag{3.32}$$

where $\rho^{\alpha}(x)$, $h_{\hat{\imath}}^{\alpha}$ and $\delta_{\hat{\imath}\hat{\jmath}}$ can be formulated as

$$\rho^{\alpha}(x) = (1 - x^2)^{\alpha - \frac{1}{2}} \tag{3.33}$$

$$h_{\hat{\imath}}^{\alpha} = \frac{\pi 2^{1-2\alpha}\Gamma(\hat{\imath}+2\alpha)}{\hat{\imath}!\,(\hat{\imath}+\alpha)\Gamma^2(\alpha)} \tag{3.34}$$

$$\delta_{\hat{\imath}\hat{\jmath}} = \begin{cases} 0 & (\hat{\imath} \neq \hat{\jmath}) \\ 1 & (\hat{\imath} = \hat{\jmath}) \end{cases} \tag{3.35}$$

In Equation (3.34), $\Gamma(\cdot)$ denotes the Gamma function. By employing the strategy utilised for characterising the generalised vector inputs of the Chebyshev polynomial (Ye et al., 2006; Ozer et al., 2011; Moghaddam and Hamidzadeh, 2016), the generalised Gegenbauer polynomials can be demonstrated as

$$P_0^{\alpha}(\boldsymbol{x}) = 1 \tag{3.36a}$$

$$P_1^{\alpha}(\boldsymbol{x}) = 2\alpha\boldsymbol{x} \tag{3.36b}$$

$$P_{\hat{d}}^{\alpha}(\boldsymbol{x}) = \frac{1}{\hat{d}}\left[2\boldsymbol{x}^T\left(\hat{d}+\alpha-1\right)P_{\hat{d}-1}^{\alpha}(\boldsymbol{x}) - \left(\hat{d}+2\alpha-2\right)P_{\hat{d}-2}^{\alpha}(\boldsymbol{x})\right] \ (\hat{d} = 2,3,4,\dots) \tag{3.36c}$$

where $\boldsymbol{x} \in \Re^n$ illustrates the column vector. Gaussian kernel function exhibits more capability of capturing the local information when compared to the initially applied square root function (Ozer et al., 2011). The $\hat{d}$th order Gegenbauer kernel (GGK) function $\kappa_{\mathrm{GGK}}^{\hat{d}}(\boldsymbol{x}_i, \boldsymbol{x}_j)$ is shown as

$$\kappa_{GGK}^{\hat{d}}(\boldsymbol{x}_i, \boldsymbol{x}_j) = \frac{\sum_{\hat{k}=0}^{\hat{d}} P_{\hat{k}}^{\alpha}(\boldsymbol{x}_i)^T P_{\hat{k}}^{\alpha}(\boldsymbol{x}_j)}{exp\left(\left\|\boldsymbol{x}_i - \boldsymbol{x}_j\right\|_2^2 \gamma\right)} \tag{3.37}$$

3.4. Selection of Model Parameters

There are seven hyperparameters in the X-SVR method, which are two positive kernel scale variables γ and α, the polynomial order $\hat{d}$, the insensitive tube width ε, the penalty parameter C, and two regularisation parameters λ_1 and λ_2 (Wang et al., 2019)

Generally, to assure the generalised capability of the high predicting regression function, the *k*-fold cross-validation over the training samples method is employed (Schölkopf et al., 2002). This method is also applied in this regression method to eliminate overfitting. $Err_{5\mathrm{CV}}$ is the 5-fold CV error, which is applied to representing the measurement of the training error, and it can be shown as

$$Err_{5CV} = \frac{1}{5}\sum_{\vartheta=1}^{5} err_{\vartheta} \tag{3.38}$$

where err_{ϑ} is the mean squared error. More specifically, we have

$$err_{\vartheta} = \frac{1}{m_{\vartheta}}\sum_{\varpi=1}^{m_{\vartheta}}\left[\boldsymbol{y}_{\vartheta,\varpi} - \hat{f}_{\vartheta}(\boldsymbol{x}_{\vartheta,\varpi})\right]^2 \quad (\vartheta = 1,2,\ldots,5) \tag{3.39}$$

where $\boldsymbol{y}_{\vartheta,\varpi}$ is the ϖth component of $\boldsymbol{y}_{\vartheta}$, $\boldsymbol{x}_{\vartheta} \in \Re^{m_{\vartheta}\times n}$ holds the training samples of the ϑth fold, $\boldsymbol{x}_{\vartheta,\varpi} \in \Re^{n}$ represents the ϖth component of $\boldsymbol{x}_{\vartheta}$, and $\hat{f}_{\vartheta}(\cdot)$ describes the model prediction.

The Bayesian optimisation (BO) algorithm was used in this research to quantify the probabilistic approximation of the scalar objective function $f(x)$ for a point x by applying Gaussian process (GP) and maintaining a posterior distribution function Q,

and then the next point was determined by optimising the expected improvement (EI), based on the current best result or the GP upper confidence bound (Snoek et al., 2012).

Instead of employing the traditional grid search approach, the Bayesian optimisation algorithm can be used efficiently to select the hyperparameters of the proposed X-SVR method (Feng et al., 2019). It should be noted that the expected improvement in the MATLAB function was defined as follows:

$$EI(x, Q) = E_Q[max(0, \mu_Q(x_{best}) - f(x))] \quad (3.40)$$

where, EI is expected improvement, $\mu_Q(x_{best})$ denotes the lowest value of the posterior mean, and x_{best} indicates the location of the lowest posterior mean. Furthermore, fewer iterations are required to establish the minimum objective function when applying all the previously evaluated and available information. Thus, this study integrated the BO algorithm with the proposed method for intelligently picking the learning parameters.

3.5. Summary

This chapter explains the functions of the advanced ML method, and the X-SVR method was applied to predict the unloading/reloading modulus of underlying geomaterial according to the drum's acceleration responses. The extensive generated datasets were used for training and testing the X-SVR machine learning algorithm to validate the reliability of the correlated model.

In this research, linear X-SVR, and kernel-based nonlinear X-SVR were adopted for real-time prediction of layered soil stiffness, and this chapter introduced the main aspects of the proposed approach. The proposed X-SVR could accurately predict both

the single and double layered soil stiffness, both training and predicting unloading-reloading modulus correlated well with adopted parameters in the 3D finite element model, which are detailed explained in Chapters 5 and 6.

Chapter 4

Numerical Assessment of Impacts of Vibrating Roller Characteristics on Acceleration Response of Drum Used for Intelligent Compaction

4.1. General

IC is an appealing technology for efficient and optimised ground compaction, which is proven capable of providing a detailed control system for the compaction process with real-time feedback and adjustment on the full compaction area. Although roller manufacturers offer typically recommended settings for rollers in various soils, there are still some areas needing further improvement, particularly on the selection of vibration amplitude and frequency of the drum in soils experiencing significant nonlinearity and plasticity during compaction.

In this chapter, the interaction between the road subgrade and the vibrating roller is simulated, which is using the 3D FEM to capture the dynamic responses of the soil and the roller. The developed method is capable of simulating the nonlinear behaviour of soil under dynamic loading. The dynamic load of the roller is explicitly applied to the simulated cylindrical roller drum. Besides, the impacts of the amplitude and frequency on the level of subgrade compaction are discussed according to the detailed numerical analysis. The adopted constitutive model allows the assessment of the progressive settlement of ground subjected to cyclic loading.

The results based on the numerical modelling reveal that the roller vibration characteristics can impact the influence depth, the level of soil compaction, and its variations with depth. The results of this study can be utilised as potential guidance by practicing engineers and construction teams on selecting the best roller vibration frequency and amplitude choice to achieve high-quality compaction.

4.2. Introduction

CCC is an emerging and appealing technology because it has provided a continuous assessment of soil stiffness since the technology first began over 40 years ago. The mechanistic measurements derived from the IC roller allow practicing engineers and construction teams to evaluate the quality of the compacted ground; hence, a thorough understanding of qualitative control of the soil and drum behaviour is of prime importance.

Soil stiffness is strongly correlated to loading conditions or strain levels, and there is an increasing emphasis on the investigation of soil stiffness in the field based on the roller response (Herrera et al., 2018). Therefore, the majority of experimental research

was carried out to examine the correlation between soil stiffness and roller characteristics, for example, the drum frequency and amplitude (Kenneally et al., 2015; Herrera et al., 2018; Anderegg and Kaufmann, 2004). However, referring to some recent studies, the interaction between compacted soil and drum reveals a notable nonlinearity (Kenneally et al., 2015; Herrera et al., 2018; Mooney and Rinehart, 2009).

The measured soil modulus reflects on the composite response of layered strata (Van Susante and Mooney, 2008); further analysis would be required to obtain the characteristics of each newly compacted layer. The assumption of added masses for the simulation of the soil has been generally adopted in many lumped-parameter models; thus, those models are unable to explicitly portray the decoupling behaviour of soil-drum system because of the overly simplified nature of simulations of inertial and dissipative properties for the soil modelling (Kenneally et al., 2015). Thus, a discretised computational numerical model can be recommended to capture the complex soil-drum interaction behaviour while simulating the soil's nonlinear behaviour under cyclic loading.

Developing the representative model to evaluate the sophisticated interaction between the layered geomaterial and the vibratory drum is necessary. Thus, in this chapter, a 3D FEM is utilised to examine the dynamic responses of the soil-drum system. The key motivation for the chapter is to assess the feasibility of the numerical model and reveal the impacts of the roller vibration characteristics on the soil response via the numerical simulation. While many previous studies had investigated the roller response when the full compaction state in the soil was reached, in this study, the roller response when the soil is being compacted from a weak state to a stronger state is simulated.

Moreover, the cyclic load is explicitly applied on the simulated cylindrical roller drum; and the roller properties are varied in terms of excitation frequency, amplitude and weight to assess the impacts on the level of subgrade compaction. These simulation results can be indicators for practicing engineers and construction teams to select optimised roller parameters and obtain a better understanding of intelligent compaction readings to achieve high-quality soil compaction. It should be noted that detailed field experiments would help to further assess the suitability of the established numerical model for the interpretation of intelligent compaction measurements.

4.3. Development of a Finite Element Model for Simulating Soil-Drum Interaction

4.3.1. Roller Characteristics

The dynamic response of the vibratory roller on the compacted underlying soil was evaluated using PLAXIS 3D in this study. The 3D FEM was carried out to predict the influences of soil and drum behaviour and the way in which the soil characteristics impacted the drum response. A typical vibrating rigid, smooth drum sitting on a uniform soil deposit was modelled using the continuum-based approach with appropriate material properties and geometries assigned to each component. This chapter modelled a typical rigid smooth drum with a length and radius of 2.1 m and 0.75 m, respectively.

Loading conditions for a given vibratory roller are defined by the frequency and amplitude of the loading, which depends on the frequency of its rotation, eccentricity and eccentric mass, and can impact the productivity of the roller significantly (Lavin, 2003). Referring to Figure 4.1, a single drum roller typically adopted for soil

compaction, together with counter-rotating eccentric masses to provide directional eccentric force amplitude. The resultant eccentric mass moment ($m_0 e_0$) was set between 1 to 5 kg. m. In addition, the employed excitation frequency ranged from 25 to 35 Hz. Details of the roller properties are summarised in Table 3.1. The vibratory roller had a total weight of 7,000 kg, which was used as the total weight of the simulated drum in this study.

The soil compaction via vibratory roller is induced by the combination of static forces (weights of frame and drum) as well as dynamic forces (the counter-rotating eccentric masses resulted in centrifugal force). The MDOF vibration system with various components, including the drum, frame, back tire and cabin, can represent the entire system more accurately. However, for the sake of simplicity and practicality, the SDOF system for the drum is often implemented which can capture the most significant impact force induced by the vibrating drum (Herrera et al., 2018; Bhandari et al., 2022; Xu et al., 2022a). Additionally, low-stiffness rubbers separate the compactor frame from the drum, leading to the effects of the dynamic frame being insignificant, resulting in frame dynamic effects often being neglected in the analysis (Xu et al., 2022a). Figure 4.1 exhibits a free body diagram of SDOF lumped mass model of vibratory roller compactor.

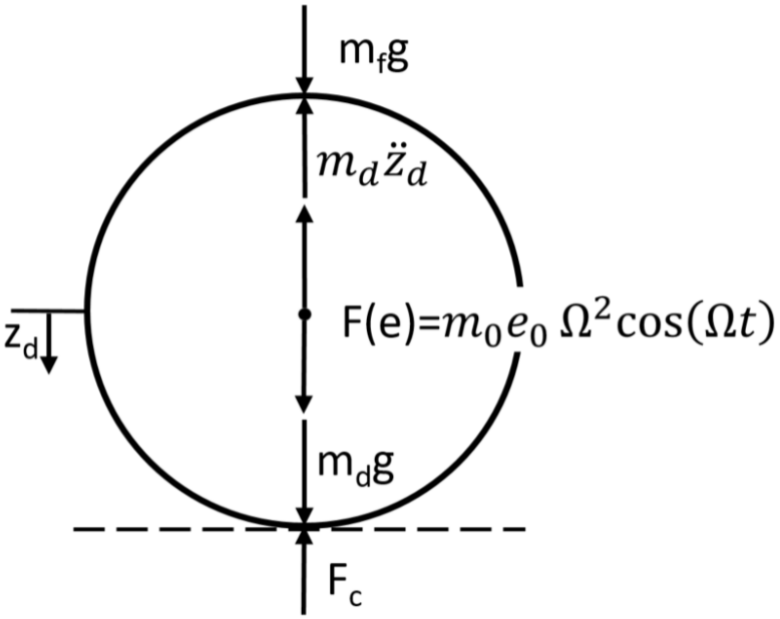

Figure 0.1 A free body diagram of 1-DOF lumped mass model of vibratory roller compactor

The externally applied load on the soil could lead to the dissipation of excess pore pressures, resulting in soil consolidation (Ho et al., 2018). In addition, a more complex soil-drum modelling is required to acquire the effective compaction force. However, the roller behaviour was simplified to validate the soil response adopting the HS-Small model utilised in this chapter. The full contact conditions between the soil and drum were continuously maintained.

$$F_C = m_0 e_0 \, \Omega^2 \cos(\Omega t + \varphi) + m_d g + m_f g - m_d \ddot{z}_d - \, m_f \ddot{z}_f \tag{4.1}$$

where $\ddot{z}_d$ is the acceleration of the drum, and F_C, $m_0 e_0$,and Ω, are the soil reaction force, the eccentric mass moment, and the frequency of the operating roller, respectively; $\ddot{z}_f$ is the acceleration of the vibratory roller frame, and it was neglected in this study.

Table 0.1 Operational parameters of vibratory roller

Parameter	**Value**	**Unit**
Length of drum	2.1	*m*
Diameter of drum	1.5	*m*
Mass of frame	2534	*kg*
Mass of drum	4466	*kg*
Eccentric mass moment inducing vibration	1.0 – 5.0	*kg m*
Vibration excitation frequency	25 – 35	*Hz*

Note: Data are taken from Kenneally et al. (2015).

4.3.2. Modelling of the Single Layered Soil Strata

Consideration of soil nonlinearity when simulating soil-structure interaction is of critical importance (Brinkgreve et al., 2010b; Han et al., 2016). Indeed, simple elastic or viscoelastic constitutive models are unable to simulate the soil deformation and forces transferred from the soil to the roller accurately, impacting its acceleration response (Herrera et al., 2018; Zhang and Kimura, 2002; Fatahi et al., 2020). Thus, it is crucial to adopt a suitable constitutive model for capturing the nonlinear stress-strain response of the underlying soil properties subjected to cyclic loading, specifically by capturing damping with shear strain and variations of soil stiffness and allowing the prediction of permanent soil deformations during compaction (Brinkgreve et al., 2010b; Sharma and Kumar, 2018; Nazarian et al., 2020).

In this chapter, the soil response subjected to cyclic loading was evaluated by applying the HS-Small model developed by Benz et al. (2009). The proposed model could capture stiffness degradation as well as the stress-strain dependant stiffness. The

small-stain stiffness is a fundamental characteristic of geomaterials, including rocks, gravels, sands, silts and clays under different loading conditions (Burland, 1989; Kuwano, 2018).

The HS-Small model was developed based on the hardening soil model (Schanz et al., 2019), and was then extended by two extra input parameters small-strain shear stiffness (G_0) and a shear strain ($\gamma_{0.7}$), and each input parameter in the HS-Small model has a clear geotechnical meaning (Brinkgreve et al., 2007). According to Benz et al. (2009), the model can simulate the modulus decay and hysteretic damping of the soils at the small strain range. HS-Small model needs six stiffness related parameters defined at a reference pressure of p^{ref} ($i.e.\,100$ kPa in this study), i.e. E_{50}^{ref} and $E_{\mathrm{oed}}^{\mathrm{ref}}$, which are the secant and tangent stiffnesses, respectively; $E_{\mathrm{ur}}^{\mathrm{ref}}$ representing the unloading/reloading stiffness; and v_{ur} indicating the Poisson's ratio for unloading/reloading cycles.

Two yield surfaces were applied in the HS-Small model, namely cap yield surface and shear hardening yield surface. The associated flow rule was utilised in the cap yield surface, considering plastic volumetric strains. By contrast, a non-associated flow rule was applied in the shear hardening yield surface, which functions as the deviatoric plastic strains, and it also satisfied Mohr-Coulomb failure criterion. The failure criterion with three measurable strength parameters: cohesion (c_{ref}), angle of dilatancy (ψ) and angle of friction (φ) were employed. Moreover, two empirical inputs, i.e. failure ratio (R_{f}) and power for the stress-level dependency of stiffness (m) are required in the model.

The model is appropriate for simulating granular materials (Huynh et al., 2022; Costigliola et al., 2022) and clays (Hejazi et al., 2008; Gong et al., 2020) under nonlinear behaviour at small strain levels, and these input parameters can be easily determined from triaxial drained test results, or correlated to the results of the Cone Penetration Test (CPT) and the Seismic Dilatometer Marchetti Test (SDMT) (Kawa et al., 2021; Schanz et al., 2019). Therefore, the model has gained popularity for its application in geotechnical practice as all input parameters have a clear geotechnical relevance (Schanz et al., 2019; Kawa et al., 2021). The details of the HS-Small model are assessed in Chapter 2, Section 2.5.3.

The properties of sandy soil reported by Brinkgreve et al. (2016) were applied and summarised in Table 4.2. Having calculated the model based on the above-mentioned data, the average shear wave velocity (s-wave) and compressional wave velocity (p-wave) at $p = p^{ref}$ = 100 kPa were 268.2 m/s and 438.0 m/s, respectively.

Table 0.2 Soil parameters based on hardening soil model with small-strain stiffness

Parameter	**Symbol**	**Value**	**Unit**
Saturated unit weight	γ_{sat}	20	kN/m^3
Unsaturated unit weight	γ_{unsat}	17	kN/m^3
Unloading/reloading stiffness	E_{ur}^{ref}	150000	kN/m^2
Primary oedometer stiffness	E_{oed}^{ref}	50000	kN/m^2
Triaxial compression stiffness	E_{50}^{ref}	50000	kN/m^2
Rate of stress-dependency	M	0.5	-
Cohesion	C	0	kN/m^2
Poisson's ratio	υ_{ur}	0.2	-
Dilatancy angle	Ψ	0	°
Friction angle	Φ	31	°
Shear strain at 0.7 G_0	$\gamma_{0.7}$	$1.0 \cdot 10^{-4}$	-
Small strain stiffness	G_0^{ref}	$1.2 \cdot 10^5$	kN/m^2
Over-consolidation ratio	OCR	1.0	-

Note: Data are taken from Brinkgreve et al. (2016).

To validate the reliability of the FEM prediction and assess the suitability of the adopted soil constitutive model, the developed numerical simulations with the HS-Small model results were compared with the data reported by Wu (1990) for triaxial tests conducted on Karlsruhe sand for different relative densities at 100 kN/m^2 cell pressure, as shown in Figure 4.2. It has been shown that the predicted results, which accept correlations for the model parameters as provided by Brinkgreve et al. (2010b), are in a respectable agreement with the experimental data. The model can reasonably

predict the deviatoric stresses and volumetric strains of both loose and dense sandy soils.

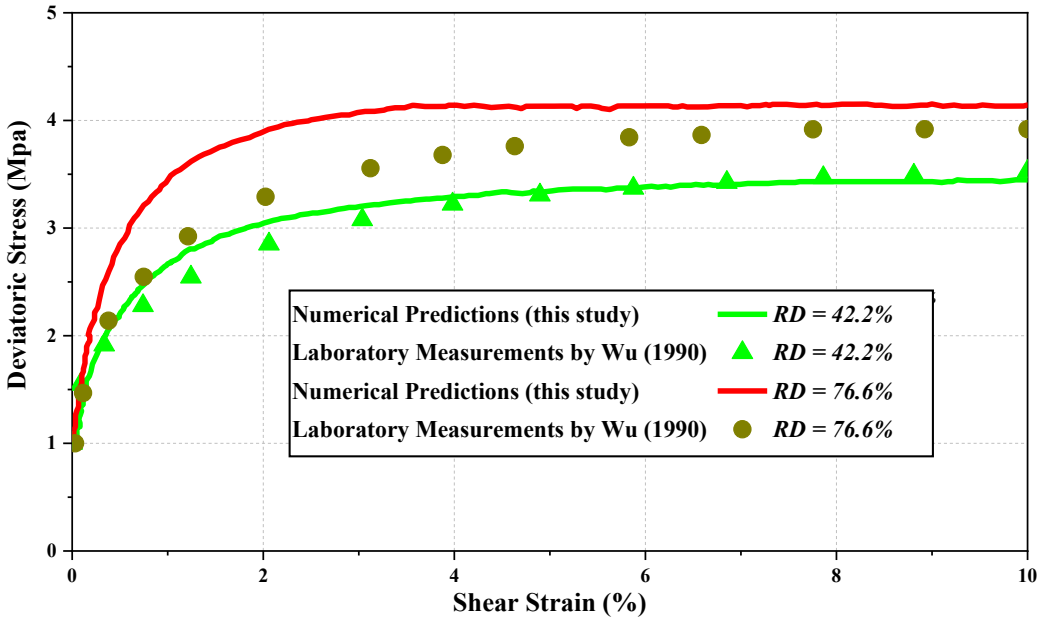

(a)

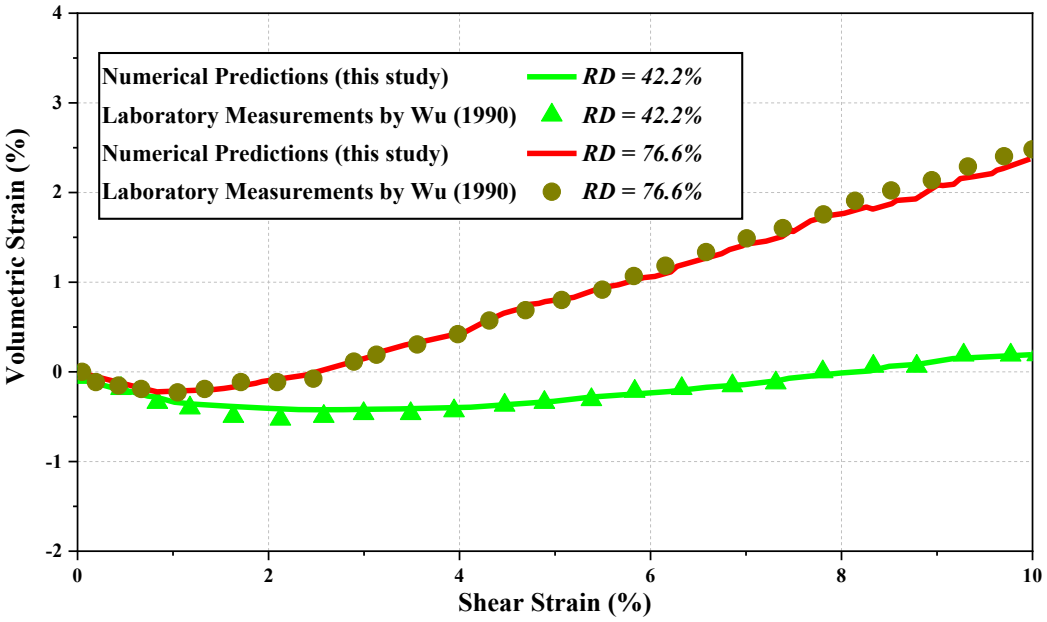

(b)

Figure 4.2 Comparison between the drained triaxial test results on Karlsruhe sand and HS-Small model predictions and those obtained based on proposed correlations for different relative densities by Brinkgreve et al. (2010b)

4.3.3. Finite Element Model

To characterise the soil-roller interaction, a model consisting of vibratory drum resting on the soil deposit was modelled in 3D FE software, PLAXIS 3D (2017). Roller parameters reported in Table 4.1 were as-signed to the drum simulated in this study. The simulated drum-soil system is portrayed in Figure 4.3. The roller was modelled as a rigid body consisting of a 2.1 m length and 1.5 m diameter drum. The vibration excitation force ($F_e = F_{ev}\cos(\Omega t)$) induced by an eccentric mass configuration, which rotates around the drum's longitudinal axis, was applied as a vertically vibrating harmonic load to the roller. It should be noted that due to the counter-rotating eccentric masses, the horizontal forces were cancelled out, and therefore they were neglected in this chapter similar to what was adopted in other studies (Van Susante and Mooney, 2008).

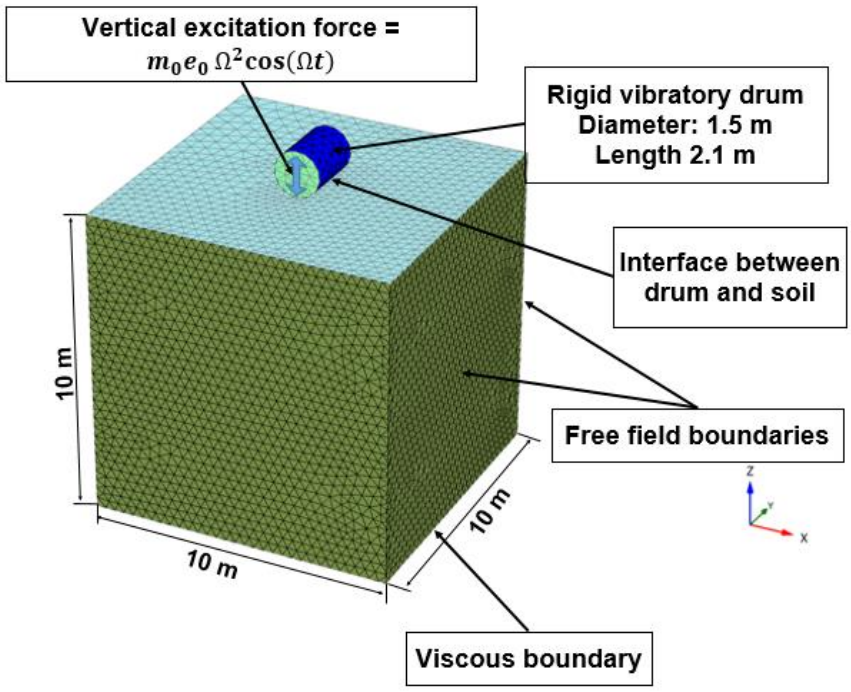

Figure 0.3 Adopted three-dimensional numerical model capturing interaction between vibratory roller and the ground

A soil deposit was modelled with a width of 10 m, a length of 10 m and a depth of 10 m. It should be noted that the full response depth associated with the vibratory roller was estimated to be from 0.6 to 1.0 m (Adam, 2007). Thus, 10 m was deemed sufficient for modelling purposes. Consideration of interface elements has a notable impact on the numerical predictions while the soil is interacting with structures (Fatahi et al., 2014; Fatahi et al., 2018).

The 3D model was utilised to conduct an implicit nonlinear time-integration with a time step of 2.5×10^{-4} s. Indeed, there were three different loading stages adopted in this numerical modelling to assess the soil response to the drum vibration during the compaction process. The first phase was application of gravity loading only; the second stage was the dynamic loading phase, where the vibration load was applied on the drum followed by the third stage, which was a static condition while the roller was removed to establish the permanent deformation of the soil after completion of the soil compaction. The results of the conducted numerical modelling and parametric studies are discussed as follows.

4.3.4. Roller-Soil Interface Modelling and Boundary Conditions of the Single Layered Soil Strata

Appropriate interfaces are required to simulate the soil-drum interaction capturing stress transfer via interacting surfaces. In this study, 12-node triangular interface elements with 6-point Gaussian integration were utilised to capture any possible soil deflection and drum vibratory displacement while the soil was interacting with the drum.

The behaviour of the interface was evaluated by implementing the linear elastic-perfectly plastic constitutive model (Fatahi et al., 2020). The interface strength reduction factor R_{inter} was adopted via the following equations:

$$c_i = c_s R_{inter} \tag{4.2}$$

$$tan\varphi_i = tan\varphi_s R_{inter} \leq tan\varphi_s \tag{4.3}$$

$$\sigma_{t,i} = \sigma_{t,s} R_{inter} \tag{4.4}$$

$$\psi_i = 0^{\circ}\ for\ R_{inter} < 1;\ otherwise\ \psi_i = \psi_s \tag{4.5}$$

$$G_i = G_{soil} R_{inter}^2 \leq G_{soil} \tag{4.6}$$

where i and s refer to the interface and soil, respectively; c_{s} and c_{i} are the cohesions of the soil and interface, respectively; σ_{t} is the tensile strength of the soil; φ_{s} and φ_{i} are the friction angles of the soil and interface, respectively; and ψ_{i}, ψ_{s}, G_{i} and G_{soil} are the dilation angles of interface and soil, and shear moduli of interface and soil, respectively. Similar to previous studies (Wehnert and Vermeer, 2004; Aghayarzadeh et al., 2020; Xu et al., 2022a), R_{inter} = 1 was adopted, while the zero-tension limit was introduced allowing separation of roller drum from the soil surface without any resistance (Brinkgreve et al., 2016).

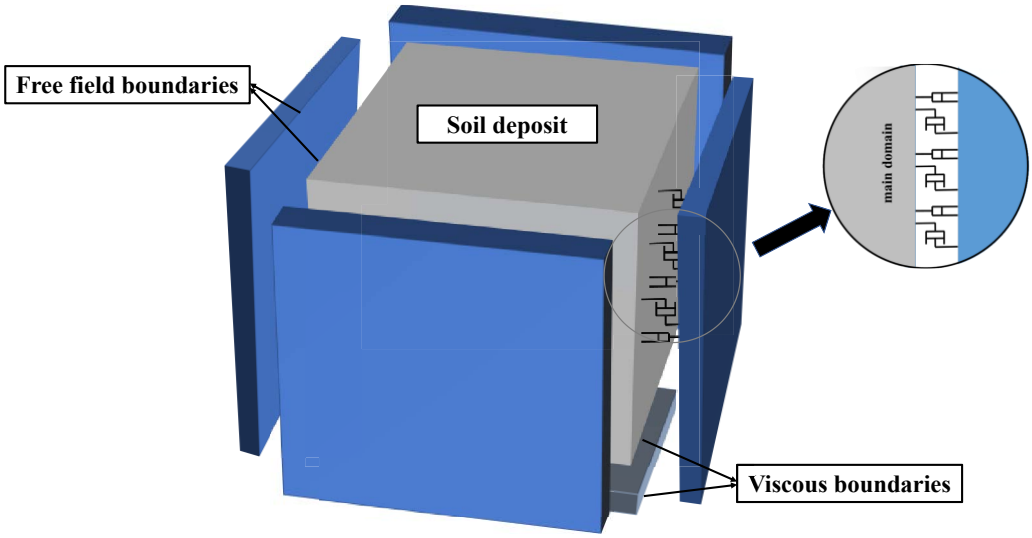

Figure 4.4 Adopted numerical model, designed for the unbound soil with free-field and viscous boundaries conditions

Moreover, during the static and dynamic studies, two separate sets of boundary conditions were employed. While considering the gravity loading in the static case, the nodes of the bottom boundary were completely constrained in all directions. In contrast, the lateral displacements on the side boundaries of the model were avoided. Referring to Figure 4.4, during the dynamic analysis, while the roller was vibrating, free-field boundaries coupled with independent viscous dashpots were employed to transfer the free-field motion from four side boundaries. Indeed, through the use of resistant tractions in both the tangential and normal directions, the proposed boundary conditions could prevent the wave energy reflecting back into the soil (Fatahi et al., 2020).

Furthermore, a viscous boundary (non-reflecting boundary condition) with the dampers was used at the bottom boundary during dynamic analysis to absorb the crossing waves without rebounding to reduce wave reflection from the boundaries as suggested by Kenneally et al. (2015) and Herrera et al. (2018) corresponding to the deep soil deposits in situ. The adopted shear and normal tractions on the boundaries

to cancel the reflecting waves out were defined as follows (Lysmer and Kuhlemeyer, 1969):

$$t_s = -\rho V_s C_s \tag{4.7}$$

$$t_n = -\rho V_n C_p \tag{4.8}$$

where V_{s} and V_{n} are the shear and normal components of the velocity, respectively; ρ is the density of the medium; t_{s} and t_{n} are the tractions in the shear and normal directions, respectively; and C_{s} and C_{p} are the S- and P-wave velocities, respectively. To ensure minimal boundary effects, a block of soil that was 10 m in length, 10 m in width (more than five times larger than the roller length), and 10 m deep (more than six times larger than the roller diameter) was simulated.

4.4. Results and Discussion

To better investigate the soil response due to vibratory roller behaviour, impacts of roller frequency, amplitude and weight of roller were assessed in this chapter. In the adopted numerical model, the excitation force caused by the rotating eccentric masses was applied to the rigid drum, while different vibration frequencies as well as various eccentric mass moments and different weight of roller $[(m_d + m_f)g]$ were considered to evaluate the drum response.

4.4.1. Effects of Vibration Frequency

Vibratory roller frequency as a fundamental parameter in the dynamic system has a crucial impact on roller compaction. To scrutinise the effects of the vibratory drum, varied frequencies while keeping the eccentric mass moment $m_0 e_0$ = 2 kg. m and weight of drum and frame equal to 7,000 kg constant, were considered. The impact of

roller excitation frequency on the soil response was studied by varying frequency from 26 Hz to 34 Hz. It could be noted that the first natural frequency of the soil deposit was estimated to be 110 Hz - 183Hz (i.e. $V_p/(4H)$), corresponding to roller influence depth of 0.6 – 1.0 m.

Figure 4.5 presents the time history of soil displacement in conjunction with different vibration frequencies of the roller. Referring to this figure, the soil gradually settled due to roller vibration, where f = 34 Hz exhibited the highest degree of soil compaction for the adopted sandy soil. The observations, based on the conducted numerical modelling in this study, exhibit when the vibration frequency is close or equal to the natural frequency of the soil, the vibratory roller can achieve the optimum compaction, and the observed results are consistent with the results reported by other researchers (Masad et al., 2016; Wersäll and Larsson, 2016; Li and Hu, 2018).

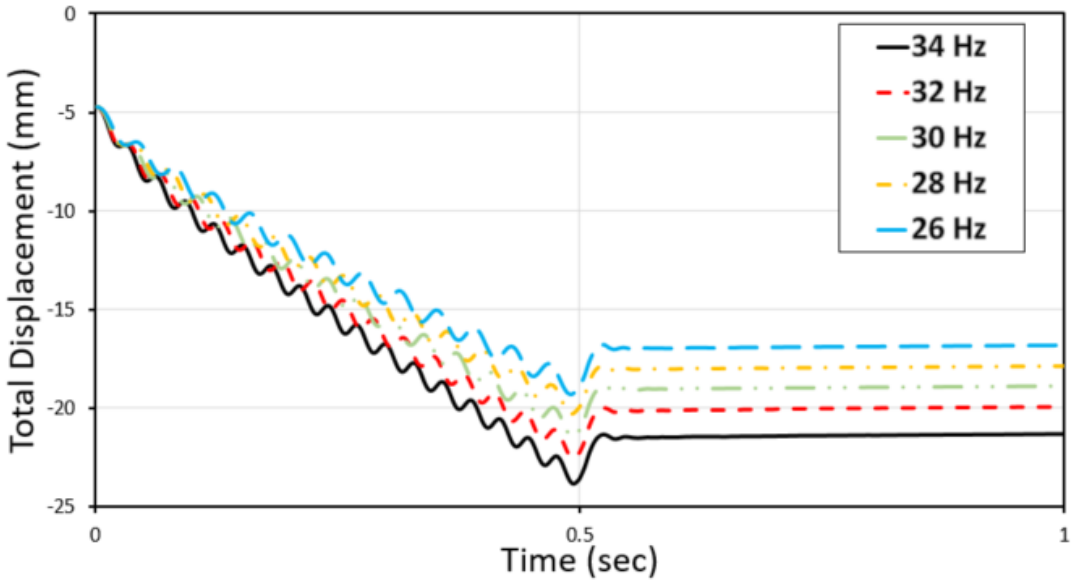

Figure 0.5 Settlement (permanent displacement) of soil due to harmonic dynamic loading

Regarding the operation frequency f = 34 Hz, the initial soil settlement (i.e. 4.8 mm) was observed before vibration just because of the self-weight of the roller.

Furthermore, the maximum vertical settlement of the soil in the dynamic phase is 23.8 mm and reached residual settlement of 21.5 mm when the roller was removed. As expected, the initial soil settlement (i.e. 4.8 mm) was larger than the recoverable soil settlement (i.e. 2.3 mm) since the initial loading stages comprised of both elastic and plastic components, whereas the unloading stage comprised of only elastic component. Figure 4.5 presents the soil settlement accumulates as a result of plastic deformation during each loading cycle as the dynamic time increased. The irreversible deformation occurred in the soil indicates the gradual compaction of the soil and incremental increases in the yield stress in the soil.

Indeed, the roller vibration frequency closest to the first mode natural frequency of the ground (i.e. roller vibration frequency of 34 Hz) resulted in more ground displacement and soil compaction as expected (Pietzsch and Poppy, 1992). Therefore, as the excitation frequency acquired a lower value than the natural frequency of the soil, the accumulated soil settlement was reduced, as evident in Figure 4.5.

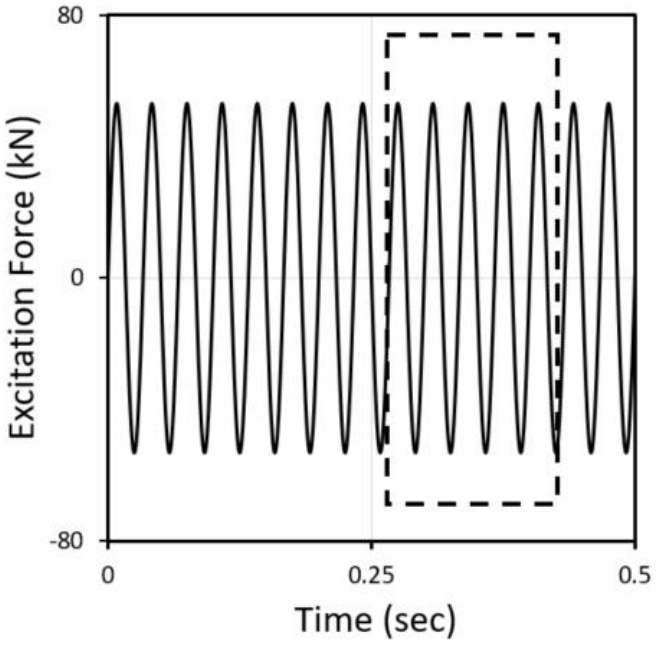

(a)

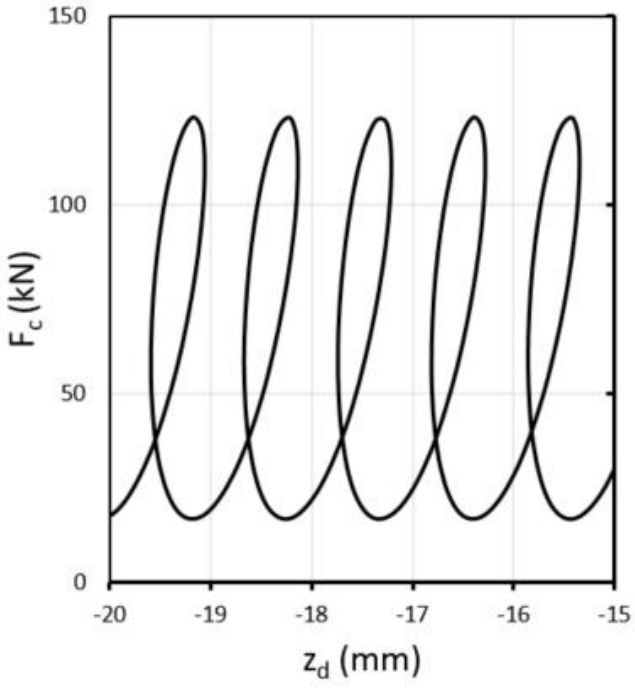

(b)

Figure 0.6 (a) A sample of applied excitation force vs time for frequency = 30 Hz and (b) soil reaction force vs soil surface displacement

Figures 4.6(a) and 4.6(b) present the time history of excitation force with a frequency of 30 Hz and the corresponding soil reaction force – cyclic soil surface displacement relationship. The energy lost in the soil due to soil damping and plastic deformations are evident in Figure 4.4(b).

4.4.2. Effects of Amplitude

The nominal amplitude of the vibratory drum displacement is directly impacted by the eccentric mass (Pietzsch and Poppy, 1992). To consider the impacts of the excitation force amplitude of the roller on the soil and drum interaction and therefore the compaction process, several different magnitudes of eccentric mass moments while keeping the vibration frequency constant equal to f = 30 Hz were adopted in this study. A number of constant eccentric mass moments varying from 1 kg.m to 4 kg.m were investigated to provide directional eccentric force amplitude.

In general, a lower eccentric mass moment is capable of providing smaller excitation force amplitude, and it is usually used for proof rolling and finishing passes to avoid over-compaction; conversely, a higher eccentric mass moment is utilised in the early stage of compaction (Kenneally et al., 2015). Figure 4.5(a) illustrates the evolution of the accumulation of soil displacement with time as a function of varying eccentric mass moment. It should be noted that in the range of applied eccentric mass moment, the full contact condition between the soil and drum was continuously maintained.

For a given vibration frequency of f = 30 Hz and soil parameters reported in Table 4.2, the soil settlement increased with eccentric mass moment with the maximum observed when $m_0 e_0$ = 4 kg.m, as shown in Figure 4.7(a). The results show that an increase in the eccentric mass moment led to an increase in the compacted soil

displacement, which is consistent with the observations reported by Masad et al. (2016).

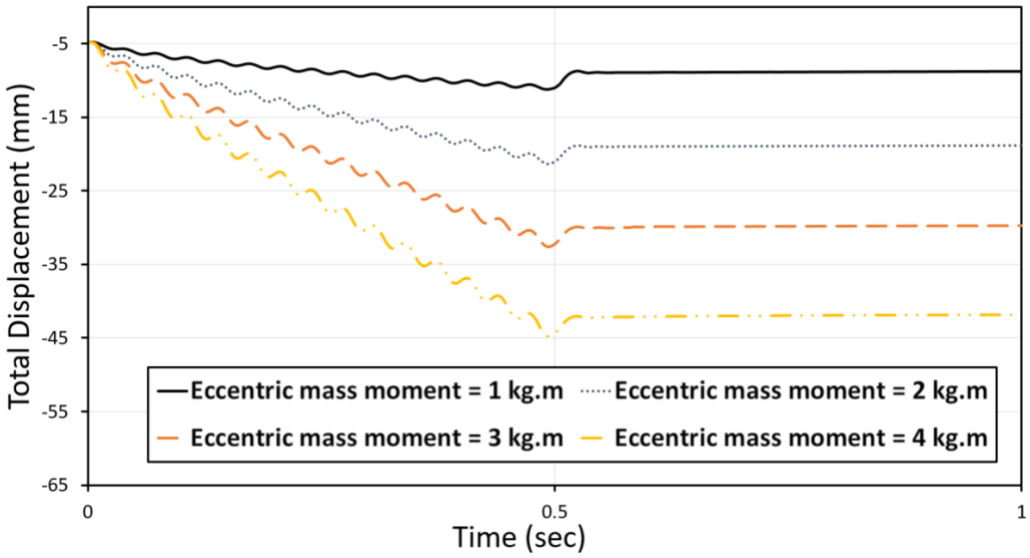

(a)

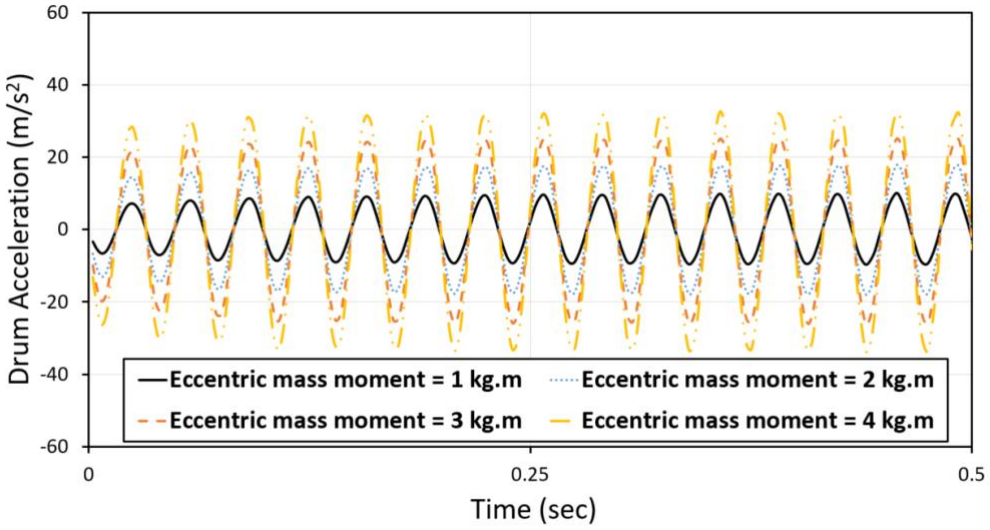

(b)

Figure 0.7 (a) Accumulation of soil displacement verses time in conjunction with different roller masses; and (b) drum acceleration verse time

Additionally, the similar correlation between the acceleration and eccentric mass moment was observed by Pietzsch and Poppy (1992), while the drum acceleration amplitude increased with the drum excitation mass moment. Corresponding to the

operating eccentric mass moment $m_0 e_0$ = 4 kg.m, the drum showed the maximum acceleration response with time as a result of the highest excitation force.

Due to the constant weight of roller, when the excitation force is more (i.e. higher $m_0 e_0$), the corresponding acceleration is consequently more. Thus, the drum acceleration increased with eccentric mass moment as observed in Figure 4.7(b). Obviously, a low eccentric mass moment from vibratory roller results in less accumulation of soil displacement in the soil in comparisons to the high eccentric mass moment. As recommended by Kenneally et al. (2015), to avoid the irregular vibration induced by chaotic jump or bifurcation for the very dense soil, the lower eccentric mass should be utilised in finishing passes.

4.4.3. Effects of Roller Weight

The roller mass was altered from 7,000 kg to 10,000 kg in this study for the further assessment while eccentric mass moment $m_0 e_0$ = 2 kg. m and frequency of drum equal to 30 Hz were held constant. Figure 4.8(a) shows the correlation between drum acceleration response and time for rollers of different weights.

Figure 4.8(a) examines the soil settlement with time during compaction. Indeed, the soil settlement gradually increased due to accumulated plastic deformation in the soil. The initial soil settlement corresponding to 7,000 kg roller (i.e. 4.8 mm) was less than the corresponding value for 10,000 kg roller which was 8.7 mm, due to the reduced self-weight of the roller.

Furthermore, the initial settlement because of the roller's self-weight was larger than the unloading settlement induced by the roller removal, since the initial settlement

comprised of both elastic and plastic components as evident in Figure 4.8(a). The 7,000 kg roller showed the highest acceleration response as observed Figure 4.8(b), and resulted in the most compacted state of the soil.

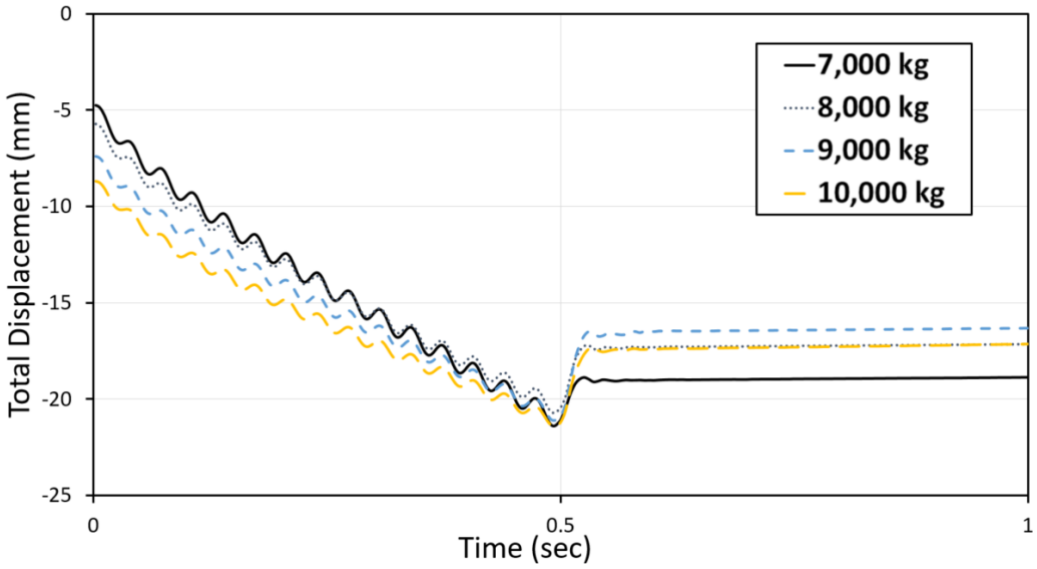

(a)

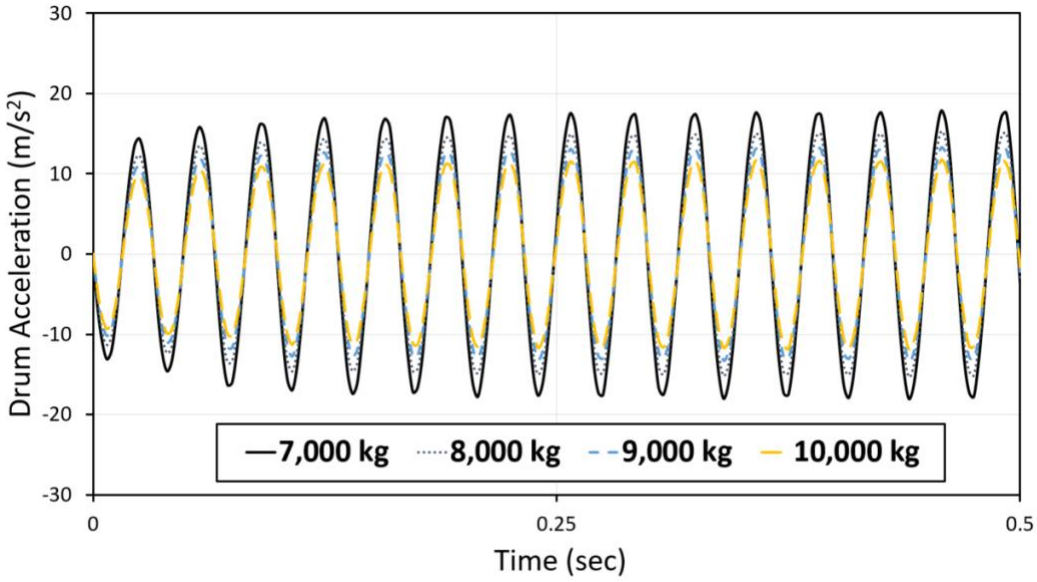

(b)

Figure 0.8 (a) Accumulation of soil displacement verses time in conjunction with different roller masses; and (b) drum acceleration verse time

It should be noted that the 7,000 kg roller exhibited the most compacted state of soil within the range of the studied parameters. The results exhibit that the soil total displacement due to compaction in-creased with the drum acceleration, which is also in close agreement with the results reported by Cao et al. (2010). While the excitation force is constant, the increased weight of roller resulted in reduced the roller acceleration and therefore vibratory compaction. Obviously the 7,000 kg roller resulted in least initial settlement (see Figure 4.8(a)) due to its lowest self-weight, and the largest final settlement (i.e. 19.0 mm) due to the increased vibration acceleration.

4.5. Summary

In this chapter, the dynamic load of the roller is explicitly applied to the vibratory roller to research the impacts of the roller parameters. The numerical predictions indicated that the adopted constitutive model captures the surface settlement of compacted soil subjected to roller vibratory. The results based on the numerical modelling reveal that when the vibration frequency was the closest to the natural first mode frequency, the maximum surface settlement was achieved. The results of soil settlement due to the self-weight of the roller being larger than the soil expansion after removal of the roller exhibited the loading stage comprised of both elastic and plastic components. In addition, an increase in the eccentric mass moment leads to an increase in the final surface settlement. However, the higher eccentric mass moment should be avoided in the finishing passes to avoid over-compaction.

According to the numerical results, the proposed approach is able to capture the complex soil-drum behaviour. The specific model can be utilised to interpret the IC predictions and optimise the process, which can be used as potential guidance by

practicing engineers and construction teams on selecting the best roller vibration frequency and amplitude choice to achieve high-quality compaction.

Chapter 5

Real-Time Determination of Sandy Soil Stiffness during Vibratory Compaction Incorporating Machine Learning Method for Intelligent Compaction

5.1. General

An emerging real-time ground compaction and quality control, known as IC, has been applied to efficiently optimising the full-area compaction. Although IC technology can provide real-time assessment of uniformity of the compacted area, accurate determination of the soil stiffness required for quality control and design remains challenging.

In this chapter, a novel and advanced numerical model simulating the interaction of vibratory drum and soil beneath is developed. The model can evaluate the nonlinear

behaviour of underlying soil subjected to dynamic loading by capturing the variations of damping with the cyclic shear strains and degradation of soil modulus. The interaction of the drum and the soil is simulated via the FEM to develop a comprehensive dataset capturing the dynamic responses of the drum and the soil.

Indeed, more than a thousand 3D dynamic FE models, covering various soil characteristics, roller weights, vibration amplitudes and frequencies were simulated. The developed dataset is then used to train the inverse solver using an innovative ML approach to simulate the stiffness of the compacted soil by adopting drum acceleration records. Furthermore, the impacts of the amplitude and frequency of the vibration on the level of underlying soil compaction are discussed. The proposed machine learning approach is promising for real-time extraction of actual soil stiffness during compaction. Results of the study can be employed by practicing engineers to interpret roller drum acceleration data to estimate the level of compaction and ground stiffness during compaction.

5.2. Introduction

Implementing the stiffness-based soil compaction has recently gained an increasing interest during earthworks due to the popularity of the mechanistic pavement design procedures (Mooney, 2010; Mooney and Facas, 2013; Nazarian et al., 2020; Fathi et al., 2021a). The compacted soil must provide enough capacity to withstand the stresses from the top layers of the road, or the dynamic loads transmitted from the vehicles or trains and experience the minimal deformations (Ranasinghe et al., 2017; Scott et al., 2020; Hu et al., 2019).

Figure 5.1 shows the typical vibratory roller used for compaction of geomaterials, while the magnitude of the centrifugal force (F_{ecc}) can be automatically adjusted based on the contact force (F_{c}). The steady-state dynamic behaviour of the vibratory roller during vibration due to the centrifugal force applied to the drum via rotating eccentric mass can be written as below:

$$m_d\ddot{z}_d = F_{ecc} + m_d g + (z_d - z_f)k_f + (\dot{z}_d - \dot{z}_f)c_f - F_c \tag{5.1a}$$

$$m_f\ddot{z}_f = m_f g + (z_f - z_d)k_f + (\dot{z}_f - \dot{z}_d)c_f \tag{5.1b}$$

$$F_{ecc} = m_0 e_0 \omega^2 \cos(\omega t) \tag{5.2}$$

where k_f and c_f are the suspension modulus and suspension damping, respectively.

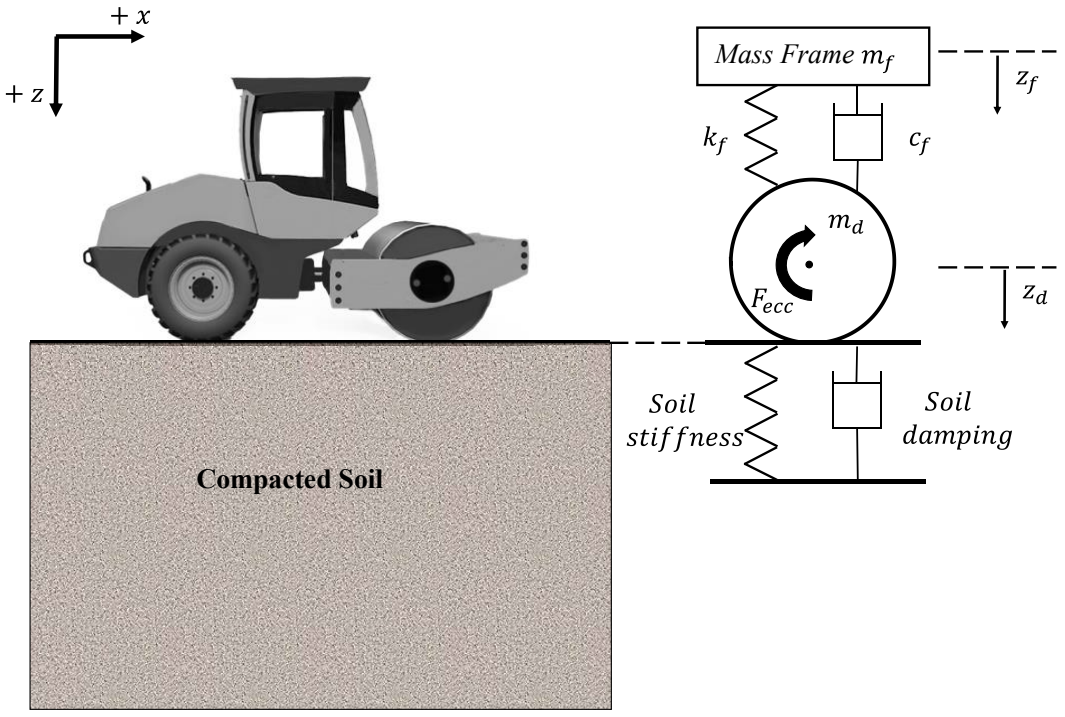

Figure 0.1 Interaction behaviour between vibratory roller and compacted soil

The physical models capturing the roller characteristics and the properties of compacted geomaterial were utilised to estimate the soil-drum behaviour (Pei and Yang, 2018). The majority of experimental research was carried out to better understand and examine the influences of drum characteristics on the achieved soil stiffness during compaction (Mooney and Rinehart, 2009).

Van Susante and Mooney (2008) applied a simplified numerical method based on an added mass technique for soil modelling to evaluate the roller-integrated experimental data to reflect the interaction between the soil and the drum. However, due to the excessively simplified assumptions for dissipative and inertial properties in this technique, a site-specific calibration would be necessary (Kenneally et al., 2015). Additionally, Buechler et al. (2012) demonstrated that the DEM is capable of simulating the soil-structure interaction and evaluating the mechanical responses as well as macroscopic deformations based on microstructural interactions.

However, the very long computational time for DEM does not yet allow this technique to be used for the real-time assessment of compaction levels (Beainy et al., 2014; Fathi, 2020). Although Mooney and Facas (2013) attempted to optimise the modelling features and size using BEM, those models still cannot explicitly portray the soil-drum system accurately and need iterative processes and indirect means to capture the soil response (Mooney and Facas, 2013; Fathi, 2020).

Several researchers used the FEM, adopting a continuum-based computational technique to explain the interaction mechanism between drum and soil (Xu et al., 2012; Erdmann and Adam, 2014; Kenneally et al., 2015; Herrera et al., 2018; Fathi, 2020; Nazarian et al., 2020). Kenneally et al. (2015) used a 2D FEM adopting a linear elastic

constitutive soil model for a uniform soil profile to explore the impacts of the compacted layer modulus and thickness on the dynamic response of the roller.

Since the simplified 2D model assumes a uniform load distribution along the drum length, 3D models capturing a more realistic distribution of load below the roller are certainly more accurate and preferable. For example, Fathi (2020) adopted a 3D finite model to evaluate responses of the compacted soil layer during roller proof-mapping.

It should be noted that the majority of studies simulating the interaction between the roller and drum explicitly considered the linear elastic (Van Susante and Mooney, 2008; Mooney and Facas, 2013) or viscoelastic soil models (Erdmann and Adam, 2014; Herrera et al., 2018). Indeed, many previous studies have shown that considering soil nonlinearity subjected to cyclic loading is paramount when soil deformation or reaction forces need to be predicted, and thus suitable constitutive models often with many model parameters need to be adopted in the modelling (Saberi et al., 2020; Liu et al., 2014).

However, practicing engineers need constitutive models with fewer parameters that can be obtained from common geotechnical tests or from the existing correlations to other soil parameters (Brinkgreve et al., 2016; Alzabeebee, 2021). For example, the addition of the Rayleigh damping feature to linear elastic models can somehow compensate for the missing hysteresis damping, while stiffness degradation and dependency of parameters to stress level and number of loading cycles need more rigorous constitutive models (Kontoe et al., 2011; Alzabeebee, 2021). In general, a reasonable soil constitutive model needs to capture variations of soil damping and stiffness with the cyclic shear strain and cumulative plastic deformations during cyclic loading.

With the increasing demand for earthworks, particularly for infrastructure projects advancement of IC, the solutions for the dynamic behaviour of interacting systems have been utilised as the prominent basis of more recent modellings. Fathi et al. (2021a) integrated the data from the 3D numerical modelling and field to assess the depth of influence of IC rollers. They exhibited an interrelationship between the soil type and the influence depth. Results illustrated that as geomaterial became more granular, the depth of influence would increase, while the influence would decrease as the soil became more cohesive.

In addition, IC technology by integrating dynamic mechanical solutions with artificial intelligence has recently been carried out to increase the compaction quality. Cao et al. (2021) adopted an Artificial Neural Network (ANN) to predict CMV based on the roller-related factors, which is consistent with the collected test data. An et al. (2020) proposed an approach to optimise the compaction process using a Genetic Algorithm (GA) to decide the number of passes. These solutions demonstrate the possibility of using new techniques to efficiently enhance the accuracy of IC results.

In this chapter, the HS-Small constitutive model was employed to simulate the various soil properties and investigate the interaction of the vibratory drum and the soil beneath. The key motivation for this chapter is to establish a rigorous and efficient method that can rapidly and accurately extract the compacted soil stiffness according to the vibratory response of the drum. Therefore, results of more than a thousand 3D numerical models were adopted to develop a dataset covering loose to dense sandy soils, roller weights, vibration amplitudes and frequencies. The developed dataset was then used to train the inverse solver using X-SVR with the GGK function to estimate the stiffness of the compacted soil adopting drum acceleration records.

5.3. Development of Three-Dimensional Numerical Model

5.3.1. Overview of the Model

The evaluation of the dynamic response between the roller and compacted underlying soil was performed employing PLAXIS 3D. Figure 5.2(a) exhibits the 3D view of the cylindrical rigid drum roller resting on the soil layer. The adopted roller drum was 0.75 m in radius and 2.1 m in length, corresponding to typical drum sizes used in Australia for earthworks in major infrastructure projects. The weight of the roller was considered as a variable changing between 6 t and 20 t.

To simulate the behaviour of a vibrating drum, an eccentric mass m_0 rotating around the axle of the drum with an effective moment arm e_0 was considered to induce the centrifugal force corresponding to the eccentric mass moment $m_0 e_0$ varying between 1 kg m and 9 kg m (Figure 5.2(b)). In addition, the applied excitation frequency ranged from 20 Hz to 35 Hz, which together with different eccentric mass moments, could result in a wide practical range of centrifugal forces (F_{ecc}) as in Equation (5.2).

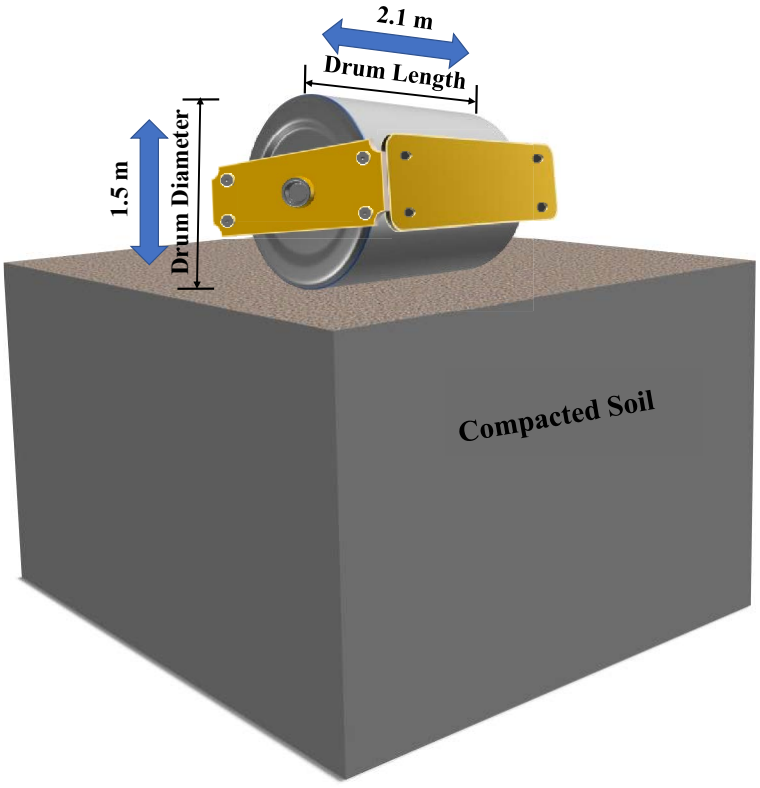

(a)

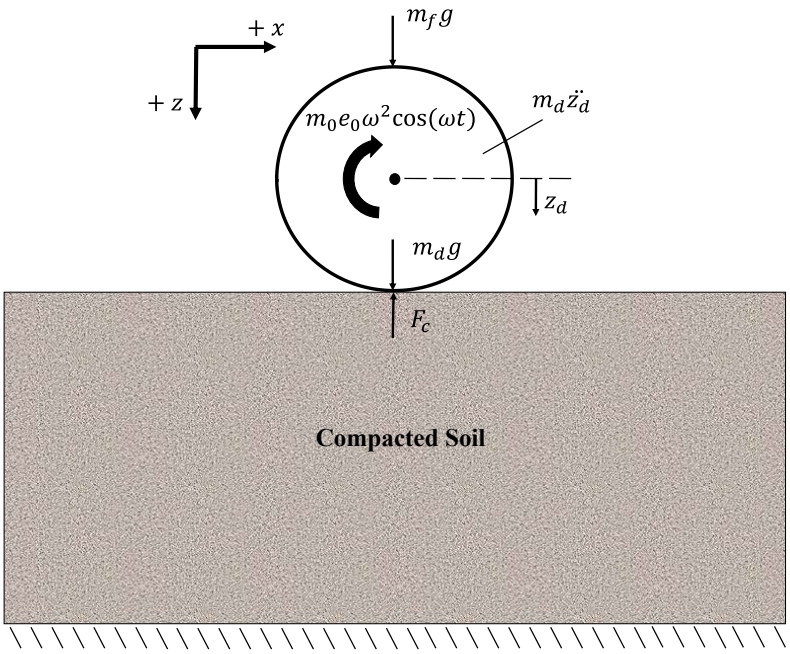

(b)

Figure 0.2 Vibratory roller compactor system: (a) Sketch of the drum, and (b) Free body diagram of one degree of freedom lumped mass model for vertical forces acting on compacted soil

In this chapter, the vibration force as in Equation (5.2) was applied to the drum via distributed line load to simulate the vibratory behaviour induced by the rotating eccentric mass. Table 5.1 summarises the adopted roller specifications and the variation ranges used in this study for parametric study.

Table 0.1 Operational values of vibratory roller adopted in single layer soil properties extraction.

Parameter	**Unit**	**Minimum**	**Maximum**
Radius of drum	m	0.75	0.75
Length of drum	m	2.1	2.1
Mass of roller	kg	5000	20,000
Eccentric mass moment	kg m	1	9
Vibration excitation frequency	Hz	15	35

5.3.2. Modelling of the Single Layered Soil Strata

The nonlinear elastoplastic stress-strain relationship is typically observed in soils subjected to dynamic loading (Han et al., 2016). It is important to employ well-established models to simulate the variations of resilient modulus, helping to characterise the nonlinear response of underlying soil under cyclic loading (Nazarian et al., 2020; Ooi et al., 2004). In this chapter, the HS-Small model was applied to simulate the cyclic behaviour of sandy soils, and the pressure dependency of the modulus, which is critical for sandy soils, was captured. For a detailed explanation of each input parameter, please refer to Section 4.3.2.

According to Brinkgreve et al. (2016), these key stiffness inputs required in this model are: (i) E_{oed}, (ii) E_{50}, and (iii) E_{ur}, as captured in Chapter 2, Section 2.5.3. Furthermore, the hyperbolic function between the vertical strain, ε_1, and the deviatoric stress, q, is the fundamental concept for the formulation of the HS-Small model and could be given by the below equation:

$$-\varepsilon_1 = \frac{2 - R_f}{2E_{50}} \frac{q}{1 - \frac{q}{q_a}} \tag{5.3}$$

where q_{a} is the asymptotic value of the shear strength. Additionally, the HS-Small model is specifically designed to simulate the soil plasticity and hysteretic damping of soil at large and small strains, respectively, while considering isotropic hardening (Brinkgreve et al., 2007; Schanz et al., 2019). The model incorporates the modified Hardin and Drnevich (1972) model as proposed by Dos Santos and Correia (2001) for strain-dependent stiffness, as in Equations. (5.4) and (5.5):

$$G_s = \frac{G_0}{1 + \frac{\alpha\gamma_c}{\gamma_{0.7}}} \tag{5.4}$$

$$G_0 = G_0^{ref} \left(\frac{c\ cos\varphi\ - \sigma_3 sin\varphi}{p^{ref} sin\varphi\ + c\ cos\varphi} \right)^m \tag{5.5}$$

where G_0 and G_{s} are small-strain and secant shear stiffnesses, receptively; γ_{c} is the shear strain; $\gamma_{0.7}$ represents the shear strain at which $G_S/G_0 = 0.7$; and G_0^{ref} is the shear modulus at the reference pressure p^{ref}. It is advised to set the model parameter α (the constant in Equation (5.4)) to 0.385 in order to reach a satisfactory agreement with laboratory measurements. The small strain tangent shear modulus (G_{t}) is calculated from Equation (5.6).

$$G_t = \frac{G_0}{\left(1 + \frac{\alpha\gamma_c}{\gamma_{0.7}}\right)^2} \geq G_{ur} \tag{5.6}$$

where G_{ur} is the unloading/reloading shear modulus. Additionally, the model implicitly captures the soil hysteretic damping via stiffness degradation with the governing equations as follows:

$$\xi = \frac{E_D}{4\pi E_S} \tag{5.7}$$

$$E_D = \frac{4G_0\gamma_{0.7}}{\alpha}\left[2\gamma_c - \frac{\gamma_c}{1 + \frac{\gamma_{0.7}}{\alpha\gamma_c}} - \frac{2\gamma_{0.7}}{\alpha} ln\left(1 + \frac{\alpha\gamma_c}{\gamma_{0.7}}\right)\right] \tag{5.8}$$

$$E_S = \frac{1}{2}G_S\gamma_c^2 = \frac{G_0\gamma_c^2}{2 + \frac{2\alpha\gamma_c}{\gamma_{0.7}}} \tag{5.9}$$

where ξ is the hysteretic damping ratio; and E_{D} and E_{S} are the dissipated energy and the cyclic maximum strain energy in a single loading cycle, respectively.

Table 0.2 Adopted soil parameter for hardening soil model with small-strain stiffness for different relative densities (RDs)

Parameter	RD = 20%	RD = 30%	RD = 40%	RD = 50%	RD = 60%	RD = 70%	RD = 80%	RD = 90%
$p^{ref}(kPa)$	100	100	100	100	100	100	100	100
$\gamma\ (kN/m^3$	15.8	16.2	16.6	17	17.4	17.8	18.2	18.6
$E_{50}^{ref}(kpa)$	12,000	18,000	24,000	30,000	36,000	42,000	48,000	54,000
$E_{oed}^{ref}(kpa)$	12,000	18,000	24,000	30,000	36,000	42,000	48,000	54,000
$E_{ur}^{ref}(kpa)$	36,000	54,000	72,000	90,000	108,000	126,000	144,000	162,000
$G_0^{ref}(kPa)$	73,600	80,400	87,200	94,000	100,800	107,600	114,400	121,200
m	0.6375	0.6063	0.5750	0.5438	0.5125	0.4813	0.4500	0.4188
$\gamma_{0.7}$	1.8E-04	1.7E-04	1.6E-04	1.5E-04	1.4E-04	1.3E-04	1.2E-04	1.1E-04
φ'	30.5	31.75	33	34.25	35.5	36.75	38	39.25
ψ	0.5	1.75	3	4.25	5.5	6.75	8	9.25
R_f	0.975	0.963	0.950	0.938	0.925	0.913	0.900	0.888
ϑ_{ur}	0.2	0.2	0.2	0.2	0.2	0.2	0.2	0.2

The key motivation for this study is to develop an advanced tool that can rapidly and reasonably extract the compacted soil stiffness for sandy soil based on the vibration responses of the drum during compaction. Thus, in order to investigate the drum responses under various soil properties, different states of sandy soil ranging from relative density RD = 20% to 90% were considered to address the soil properties from loose to dense from early stages of compaction to a well-compacted condition. Table 5.2 summarises the adopted soil characteristics corresponding to different relative densities for the HS-Small model following the formulations proposed by Brinkgreve et al. (2010b). Figure 5.3(a) and (b) exhibits the damping ratio and stiffness degradation curves adopted in the study, respectively. In addition, the water table was considered to be deep, leading to no significant excess pore water pressure being generated during the compaction process (Fatahi et al., 2020).

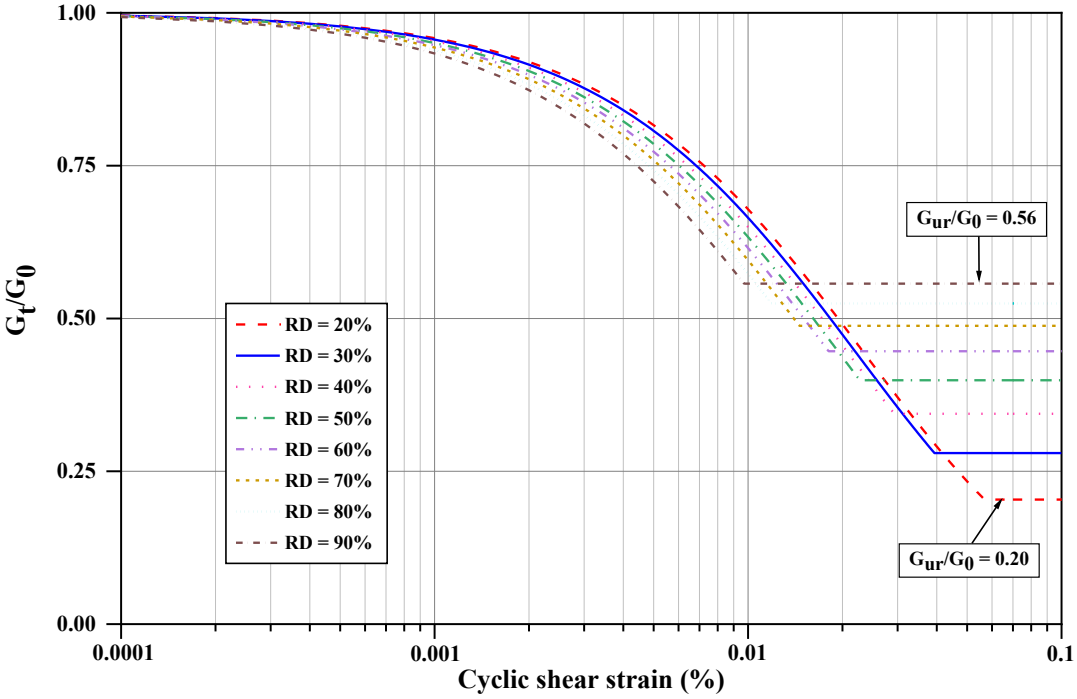

(a)

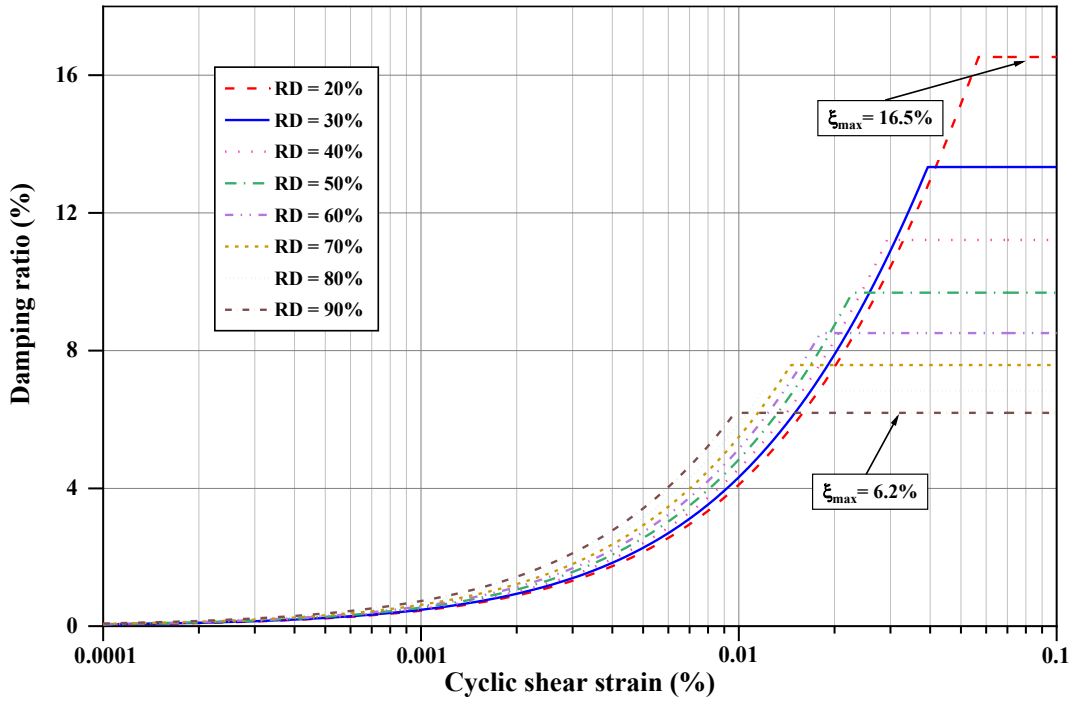

(b)

Figure 0.3 (a) Tangent shear modulus degradation curve for different relative densities, and (b) damping ratio curves for different relative densities

5.3.3. Geometrical Characteristics of the Single Layered Soil Model

Referring to Figure 5.4, to characterise the interaction between the drum and underlying soil, a 3D numerical model of a vibrating drum on a soil deposit was established to predict the time history of the roller acceleration response during vibration. To simulate the weight of the roller, gravity load was employed on the rigid drum. Moreover, the vibratory loading of the drum was achieved by applying the eccentric force as in Equation (5.2). It should be noted that no horizontal forces were applied to the roller, assuming that the eccentric mass configuration inside the drum, which rotates along the longitudinal axis of the drum, nullified the horizontal forces (Van Susante and Mooney, 2008).

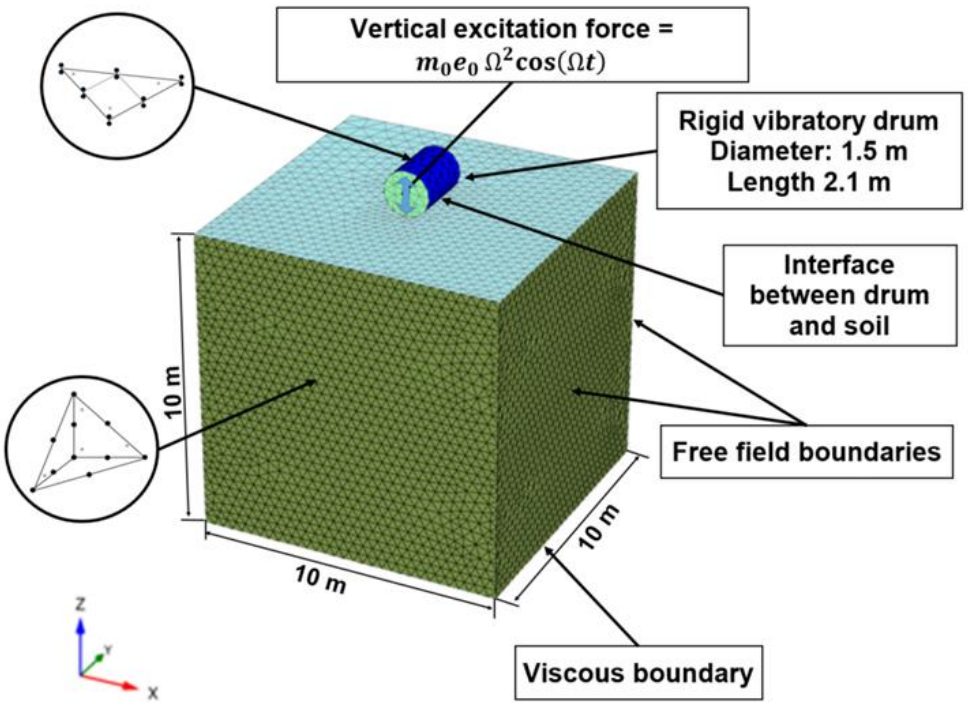

Figure 0.4 Adopted numerical model designed for the unbound soil with free-field and viscous boundaries conditions

For the sake of accuracy and minimising the boundary effects, a block of soil that was 10 m in length, 10 m in depth, and 10 m in width was modelled by applying the 10-node tetrahedral elements as shown in Figure 5.4. Each node in the underlying soil had three degrees of freedom which allowed a second-order interpolation for displacement, making the arrangement suitable for dynamic analysis. In addition, the influence depth of the adopted vibratory roller was simulated to be 0.6-1 m (Adam, 2007). Consequently, a 10-m deep soil deposit is deemed sufficient for minimising the boundary effects.

There were nearly 190,000 elements in each of the FEM, and each of the numerical models adopted four different loading phases, including initial equilibrium of soil deposit, application of weight of roller drum, application of cyclic loading simulating roller vibration and equilibrium after removal of the roller and completion of the compaction. Please refer to Section 4.3.4 for roller soil interface modelling and boundary conditions.

5.4. Results and Discussion

To better understand the response of roller sitting on the geomaterial subjected to drum vibration, impacts of amplitude, drum frequency, weight of roller and the soil characteristics were investigated. This section also demonstrates the results of the training datasets from the developed inverse solver using a novel kernel-based machine learning technique to determine the soil properties according to the acceleration response of the roller and roller characteristics.

5.4.1. Effects of Vibration Amplitude of the Drum

Vibratory eccentric force amplitude, a fundamental parameter in the compaction process, directly impacts the compaction quality. Therefore, the eccentric mass moment varying from 1 kg m to 9 kg m was adopted to assess the influences of the excitation force amplitude on the interaction between drum and soil. Figure 5.5 shows a predicted example corresponding to different eccentric force amplitudes for the soil relative density of 60% while keeping a constant mass of drum (i.e. 10,000 kg) and a constant frequency (i.e. $f = 25$ Hz).

The compacted soil surface and the vibratory drum kept continuous contact throughout the entire vibration period. It should be cognizant that a lower eccentric mass moment is frequently used for the finishing passes and proof rolling to prevent over compaction, while a higher eccentric mass moment provides larger excitation force amplitudes at the initial stage of construction to achieve a higher degree of compaction (Kenneally et al., 2015).

Figure 5.5(a) demonstrates the time history of soil surface settlement beneath the drum with various eccentric mass moments. Referring to Figure 5.5(a), the cumulative soil settlement gradually increased as a result of cyclic loading with the highest settlement observed when $m_0 e_0 = 9$ kg m, and a reduction in geomaterial settlement was observed as a result of a reduction in the eccentric mass moment, similar to observations from other studies (Masad et al., 2016; Ma et al., 2021).

Because of the constant weight of the roller and operation frequency, the excitation force was directly influenced by the eccentric mass amplitude, where amplified eccentric mass moment corresponded to the increased acceleration experienced by

the drum, as observed in Figure 5.5(b). Indeed, for the adopted case here, to achieve a higher degree of compaction, a high eccentric mass moment from the vibratory drum could help increase the soil compression level and vice versa. However, as Kenneally et al. (2015) suggested, high eccentric masses should be avoided in the finishing passes, which would induce irregular drum behaviour caused by bifurcation of the chaotic jump for the densely compacted underlying soil.

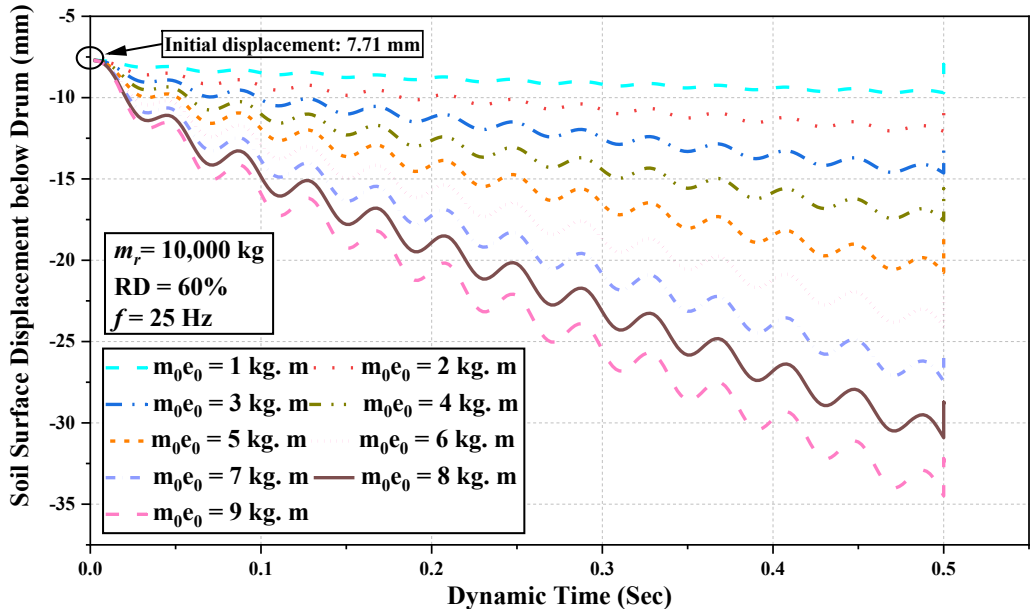

(a)

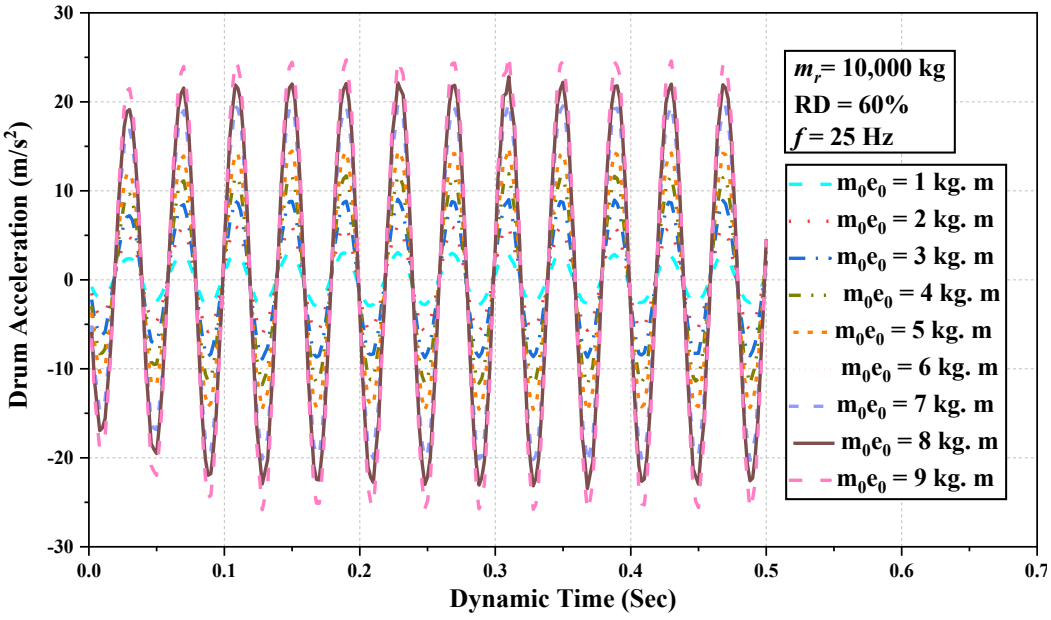

(b)

Figure 0.5 (a) Soil surface settlement, and (b) drum acceleration response for different eccentric mass moments

5.4.2. Effects of Vibration Frequency of the Drum

The choice of vibratory roller frequency is crucial for soil compaction (Wersäll et al., 2017). In this study, the operation frequency of the vibratory roller was altered between 20 Hz and 35 Hz. For example, prediction for *RD* = 60%, corresponding to the unit weight of 17.4 kN/m^3, while the mass of the roller was equal to 10,000 kg and the eccentric mass moment was equal to 5 kg m, is presented in Figure 5.6.

Referring to Table 5.2 for the corresponding soil parameters, the average shear wave velocity (S-wave) and compressional wave velocity (P-wave) of the soil deposit at $p^{\mathrm{ref}} = 100$ kPa were 238.4 m/s and 389.3 m/s, respectively. The first natural frequency of underlying properties (i.e. $V_{\mathrm{p}}/(4H)$), considering the roller influence depth of 0.6–1 m (Adam, 2007), was estimated to be 97-162 Hz, which is well above the adopted vibration frequency of the drum, and thus no resonance condition was observed.

Figure 5.6 presents the surface displacement of the compacted subgrade with dynamic time as a function of changing vibratory roller operation frequency. The results exhibit that an increase in the operation frequency led to increased compacted soil settlement. Numerical predictions show that the highest degree of soil compaction for the adopted sandy soil was achieved when the frequency was equal to 35 Hz, which illustrated that the roller could achieve the optimum compaction when the roller frequency was closer to the first mode natural frequency of the ground, which is consistent with observations made by other researchers (Masad et al., 2016; Wersäll and Larsson, 2016).

Referring to the case with a drum vibration frequency of $f = 35$ Hz as in Figure 5.6, the initial soil displacement due to roller static gravity load was 7.7 mm, and the maximum vertical displacement reached 25.9 mm at the end of the dynamic phase, and then resumed to 23.98 mm permanent settlement after removing the roller. The compacted soil bounced back 2 mm, which was well less than the initial settlement of 7.7 mm, which clearly shows that the unloading phase comprised only elastic deformation, whereas the initial loading stage subjected to the weight of the roller included both plastic and elastic components.

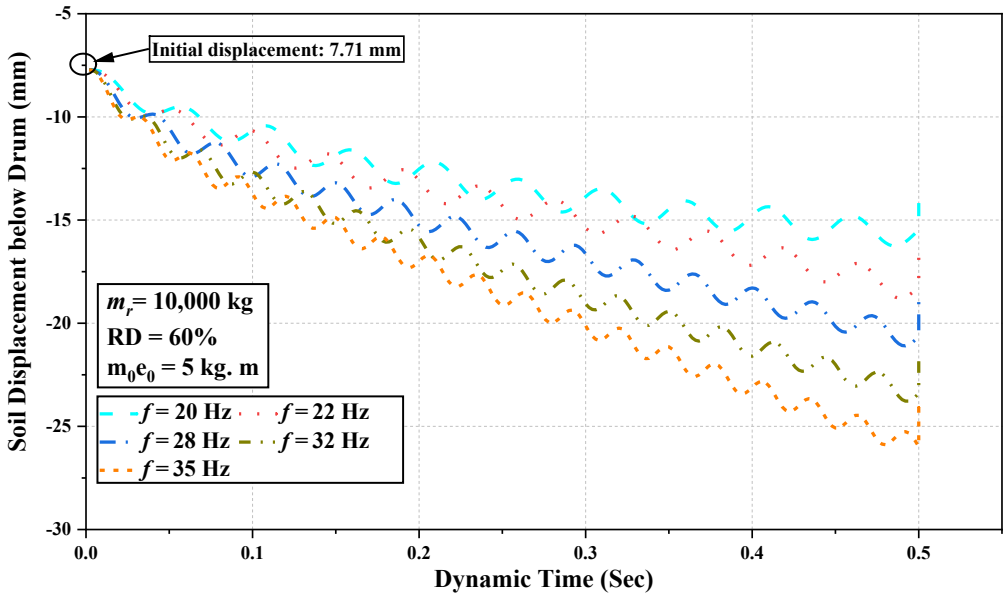

Figure 0.6 Soil settlement verse dynamic time for different vibration frequencies

Figure 5.6 explains that the plastic deformation increases due to soil settlement on each dynamic loading cycle as the dynamic duration raises. The irreversible deformation of the selected sandy material reveals that the soil yield stress has gradually increased (Xu et al., 2022a) . Indeed, the excitation frequency near the natural frequency of compacted soil (i.e. $f = 35$ Hz in this study) resulted in more soil compaction and ground settlement as expected (Pietzsch and Poppy, 1992). Thus,

as the vibration frequency reduced (less than the first mode natural frequency of the ground), the cumulative soil displacement decreased, as shown in Figure 5.8.

5.4.3. Effects of Roller Mass

The mass of the roller (m_r) was incrementally changed from 6000 kg to 20,000 kg to investigate its effects on the drum-soil interaction. As an example of results corresponding to the soil relative density of *RD* = 60%, the impacts of the mass of the roller are presented in Figure 5.7, while the frequency of vibratory roller was equal to 25 Hz and the eccentric mass moment was $m_0 e_0 = 5$ kg m. Figure 5.7(a) illustrates the impacts of the roller mass on the initial soil displacement because of the weight of the roller and cumulative soil displacement after 10 cycles of loading. Moreover, Figure 5.7(b) demonstrates the accumulated soil settlement varying with dynamic time for the 12,000 kg roller, which obviously examines how the cumulative plastic deformations in the soil gradually increased.

The initial settlement due to gravity loading alone for the heavier roller (i.e. 20,000 kg roller, 22.5 mm initial settlement) was more than the initial settlement for the lighter roller (i.e. 6000 kg roller, 4 mm initial settlement) because of the enhanced static pressure implemented to the compacted soil. For the 12,000 kg roller with operation eccentric mass moment $m_0 e_0 = 5$ kg m (Figure 5.7(b)), the unloading soil displacement (i.e. 2.25 mm) due to the roller removal was smaller than the initial displacement (i.e. 9.85 mm), highlighting that the initial settlement included both plastic and elastic components.

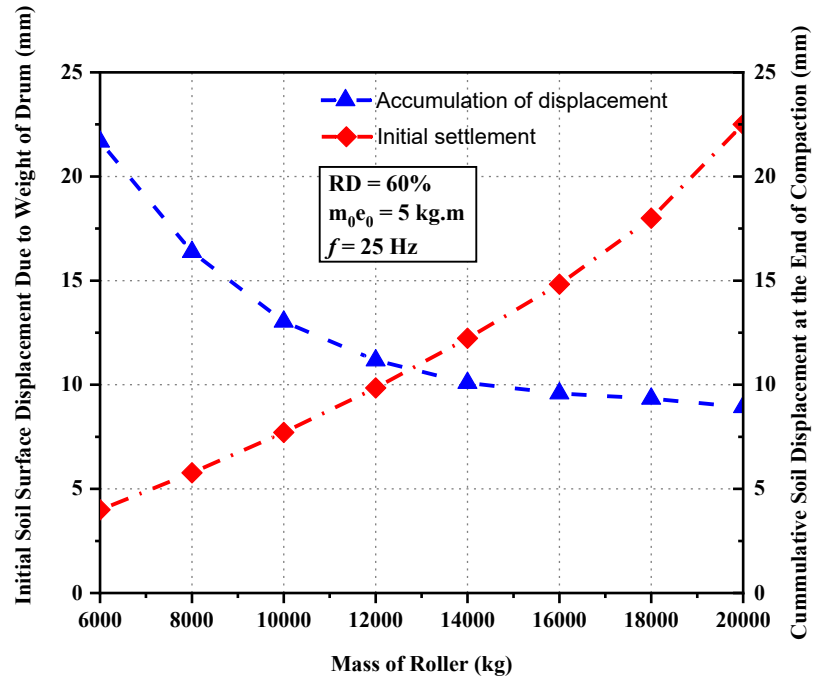

(a)

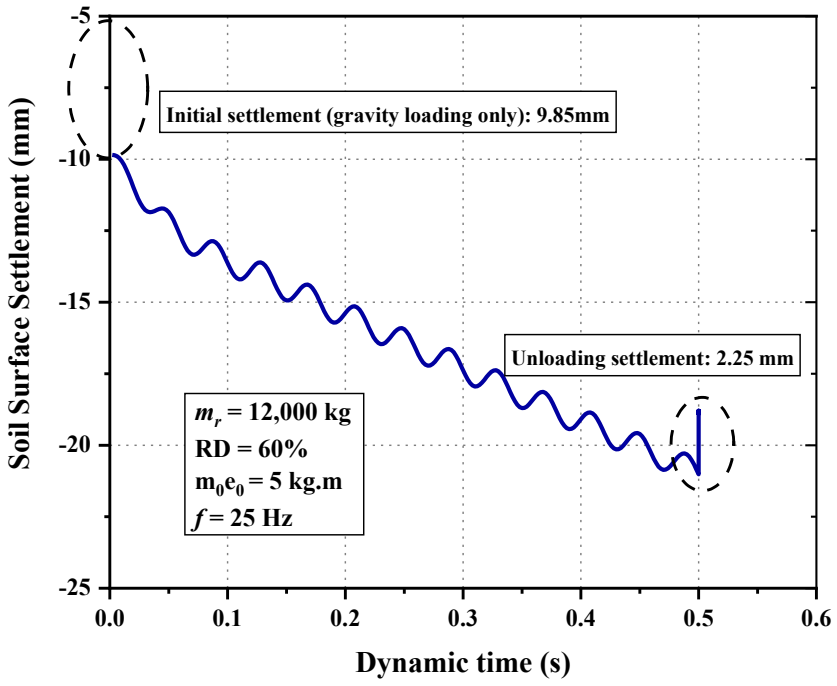

(b)

Figure 0.7 (a) Initial soil settlement, and (b) time dependent soil displacement

Referring to Figure 5.8, the lightest 6000 kg roller had the highest acceleration responses and caused the highest values of the cumulative soil displacement after the completion of roller compaction. The predictions indicate that with increasing roller acceleration, the total settlement of compacted soil increased, and it is consistent with the observations made by Cao et al. (2010). For a given centrifugal force, the added weight of the roller lowered the roller acceleration and vibratory compaction.

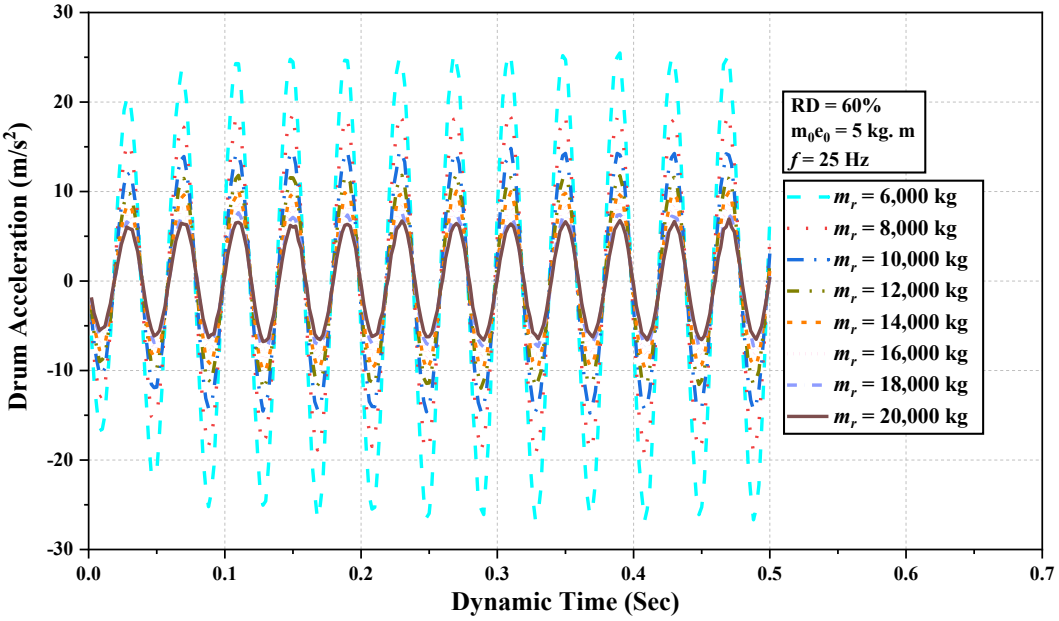

Figure 0.8 Drum acceleration verses dynamic time for different roller masses

5.4.4. Evaluation of the Machine Learning Method

To illustrate the feasibility of using machine learning to back calculate the soil stiffness based on the drum acceleration response, the comprehensive results from the 3D numerical modelling were used. The newly proposed generalised Gegenbauer, a series expansion of the Gegenbauer polynomial (Stein and Weiss, 2016), was implemented herein as the kernel for the X-SVR method to train and test the experimental data. In this study, there were 1405 sets of data from the 3D numerical

method, which were used to examine the ability of machine learning to determine compacted soil stiffness. Among them, 405 sets of data (around 30% of the total datasets) were randomly selected to train the network, and 1000 sets of data (around 70% of the total datasets) were used to test the trained network.

It should be noted that several research studies utilised a large portion of data for testing and evaluation. For example, the selection of 30% training data and 70% testing data was employed by Lin et al. (2017) for target classification through a convolutional highway unit which is a novel architecture developed based on the convolutional neural network (CNN), and the classification accuracy of the model could reach 94.47%. In addition, experimental data by Zainudin et al. (2016) were split into different distributions of training and testing data under different machine learning classification techniques. They showed that the data group of 30% training and 70% testing had the best results for predictions under the decision tree and random forest (RF) classification techniques, and the data group of 20% training and 80% testing had the best precisions for classification techniques of Naïve Bayes and support vector machine.

The influence depth of compacted soil is primarily contingent upon the operating parameters, dimensions, as well as weight of the roller (Fathi et al., 2021a). Adjusting various independent operating settings of the employed rollers by the driver, such as frequency and eccentric mass moment, can directly impact the progress in compaction and quality of compaction (Pietzsch and Poppy, 1992). In addition, the acceleration response of the roller is closely related to compaction level, impacting the soil stiffness (Hua et al., 2018). Indeed, to assess the real-time stiffness extraction

of the proposed numerical model based on the vibration response of the roller drum, the four physical parameters were selected as the machine learning inputs, including:

(1) the acceleration vs. dynamic time of drum ($\ddot{z}_{\mathrm{d}}$ or a_{d});

(2) frequency of dynamic loading (f);

(3) ratio of eccentric mass to drum length ($R_{\mathrm{el}} = m_0 e_0 / l$) and

(4) ratio of roller mass to drum length ($R_{\mathrm{ml}} = M/l$),

while the unloading/reloading modulus (E_{ur}) was selected as the output. It should be noted that these input parameters can be directly collected from the roller during compaction. Thus, in real practice, engineers can use the developed machine learning technique to determine equivalent properties of the soil below the roller within the influence depth of the roller. Additionally, roller operation parameters (f, R_{el} and R_{ml}) are independent and can be decided or controlled by the manufacturer or operator, and drum acceleration response ($\ddot{z}_{\mathrm{d}}$-t_{d}) is influenced by the compacted soil characteristics.

These input parameters can be directly collected from the roller without requiring further data from the soil. Moreover, to cover a wide range of vibratory roller characteristics, the applied excitation frequencies varied from 20 Hz to 35 Hz, with roller mass ranging from 5000 kg to 20,000 kg and the excitation force induced by the eccentric mass moment was set from 1 kg m to 9 kg m. Furthermore, to confirm the accuracy of the established ML method, the root mean square error ($RMSE$), coefficient of determination (R^2) and relative error (RE) were calculated from the following equations:

$$RMSE = \sqrt{\frac{1}{s}\sum_{i=1}^{s}(y_i - \hat{y}_i)^2} \tag{5.10}$$

$$R^2 = 1 - \frac{\sum_i(-y_i + \hat{y}_i)^2}{\sum_i(-\bar{y} + \hat{y}_i)^2} \tag{5.11}$$

$$RE = \frac{\hat{y} - y}{y} \times 100\% \tag{5.12}$$

where y, $\hat{y}$ and $\bar{y}$ denote the values of benchmark, prediction and the mean of the true values, respectively; while s denotes the number of samples.

Table 0.3 Comparisons of the performance of adopted machine learning techniques with different kernel functions

Kernel Functions	$RMSE_{train}$	R^2_{train}	$RE_{train}(\%)$	$RMSE_{test}$	R^2_{test}	$RE_{test}(\%)$
Gegenbauer	7.3109E+01	0.999996	0.00044	7.7336E+02	0.999485	0.51150
Linear	6.0993E+03	0.968795	0.26537	7.9158E+03	0.948700	0.61204
Polynomial	6.2967E+03	0.966725	0.28918	7.9367E+03	0.947896	0.55768
Gaussian	7.2005E+02	0.999568	0.01186	1.1838E+03	0.998782	0.16686
Exponential	1.0801E+02	0.999973	0.00262	2.4892E+03	0.994455	0.30239

To assess the accuracy of the machine learning technique for real-time feedback control, the adopted machine learning function should result in a high coefficient of determination on training and testing experimental data. The $RMSE$, R^2 and RE for the cases using different kernels, including the Gegenbauer kernel, linear kernel, exponential kernel, Gaussian kernel and polynomial kernel, are presented in Table 5.3.

The training and testing unloading/reloading moduli (E_{ur}) exhibited the best correlation with the experimental data with the Gegenbauer kernel and the R^2 for training and testing data with the Gegenbauer kernel were 0.999996 and 0.999485, respectively (Figure 5.9 (a)). In addition, the relative error of the adopted machine learning method with the Gegenbauer kernel function exhibited the lowest value, which is also reported in Figure 5.10. The average relative errors of the adopted machine learning process with the Gegenbauer kernel method for training data and testing data were less than 0.00044% and 0.512%, respectively, indicating the adopted model had high precision for both training and testing data.

The average computation time of each numerical modelling case using selected parameters for the X-SVR algorithm with the Gegenbauer kernel function was 0.2 s, which makes the machine learning technique suitable for real-time quality control by practicing engineers on site.

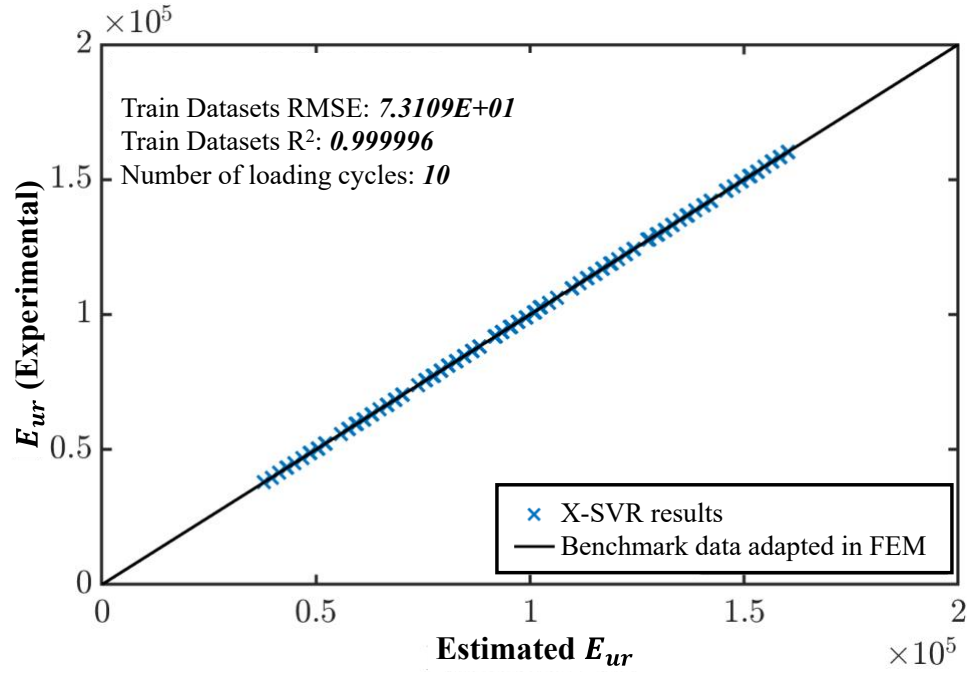

(a)

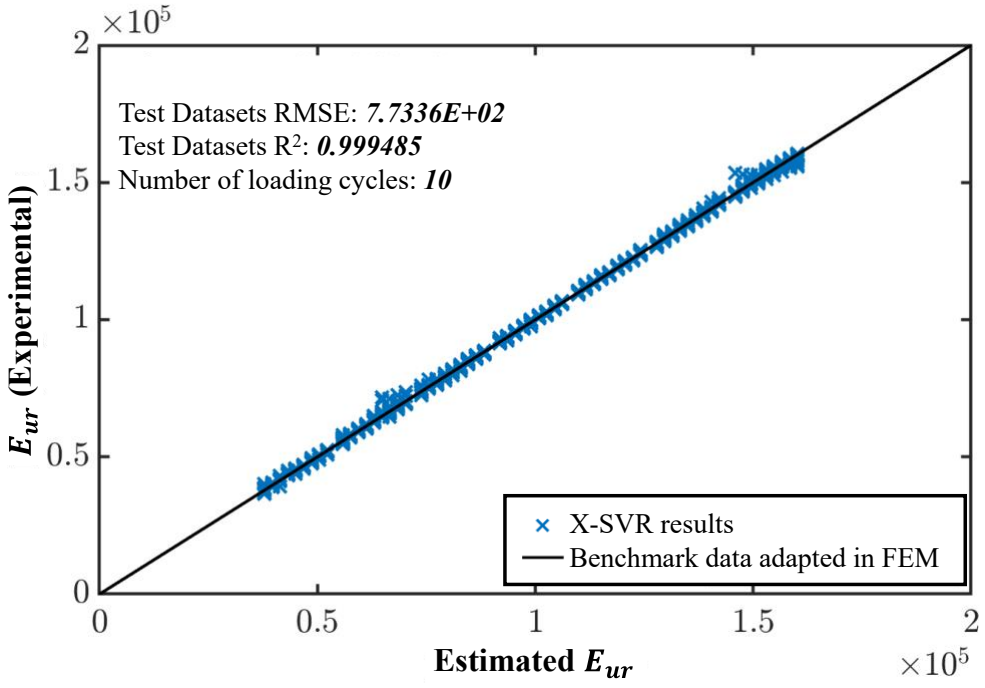

(b)

Figure 0.9 Comparison of finite element results (experiment) with machine-learning outputs (estimated) (a) trained data, and (b) tested data

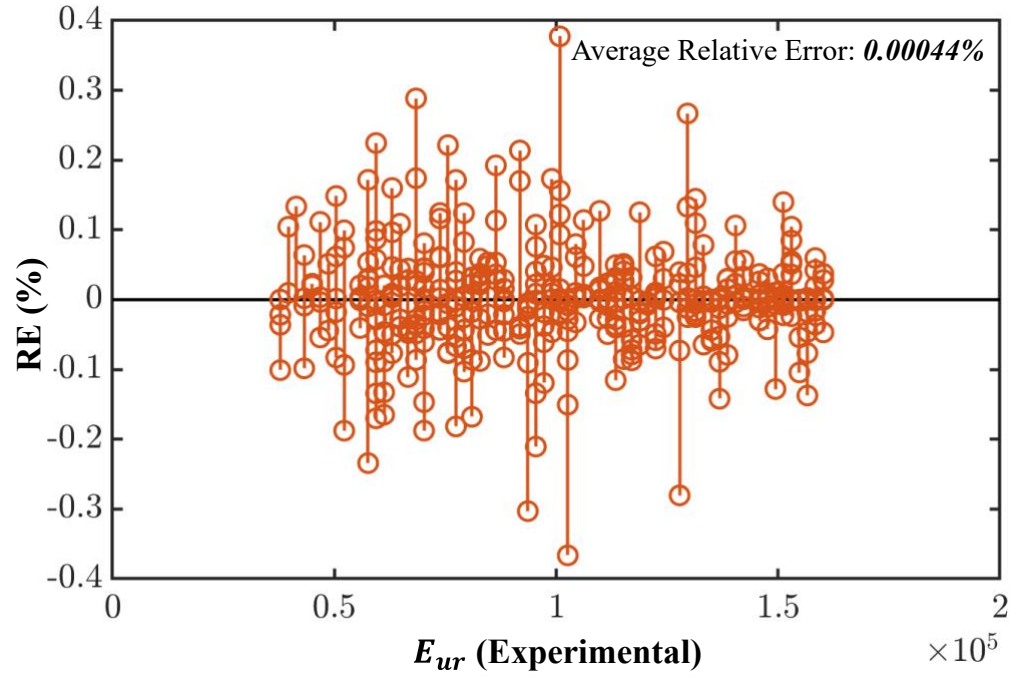

(a)

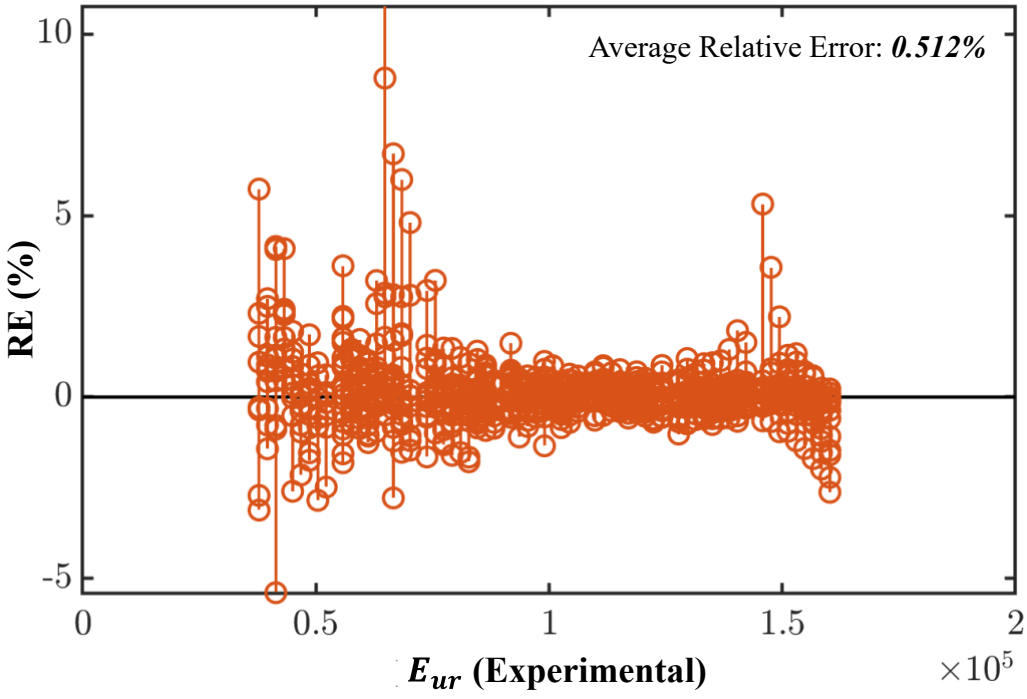

(b)

Figure 0.10 The relative errors of the machine learning predictions adopting Gegenbauer kernel for (a) trained data, and (b) tested data

The proposed X-SVR method in this study could be theoretically considered as a QP problem, which is able to efficiently capture the global optimum because of its strong convexity related to the QP problem. Furthermore, the developed scheme has been integrated with advanced kernels (e.g. GGK in this study) and an optimisation toolbox to enhance the efficiency and robustness of solving relevant problems (Wang et al., 2020).

Compared with the conventional SVR method, X-SVR can establish a higher-accuracy regression model between the inputs and outputs by utilising identical sizes of training datasets. This study applied the ANN model to comparing its performances with the adopted X-SVR. The R^2 of the ANN approach for training and testing experimental data were 0.996423 and 0.953048, respectively, and the adopted X-SVR with GGK function represented the better training and testing unloading/reloading moduli with 0.999996 and 0.999485, respectively.

Furthermore, the average *REs* of the adopted model in the study for training and testing data were less than 0.00044% and 0.512%, respectively, which is better than ANN for training and testing data, which were 0.04072% and 0.53%, respectively. While this study has clearly highlighted the great potential of machine learning in IC, further studies to assess the potential use of other ML algorithms, such as the multi-layer perceptron (MLP) feed-forward neural network model (Fathi et al., 2021b), machine learning support vector machine algorithm (Zhang et al., 2021) and RF and ANN hybrid machine learning algorithm (Fathi et al., 2019) are also recommended.

5.4.5. Effects of the Number of Loading Cycles on Prediction Using Machine Learning

Evaluating the minimum required time duration to collect drum acceleration data as input for machine learning training and predictions of the unloading/reloading modulus (E_{ur}) in real-time depends on the vibration frequency of the drum. The results of each loading cycle were analysed thoroughly, and Figure 5.11 summarises the accuracy of predictions considering the number of loading cycles used for developing a machine learning inverse solver. Referring to Figure 5.11, the coefficient of determination gradually increased due to the increased number of loading cycles used for back calculation, and after three loading cycles, minor changes in R^2 and $RMSE$ were observed. According to the implemented machine learning analyses, the results indicated that applying X-SVR with GGK when the number of utilised loading cycles was equal to or larger than three was reasonable.

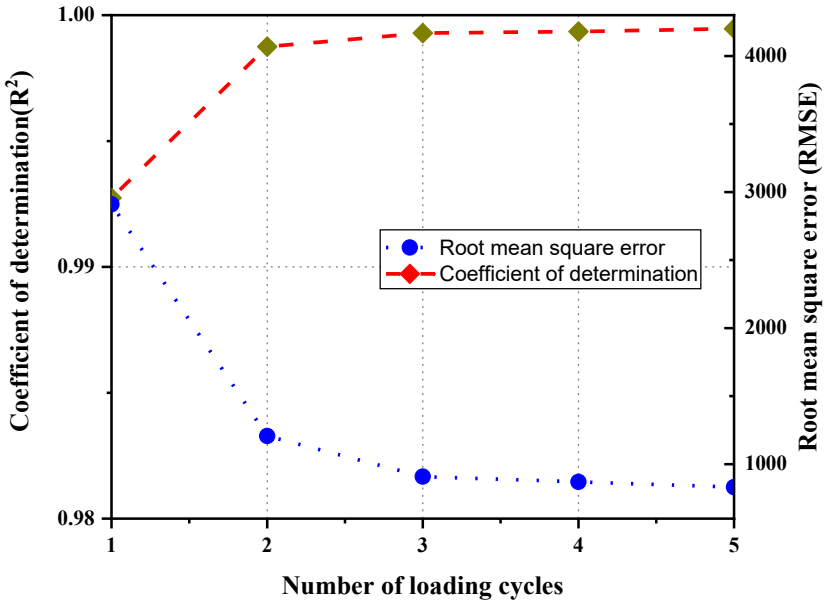

Figure 0.11 Coefficient of determination and root mean square error of machine learning method with Gegenbauer kernel vs. number of loading cycles

Figure 5.12 shows the comparison of estimated and experimental E_{ur} when three loading cycles were used in the machine learning process for training data and testing data, confirming acceptable coefficient of determination R^2.

Therefore, the minimum field time interval needed to use for real-time determination of E_{ur} using the X-SVR method with the Gegenbauer kernel can be calculated by

$$T_i = N_c \frac{1}{f} \tag{5.13}$$

where T_{i} and N_{c} denote the minimum input working period for satisfactory machine learning precision and the minimum number of loading cycles (determined to be N_{c} = 3 as in Figure 5.12), respectively. This study can be used as preliminary research for properly choosing training data and efficiently back-calculating the soil unloading/reloading modulus in real-time during the compaction process. Thus, the proposed machine learning technique can be used as feedback control, which can be used as potential guidance by practicing engineers for determining the soil unloading/reloading modulus to be used for quality assurance.

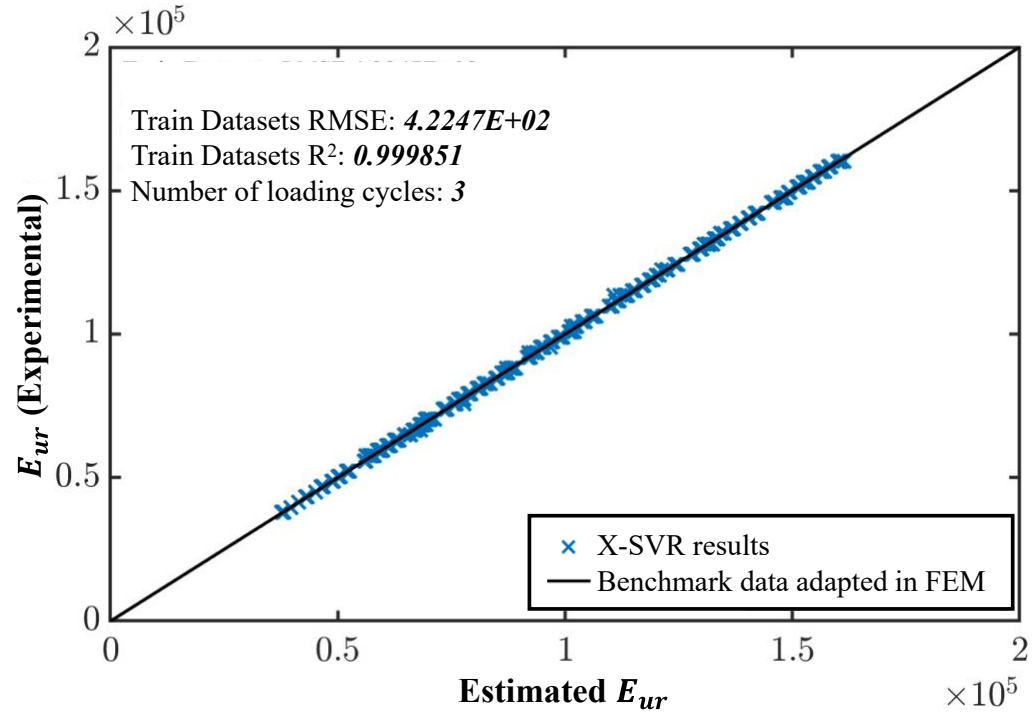

(a)

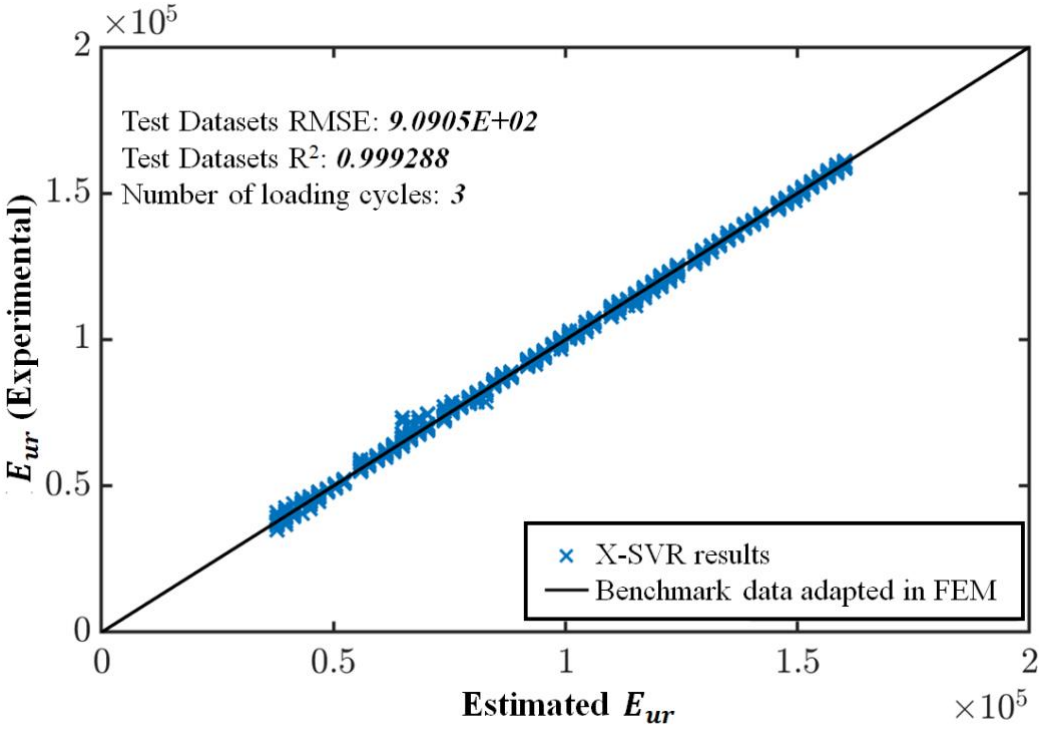

(b)

Figure 0.12 The relative errors of the machine learning predictions adopting Gegenbauer kernel for (a) trained data, and (b) tested data

5.5. Summary

This chapter presents the development of a novel and advanced numerical model, using the continuum-based approach with appropriate material properties and geometries, simulating the interaction of vibratory drum and soil beneath. More than a thousand 3D numerical models were adopted covering various field conditions. Then the newly proposed X-SVR machine learning method was employed to train the inverse solver, simulating the stiffness of the underlying soil by adopting drum acceleration records. The numerical predictions indicated that the eccentric force amplitude as well as frequency, greatly impacted the soil surface settlement right below the drum. In addition, the proposed machine learning approach is promising for real-time extraction of actual soil stiffness during compaction.

The newly proposed generalised Gegenbauer was implemented herein as the kernel for the X-SVR method to train and test the experimental data using the acceleration response of the drum and basic roller properties. Both training and testing underlying stiffness captured from the X-SVR method correlated well with the numerical predictions and the average computation time of each numerical modelling case with the kernelised X-SVR algorithm function was 0.2 s. It is evident that the inverse solver developed in this study could accurately predict the soil stiffness utilising the novel kernel-based X-SVR machine learning, which makes the developed model suitable for real-time quality control by practicing engineers on-site.

Chapter 6

Double-Layered Granular Soil Modulus Extraction for Intelligent Compaction Using Extended Support Vector Regression for Machine Learning Considering Soil-Structure Interaction

6.1. General

This chapter adopts a double-layered soil profile, and a 3D FEM, accounting for soil-drum interaction, is utilised for the analysis. The isotropic hardening elastoplastic hysteretic model was implemented to simulate the soil behaviour subjected to cyclic loading ranging from small to large strain amplitudes and account for stiffness degradation. The comprehensive dataset composed of the roller acceleration response

and ground characteristics is then used to correlate the predicted soil modulus via advanced machine learning approach.

The adopted machine learning method incorporating Gaussian kernel and GGK functions can reasonably predict the double-layered soil modulus during roller compaction. Additional analyses were conducted to observe the proper training size and number of iterations to achieve real-time quality control to be used by site engineers. Furthermore, the influences of the relative modulus ratio, drum lengths and top layer modulus on the soil surface dynamic displacement are discussed.

6.2. Introduction

Applying IC to pavement construction has recently acquired a growing interest, showcasing the benefit of technological improvements for mechanistic pavement design (Nazarian et al., 2020). Indeed, roller compaction is a significant procedure in construction projects, and a well-compacted multi-layered pavement structure is required to provide a stable foundation and distribute the dynamic vehicular loads from the trains or vehicles to the ground while minimising surface deformation. The loading conditions of the vibratory roller for the compaction depend on the frequency and amplitude of the rotating eccentric mass (Wersäll et al., 2020; Sandström, 1994). The induced cyclic load generates cyclic shear stresses, which in turn reduce the pore space between the soil particles and rearrange them into a denser state. Then, the reduced void ratio as a result of the roller compaction process results in enhancing pavement bearing capacity and pavement longevity.

The key parameters of compacted soil for pavement design are soil shear strength and stiffness (Bai and Bai, 2005), and they play a critical role in certifying the

satisfactory subgrade quality and long-term pavement performance. Compliance with the multi-layered compaction quality is a crucial issue of great interest to geotechnical engineers (Wang et al., 2021; Ma and Shi, 2022). While various issues related to pavement compaction have been discussed extensively in the past, several rather recent studies mainly focused on the application of new technologies and the characteristics of the compacted materials (Hu et al., 2019; Hu et al., 2017; He and Zhou, 2022), while better taking cognisance of the dynamic mechanical response of the vibratory roller problems for multi-layered soil is vital (Wang et al., 2021).

The eccentric force (F_{EF}) applied in the dynamic compaction can immediately impact the compaction effort and soil stiffness (Nazarian et al., 2020; Xu et al., 2022b). Equation (6-1) is employed to reflect the magnitude of the eccentric force, indicating the eccentric mass moment ($m_e e_e$) and roller vibration frequency (f) can directly impacts the value of eccentric force. According to Wang et al. (2021), the governing equations of the plane-strain elastic problem in the frequency domain for a two-dimensional multi-layered pavement system could be expressed as in Equation (6.2):

$$F_{EF} = m_e e_e (2\pi f)^2 \cos(2\pi f t) \tag{6.1}$$

$$\begin{cases} \gamma_{xz}(x,z,f) = \dfrac{1}{G}\tau_{xz}(x,z,f) \\ \varepsilon_z(x,z,f) = \dfrac{1-v^2}{E}\left(\sigma_z(x,z,f) - \dfrac{v}{1-v}\sigma_x(x,z,f)\right) \\ \varepsilon_x(x,z,f) = \dfrac{1-v^2}{E}\left(\sigma_x(x,z,f) - \dfrac{v}{1-v}\sigma_z(x,z,f)\right) \end{cases} \tag{6.2}$$

where $m_e e_e$, f and t are the eccentric mass moment, vibration roller frequency, and dynamic time, respectively, x and z are the positive directions of the observation point along the surface and pavement depth, respectively, G, v, and E are shear

modulus, Poisson's ratio and Young's elastic modulus of the compacted geomaterial, separately, σ_x, σ_z, ε_x, and ε_z are normal stress and normal strain along the x-axis and z-axis, separately, and τ_{xz} is the shear strain in the $x - z$ plane.

In recent studies, two-dimensional continuum-based finite element models have been used more frequently to capture the complex geometries, boundary conditions and nonlinear interaction between the vibratory drum and soil strata (Mooney and Facas, 2013). It should be noted that simulation time for 2D modelling is shorter, motivating more researchers to use that for compaction simulation. Kenneally et al. (2015) used ABAQUS to build a dynamic 2D linear elastic FE model, which showed that the interaction between soil and drum is significantly dependent upon the dissipative and inertial properties of the compacted soil.

When the cyclic loading problems are simulated via the three-dimensional (3D) model, the execution time can be excessive, but more accurate predictions can be achieved considering more realistic geometries and boundary conditions (Fathi et al., 2022). Xu et al. (2022a) utilised the 3D numerical model to capture the variation of soil modulus and damping with cyclic shear strain as well as the cumulative plastic deformation during cyclic loading. They reported that adopting a nonlinear elastic-plastic soil model can accurately capture the interaction between soil and drum during compaction, while as a simplifying assumption only a single layer of soil was simulated below the drum.

On the other hand, the demand for real-time quality control compaction is increasing, particularly for infrastructure projects. Hence, establishing a robust and rapid approach to determine the soil characteristics during the compaction process using

emerging techniques such as ML is of great interest to practicing engineers. Zhang et al. (2021) adopted the SVM to characterise the correlation between the CMV and non-nuclear gauge density measurements. In their work, by selecting 80% of training data and 20% of testing data, the in-situ density under different conditions could be predicted with reasonable accuracy with the R^2 equal to 0.85 and 0.76, separately.

In addition, Wang et al. (2022b) established an ANN based approach with the error backpropagation algorithm to estimate the compacted soil modulus and the shear strength. The developed datasets applied for predicting included 4,000 data points of shear strength from open literature, as well as 246 laboratory testing data, while a good correlation between the predicted shear strength and the actual values were observed with an R^2 greater than 0.9.

This study implemented an isotropic hardening elastoplastic hysteretic model, namely the HS-Small model, to simulate the granular soil response subjected to cyclic loading ranging from small to large strain amplitudes and accounts for stiffness degradation. Approximately 3,000 sets of 3D numerical simulations covered a wide range of frequencies, amplitudes, weights, lift thicknesses and various states of granular soils, which were adopted in conjunction with X-SVR to establish a robust and accurate method for predicting the real-time unloading-reloading modulus of the double-layered compacted soil during compaction.

Moreover, a detailed study on the impacts of data size and number of calculation iterations on the computational time is presented in an attempt to determine optimum settings required for machine learning for the back-calculation of soil modulus to minimise the calculation time, allowing the real-time feedbacks of the soil modulus

when vibratory roller is used for compaction. Furthermore, to better understand the vibration response of the roller, the impacts of the soil stiffness ratio, drum length as well as top soil layer stiffness were investigated.

6.3. Details of Finite Element Model

6.3.1. Overview of the Three-Dimensional Model

Accurate consideration of soil nonlinearity under dynamic loading is of critical importance in most geotechnical engineering problems, especially for soil-drum system analysis (Von Quintus, 2010). Since basic viscoelastic or elastic constitutive models are incapable of expressing the progressive and plastic soil deformations, it is significant to employ the proper constitutive models capturing the large strain (e.g., irrecoverable deformation) and small strain (e.g., hysteretic damping) responses of the soil subjected to cyclic loading.

By employing appropriate soil-drum boundary conditions and interface modelling, continuum-based numerical predictions can be used to predict the permanent soil deformations and capture variations of soil damping and modulus with shear strain during compaction (Brinkgreve et al., 2010a; Nazarian et al., 2020; Xu et al., 2022b).

This study utilised a typical earthwork vibratory roller compactor with the drum radius of 0.75 m and the drum length of 2.0 m. The adopted dimensions of the model were assembled to simulate the common drum types employed in Australia for construction works in plenty of infrastructure programs. In addition, the drum is independent from the compactor frame by the equipped low stiffness rubber, leading to the influences of the dynamic frame being insignificant and thus neglected in the

analysis same as in previous studies (Kenneally et al., 2015; Herrera et al., 2018; Xu et al., 2022a).

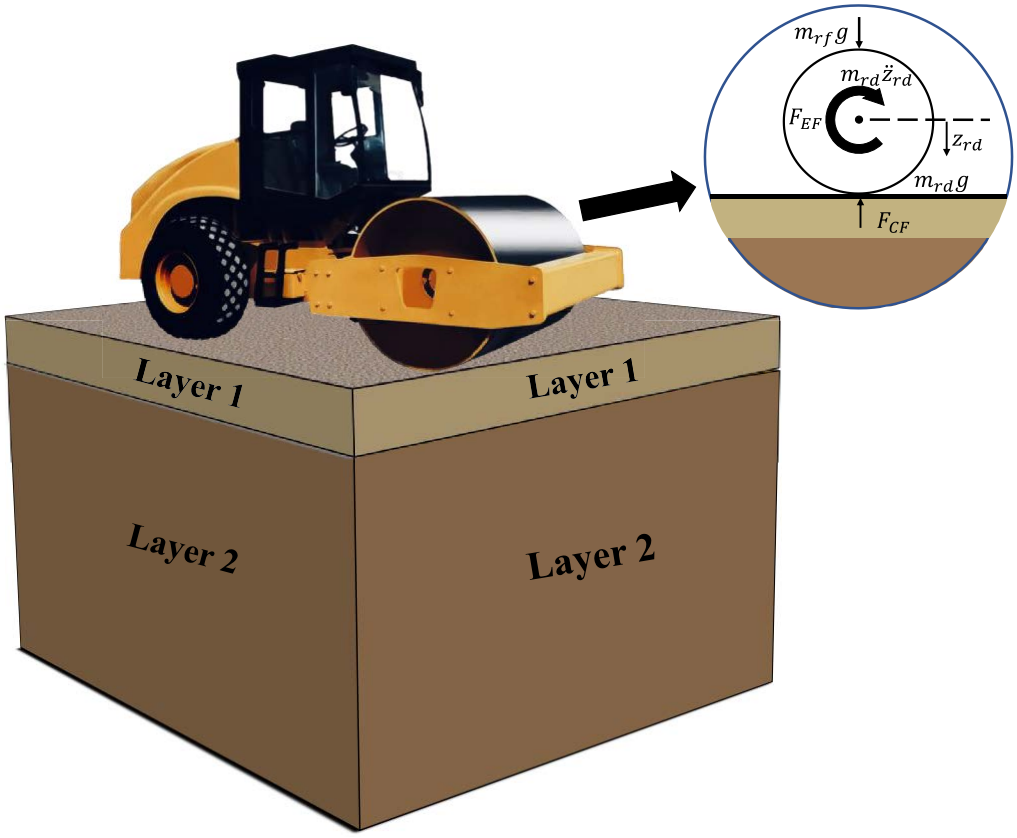

Figure 0.1 The 3D sketch of the interaction between drum and soil strata

Moreover, the weight of the rollers was nominally in the range of 5 to 15 tonnes to investigate the reaction of compacted soil beneath, which covers a wide range of rollers with different weights. In addition, the maximum velocity of the moving roller was considered to be 5.4 km/h, and it is far lower than the corresponding applied frequency or vibration speed of the drum, and thus effects were neglected in this study (Wang et al., 2021). In other words, the drum was assumed to be vibrating in the vertical direction at a fixed position on the soil.

Although the complicated dynamic vibration models with numerous components are more accurate in representing the entire system, for the sake of practicality and

simplicity, it is possible to employ a SDOF lumped mass model considering the most important inertial force, which is induced by the vibrating drum (Herrera et al., 2018). Fig. 6.1 exhibits the sketch of 3D roller of interaction between drum and soil strata, while the centrifugal force (F_{EF}) of drum can be adjusted automatically according to the magnitude of the contact force (F_{CF}) between the soil and drum. Adopting a spring-mass-dashpot vibration system, the expressions employed to represent the dynamic behaviour of soil compaction can be written as:

$$F_{CF} = F_{EF} + m_{rd}g + m_{rf}g - m_{rd}a_{rd} \tag{6.3}$$

where a_{rd} is the drum acceleration, m_{rf} and m_{rd} are masses of the roller frame and the roller drum, respectively.

6.3.2. Modelling of Roller

In this study, PLAXIS 3D (Brinkgreve et al., 2016) as an advanced FE program was applied to simulate the 3D drum-soil interaction problem for propagating waves in the time domain. The model is carried out concerning SDOF drum vibrated at the double-layered soil deposit with the lift thickness of the top layer ranging from 0.15 m to 0.5 m, while it is capable of investigating the nonlinear interaction between drum and soil. The drum was simulated as a rigid and smooth body using a solid element for computational efficiency, similar to other research studies (Nazarian et al., 2020; Kenneally et al., 2015).

Various loading conditions can be combined by the different eccentric mass configurations, frequency and eccentricity, which can directly impact the productivity of roller (Sandström, 1994). Therefore, to enclose an extensive loading

conditions, the frequency was considered changing from 15 Hz to 35 Hz, and the eccentric mass moment $m_e e_e$ varied between 2 kg.m and 6 kg.m incrementally. The different values of $m_e e_e$ together with different rotation frequencies, resulted in a wide practical range of F_{EF} (refer to Equation (6.3)). Additionally, the centrifugal forces were applied to the drum to estimate the dynamic response prompted by the rotating eccentric mass (Xu et al., 2022b).

6.3.3. Modelling of the Double-Layered Soil Strata

The mechanical response of soils subjected to vibrating roller action varies from small to large cyclic deformations. Many previous studies exhibited high stiffness and reversible behaviour for very small-strains which are less than 10^{-5} with a constant shear modulus (Viggiani and Atkinson, 1995; Bard, 1993). Thus, an isotropic hardening elastoplastic hysteretic model (HS-Small) was implemented to examine the nonlinear soil response under a cyclic loading, suitable for diverse strain range from small to large strain amplitudes, while accounting for stiffness degradation with shear strain (Benz et al., 2009).

The HS-Small model combines isotropic plasticity hardening for larger strain levels, and the modulus decay and hysteretic damping of the soils at small strain levels (Lanzano et al., 2016; Benz et al., 2009; Fatahi et al., 2020). The decay of small-strain soil modulus in the model is associated with the surface forces and loss of inter-particle forces within the soil skeleton (Jin et al., 2019). When the loading direction is reversed, the stiffness recovers to the maximum recoverable value that has the same order as the original soil stiffness, and the stiffness then starts to decline once more, while the applied loading is kept going in the reversed direction.

Since the model can record the deviatoric strain history γ_{HIST}, which can be projected onto the actual loading direction (Benz et al., 2009). Thus, the actual shear stiffness can be represented via the following equations incorporating the modified Hardin and Drnevich (1972) model:

$$G_s = \frac{G_0}{1 + \frac{\alpha\gamma_{HIST}}{\gamma_{0.7}}} \tag{6.4}$$

$$G_0 = G_0^{ref}\left(\frac{c\,cos\varphi\ - sin\varphi\sigma_3}{c\,cos\varphi\ + sin\varphi\,p^{ref}}\right)^m \tag{6.5}$$

where G_0 and G_s correspond to the initial shear modulus and the secant shear modulus at very small strain, respectively, m is a dimensionless parameter, denoting the power for the stress-level dependency of stiffness, and σ_3 is the minor principal stress. Moreover, $\gamma_{0.7}$ is the shear strain at which $G_s = 0.722G_0$ to describe the shape of the G_s - γ_{HIST} relationship; referring to Dos Santos and Correia (2001), the recommended value of α = 0.385 is adopted in this study.

Furthermore, G_0^{ref} is the shear stiffness related to the reference pressure p^{ref} (= 100 kPa in this study). Additionally, Benz et al. (2009) proposed the following equations for the scalar valued shear strain γ_{HIST}:

$$\gamma_{HIST} = \sqrt{3}\frac{\|\mathbf{H}\,\Delta\underline{e}\|}{\|\Delta\underline{e}\|} \tag{6.6}$$

where **H** is the symmetric tensor utilised to show the material's deviatoric strain history, and $\Delta\underline{e}$ represents the actual deviatoric strain increment. For the model parameter determination, the scalar values of shear strain $\gamma = \gamma_{HIST}$ are applied. In addition, the tangent shear stiffness modulus (G_t) can be derived from Equation (6.7)

concerning the shear strain, while it is limited by the lower cut-off value $\gamma_{\text{cut-off}}$ related to the unloading-reloading shear stiffness modulus G_{ur} which is given as Equation (6.8).

$$G_t = \frac{G_0}{\left(1 + 0.385\frac{\gamma}{\gamma_{0.7}}\right)^2} \geq G_{ur} = \frac{E_{ur}}{2(1 + v_{ur})} \tag{6.7}$$

$$\gamma_{\text{cut-off}} = \frac{\gamma_{0.7}}{0.385}\left(\sqrt{\frac{G_0}{G_{ur}}} - 1\right) \tag{6.8}$$

It should be noted that there are three key soil stiffness parameters in the HS-Small model utilised in the study, which are: E_{50} (the secant stiffness modulus), E_{oed} (one-dimensional tangent modulus) and E_{ur} (unloading-reloading stress-dependent modulus), and they are explained in Chapter 2, Section 2.5.3.

For a detailed explanation of each input parameter, please refer to Section 4.3.2. Furthermore, the HS-Small model formulations adopted the hyperbolic function to relate the vertical strain (ε_1) to the deviatoric stress (q) as shown in Equation (6.9).

$$-\varepsilon_1 = \frac{1}{E_1}\frac{q}{1 - \frac{q}{q_a}} \; for \; q < q_f \; = (c \; cot \; \varphi - \sigma_3')\frac{2 \; sin \; \varphi}{1 - sin \; \varphi} \tag{6.9}$$

where q_a is the shear strength related to asymptotic value, q is the current shear stress, and q_f is the ultimate deviatoric stress.

This study used double-layered soil, adopting the HS-Small model for both layers. The primary motivation for the model is to consider a wide range of soil properties from loose to dense state, while various relative density from RD = 30% to RD = 80% were separately utilised for both layers.

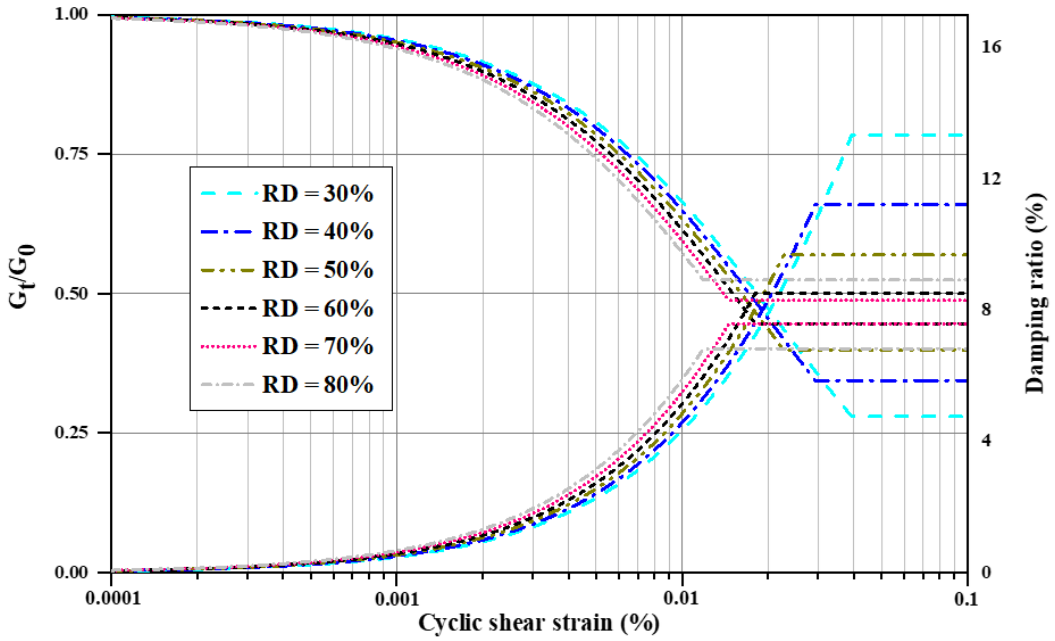

Figure 0.2 Damping ratio curves and tangent shear modulus degradation curves for various relative densities (RDs)

Figure 6.2 shows the backbone curves, capturing variation of the shear modulus and the damping ratio with cyclic shear strain amplitude. The implicit nonlinear time-integration was implemented for the dynamic analysis in numerical modelling for accurate predictions as well as the stable computing process (Sluys, 1994) which can be expressed based on the Newmark method as in Equation (6.10).

$$u^{t+\Delta t} = \Delta t^2 \left(\left(\frac{1}{2} - \alpha_i \right) \ddot{u}^t + \alpha_i \ddot{u}^{t+\Delta t} \right) + \dot{u}^t \Delta t + u^t \tag{6.10a}$$

$$\dot{u}^{t+\Delta t} = \Delta t \left((1 - \beta_i) \ddot{u}^t + \beta_i \ddot{u}^{t+\Delta t} \right) + \dot{u}^t \tag{6.10b}$$

where u, $\dot{u}$, and $\ddot{u}$ are displacement, velocity and acceleration, respectively, Δt is the time step, α_i and β_i are numerical model coefficients ($\alpha_i = 0.25$ and $\beta_i = 0.50$ are employed in this study as in (Noh and Bathe, 2019). Adopting the formulations

developed by Brinkgreve et al. (2010a), Table 6.1 summarised the adopted values of the model parameters related to various RDs of the soil.

Table 0.1 Applied soil characteristics for HS-Small model with the different relative densities (RDs)

Parameter	RD = 30%	RD = 40%	RD = 50%	RD = 60%	RD = 70%	RD = 80%
$\gamma\ (kN/m^3)$	16.2	16.6	17	17.4	17.8	18.2
$E_{50}^{ref}(kPa)$	18,000	24,000	30,000	36,000	42,000	48,000
$E_{oed}^{ref}(kPa)$	18,000	24,000	30,000	36,000	42,000	48,000
$E_{ur}^{ref}(kPa)$	54,000	72,000	90,000	108,000	126,000	144,000
$G_0^{ref}(kPa)$	80,400	87,200	94,000	100,800	107,600	114,400
m	0.6063	0.5750	0.5438	0.5125	0.4813	0.4500
$\gamma_{0.7}$	1.7E-04	1.6E-04	1.5E-04	1.4E-04	1.3E-04	1.2E-04
φ' (degree)	31.75	33	34.25	35.5	36.75	38
ψ (degree)	1.75	3	4.25	5.5	6.75	8
R_f	0.963	0.950	0.938	0.925	0.913	0.900

6.3.4. Geometrical Characteristics of the Double-Layered Soil Model

Figure 6.3 examines the 3D model of the drum on the double-layered soil strata by simulating the roller-soil interaction to obtain the acceleration of vibrating drum. The gravity load was applied to the rigid drum to model the self-weight of roller, and the value of the dynamic vertical vibrating load was adjusted by changing the eccentric force as in Equation (6.3). The horizontal forces were counteracted as a result of the

counter eccentric masses rotating around drum's longitudinal axis, and thus no horizontal force was applied during the dynamic analysis (Van Susante and Mooney, 2008).

The double-layered soil strata model was simulated employing around 70,000, 10-node tetrahedral elements (Figure 6.3(a), for 500 mm lift thickness of the top layer), which provides a second-order interpolation of displacements. The lift thickness of the compacted layer is a significant factor influencing the quality of compaction during construction (Roberts et al., 1991; Kenneally et al., 2015). Although, the typical lift thickness of the layer changes from 150 to 300 mm (Mooney and Ma, 2009), to ensure the predicted dataset can systematically and valuably cover extensive cases with different conditions, the range of thickness varying between 150 and 500 mm was employed in this chapter. Kenneally et al. (2015) used the maximum thickness of the base layer as 550 mm for compaction. Mooney and Facas (2013) investigated the impacts of the different depths of overlying bases up to 500 mm in field measurement.

In addition, the width and length of the block were kept constant at 10 m, and the depth of the bottom layer soil was 10 m, which is capable of minimising the impacts of boundaries and for the sake of accuracy. The effective depth of the corresponding roller was estimated up to 1.2 m (Mooney and Facas, 2013), and thus the simulation depth was sufficient. The loading sequence was divided into four different stages, including (i) the initial equilibrium of the double-layered soil strata, (ii) application of the roller mass, (iii) application of cyclic loading to simulate the drum vibration, and (iv) equilibrium after completion of vibration and removing the drum simulating post-compaction state.

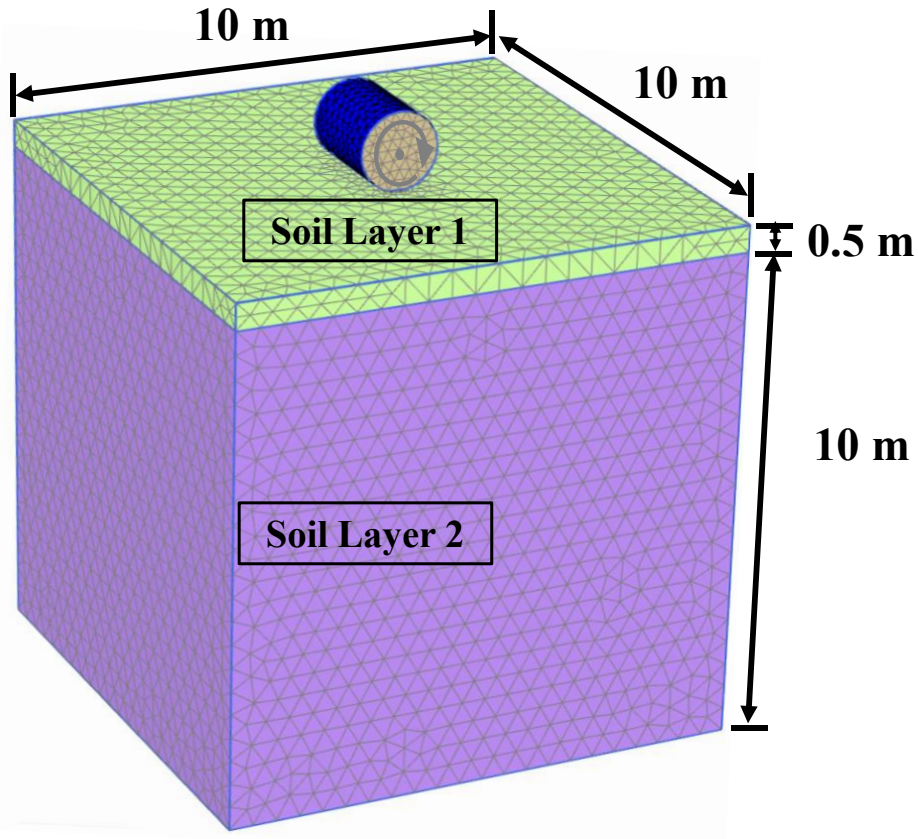

(a)

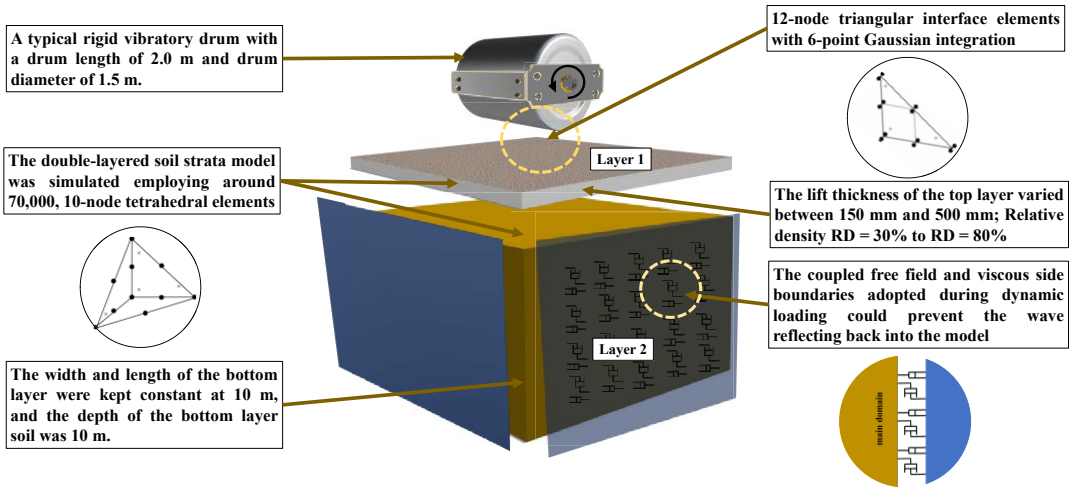

(b)

Figure 0.3 Adopted double-layered (a) three-dimensional numerical model in Plaxis 3D, and (b) the sketch of the soil-drum system

6.3.5. Interface Modelling and Boundary Conditions

To accurately model the soil-drum interaction in numerical modelling of the double-layered soil strata, appropriate interfaces to simulate stress transfer between the roller and soil is required. Referring to Figure 6.3(b), the 12-node elements with 6-point Gauss integration scheme were adopted for interface simulation. Each node had three translational degrees of freedom with a pair of two nodes with zero distance, which resulted in the allowance for differential displacements between the node pairs on interface elements as a result of gapping or slipping.

The linear elastic-plastic constitutive model was utilised to simulate the interface behaviour. In this chapter, the Mohr-Coulomb criterion was applied to distinguish between plastic interface behaviour, where a permanent slip could occur, and elastic behaviour, when small displacements may exist within the interface (Brinkgreve et al., 2016). For soil experiences plastic and elastic deformation, the shear stress, τ, can be defined as:

For Elastic-Plastic deformations: $|\tau| = -\sigma_n \, c_i \, tan(\varphi_i)$ (6.11)

For Elastic only deformation: $|\tau| < -\sigma_n \, c_i \, tan(\varphi_i)$ (6.12)

where σ_n is the effective normal stress, φ_i and c_i are the friction angle and the cohesion of the interface, separately.

In addition, the interface strength properties are associated with the soil layer strength properties. The properties of the interface can be calculated based on the relevant soil properties, which are modified using interface reduction factor R_{inter}:

$$tan(\varphi_i) = tan(\varphi_{soil})\, R_{inter} \leq tan(\varphi_{soil}) \tag{6.13}$$

$$c_i = c_{soil} R_{inter} \tag{6.14}$$

$$\psi_i = 0 \; for \; R_{inter} < 1, otherwise \; \psi_i = \psi_{soil} \tag{6.15}$$

where ψ_i and ψ_{soil} are initial dilatancy angle, and soil dilatancy angle, respectively, and φ_{soil} denotes the failure-peak value of φ in HS-Small model. In line with several previous studies (Xu et al., 2022a; Mccabe and Sheil, 2015; Skels and Bondars, 2017), R_{inter} = 1 was adopted in this study, and separation was allowed between the vibrating drum and the soil surface without any resistance by adopting a zero tension limit.

Two groups of boundary conditions were adopted separately during static and dynamic conditions. A fully fixed boundary condition in all directions was utilised at the bottom of the model while lateral displacements were restricted on the four side boundaries during gravity loading. The coupled free field and viscous side boundaries were adopted during dynamic loading which could prevent the waves reflecting back into the model (Fatahi et al., 2020). Equations (6.16) and (6.17) capture utilised extra tractions on the boundaries allowing a free-field boundary (not reflective):

$$\tau_s = -\rho C_2 V_s (\dot{u}_y^m - \dot{u}_y^{ff}) \tag{6.16}$$

$$\sigma_n = -\rho C_1 V_p (\dot{u}_x^m - \dot{u}_x^{ff}) \tag{6.17}$$

where τ_s and σ_n are the shear and normal stresses, respectively, V_s and V_p are the shear wave velocity and the compressive wave velocity, ρ is the density of material, C_1 and C_2 are the relaxation coefficients to enhance the influences of absorption, and

it should be noted the relaxation is redundant ($C_1 = C_2 = 1$) when the pressure waves perpendicularly strike the boundary (Lysmer and Kuhlemeyer, 1969). $\dot{u}^{ff}$ and $\dot{u}^{m}$ are the soil particle velocities in the free-field and main element, respectively. Furthermore, a viscous boundary with a damper was employed during dynamic analysis as recommended by Herrera et al. (2018) and Kenneally et al. (2015) at the bottom boundary to avoid crossing wave bouncing back to simulate a deep soil deposit.

6.4. Results and Discussion

In this study, the results of the X-SVR machine learning incorporating kernel functions were presented to correlate the roller characteristic and soil lift thickness to soil stiffness during roller compaction. In addition, the extra studies were conducted to determine a proper proportion of training and testing data size and the suitable number of iterations to decrease the computation time and develop a rapid and efficient model to extract the soil stiffness in real-time. Moreover, the stiffness ratio of double-layer E_{ur}^{1}/E_{ur}^{2} varied between 0.5 and 2.0, and impacts on drum response were studied, where E_{ur}^{1} is the unloading-reloading soil stiffness of the top layer and E_{ur}^{2} is the unloading-reloading soil stiffness of the underlying soil. Furthermore, to better understand the soil surface displacement, the impacts of drum length as well as top soil layer stiffness were investigated.

6.4.1. Evaluation of the Extended Support Vector Regression method

To examine the reliability of the kernelised X-SVR method, around 3,000 sets of analyses using 3D finite element modellings were generated in this study. Among these extensive datasets, 2,400 sets of randomly selected data were developed to train the ML model, and the remaining 597 groups of data were applied to test the model.

To achieve higher efficiency in predicting the modulus of geomaterials, the GGK and Gaussian kernel functions were separately implemented herein for the newly proposed X-SVR. Using the Gaussian kernel function instead of the square root function for depicting the local information could result in a superior performance (Ozer et al., 2011; Cheng et al., 2017). In addition, according to Wang et al. (2019), as the weighting function of GGK, the developed Gaussian kernel $\kappa\,(\boldsymbol{X}_i, \boldsymbol{X}_j)$ in terms of two arbitrary input $\boldsymbol{x}_i$ and $\boldsymbol{x}_j$ which satisfies the Mercer Theorem and it is defined as:

$$\kappa\,(\boldsymbol{X}_i, \boldsymbol{X}_j) = exp(\gamma \left\| \boldsymbol{X}_i - \boldsymbol{X}_j \right\|_2^2) \tag{6.18}$$

The quality control of the compacted soil is greatly affected by the physical parameters of roller such as amplitude, frequency and other characteristics of roller (Rinehart and Mooney, 2008; Xu and Chang, 2013).

In this chapter, five variables were selected as inputs for ML model, which are (1) the dynamic acceleration time-history response of the drum ($a_{rd} - t$ or $\ddot{z}_{rd}$- t), (2) the excitation force of the roller (F_{EF}), (3) the unloading-reloading stiffness of the underlying layer (i.e. E_{ur}^2) (4) the ratio of roller mass to drum length ($R_{Ml} = M/l$)

and (5) the lift thickness of the top layer (h_{top}). The output of the proposed model was the unloading-reloading modulus of the top layer (i.e. E_{ur}^{1}).

It should be known that the R_{Ml} and the h_{top} are independent which can determine by the site team and manufacturer, and the acceleration response of vibratory drum can be directly captured by the accelerometer attached to the centre of the drum. The excitation force of the roller could be computed using Equation (6.1), which is a function of the drum eccentric mass moment and frequency.

Moreover, the value of unloading-reloading modulus underlying layer (i.e. E_{ur}^{2}) can be determined from proof-rolling as mentioned in Xu et al. (2022b). Therefore, these input variables could be readily captured by engineers and be used in the proposed machine learning model to predict the E_{ur}^{1} of the soil layer immediately below the roller drum for different construction sites and projects. To verify the reliability of the proposed X-SVR algorithm, the $RMSE$, the R^2, and the RE were determined.

Figure 6.4 showed the correlation between the experimental results in machine learning with adopting GGK kernel and the R^2 of training and predicting unloading-reloading modulus, which exhibited a good correlation of 0.999952 and 0.987505, respectively. In addition, the RE of the training and testing data in adopted X-SVR with GGK method were 0.00056% and 0.4260% (Figure 6.5), respectively, figuring out the proposed method exhibited high precision for both training and predicting.

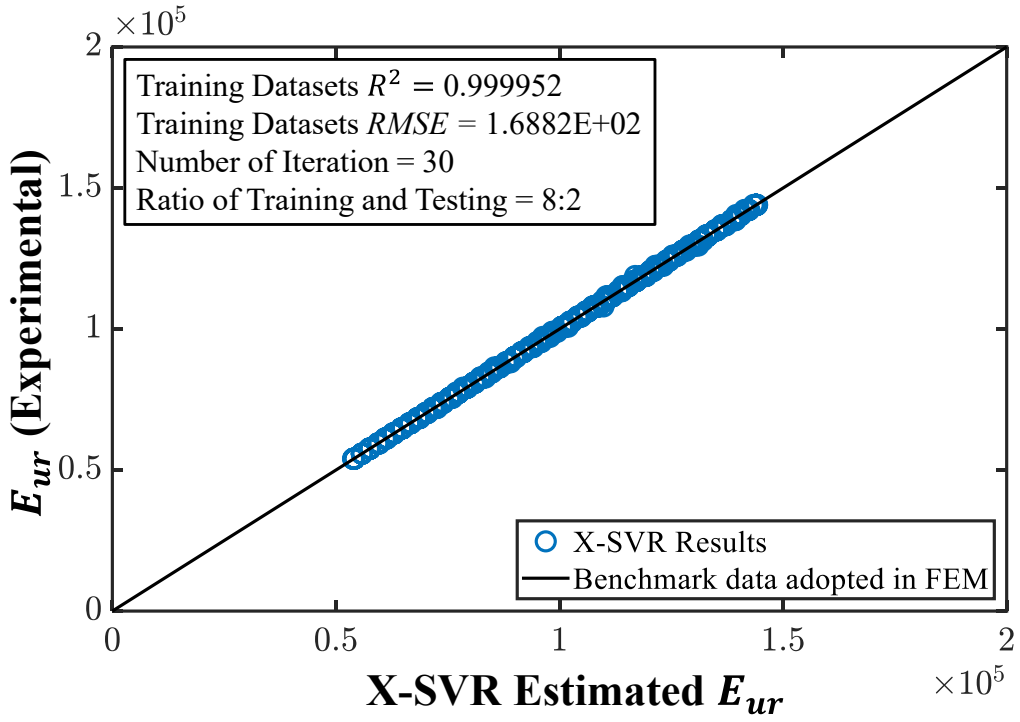

(a)

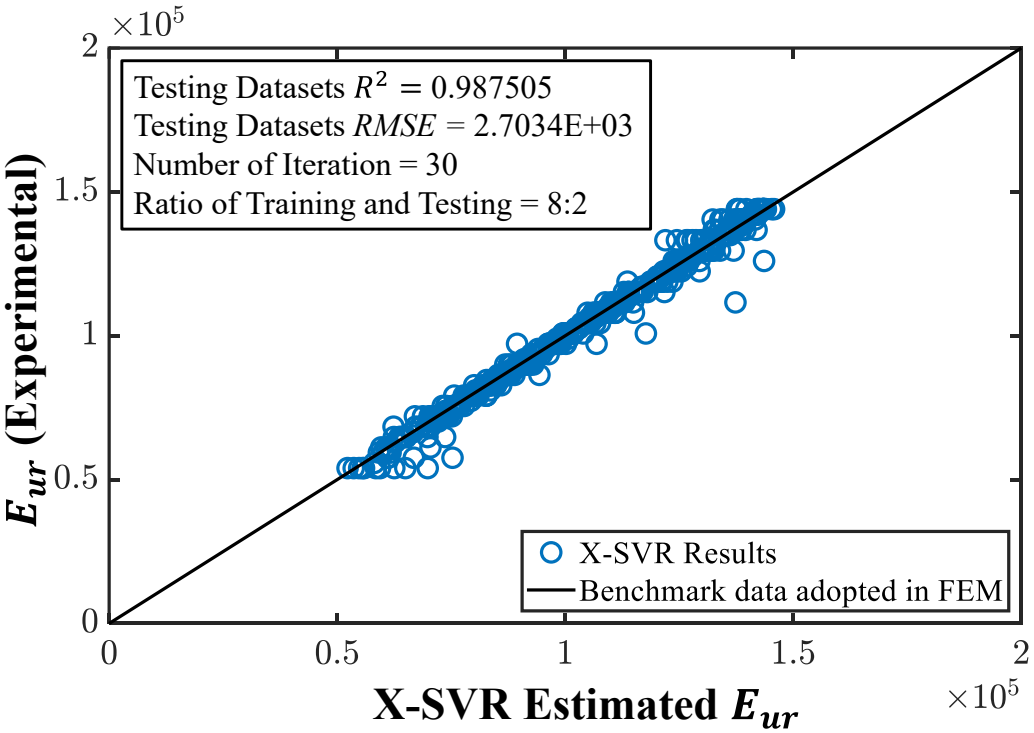

(b)

Figure 0.4 Comparison of double-layered numerical outputs (experiment) by the GGK kernelised X-SVR (a) training datasets, and (b) predicting datasets

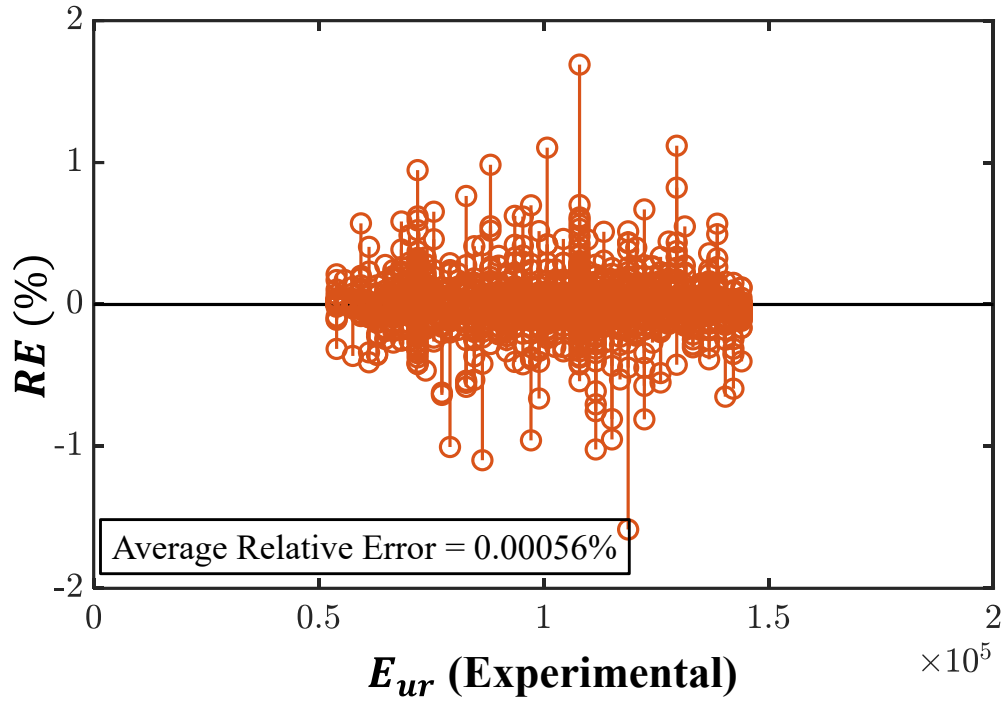

(a)

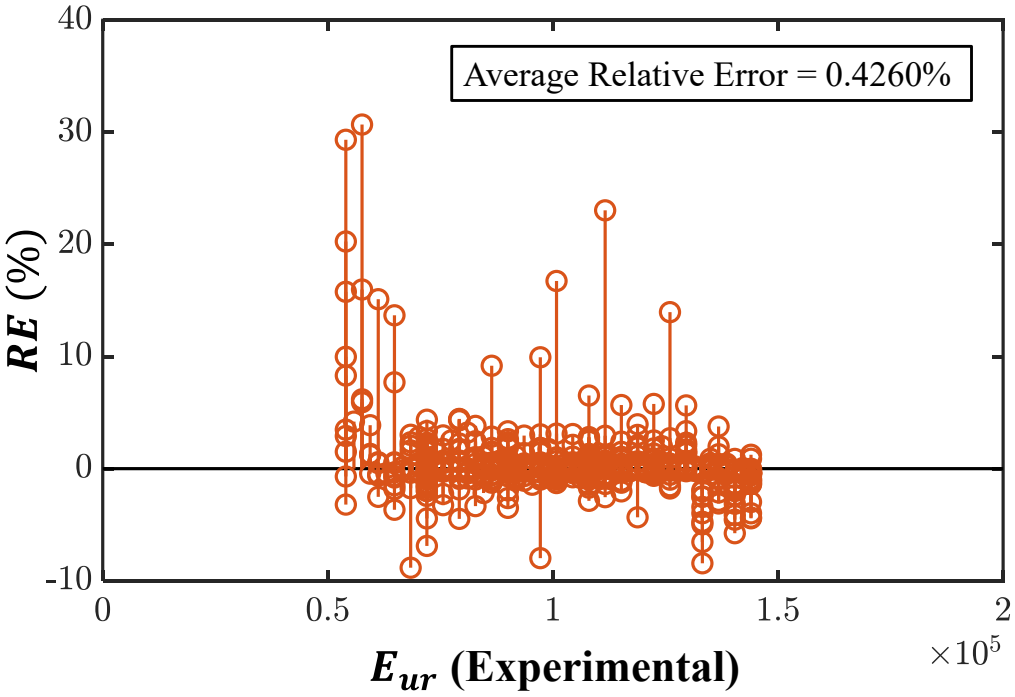

(b)

Figure 0.5 The RE by the GGK kernelised X-SVR approach (a) training datasets, and (b) predicting datasets

It is worth mentioning that the Gaussian kernelised X-SVR function illustrated the good results. Indeed R^2 value of training and predicting unloading-reloading modulus showed a good correlation with values equal to 0.991421 and 0.985122, respectively (refer to Figure 6.6). Furthermore, the average relative errors of training data and predicting data were 0.0542% and 0.1240%, respectively (Figure 6.7).

In addition, the average computation time of X-SVR with Gaussian kernel function was 1.9 sec for each estimation (Intel Core i7-8650U, 1.9 GHz cores and 16 GB RAM). Since the motivation was to develop an efficient method to predict the unloading-reloading modulus of compacted soil rapidly and accurately, the X-SVR with Gaussian kernel function can achieve real-time extraction of compacted soil on site.

To further assess the reliability of the adopted X-SVR with Gaussian kernel, a neural network (NN) method was conducted for the comparison. Identical to the previous investigations, 2400 training samples were utilised for NN technique to simulate the unloading-reloading modulus with the number of neurons in hidden layer is 10. The coefficient of determination of the NN method in terms of training and testing data were presented in Figure 6.8(a) and 6.8(b), respectively. The computational accuracies of the NN for training and experimental testing results corresponded to $R^2_{training}$ = 0.98303 and $R^2_{testing}$ = 0.91594, while the proposed X-SVR with Gaussian kernel function for training and testing unloading-reloading modulus resulted in $R^2_{training}$ = 0.991421 and $R^2_{testing}$ = 0.985122. By comparing the predictions via the X-SVR approach and the NN method, it is evident that the former resulted in more accurate predictions of soil stiffness during compaction.

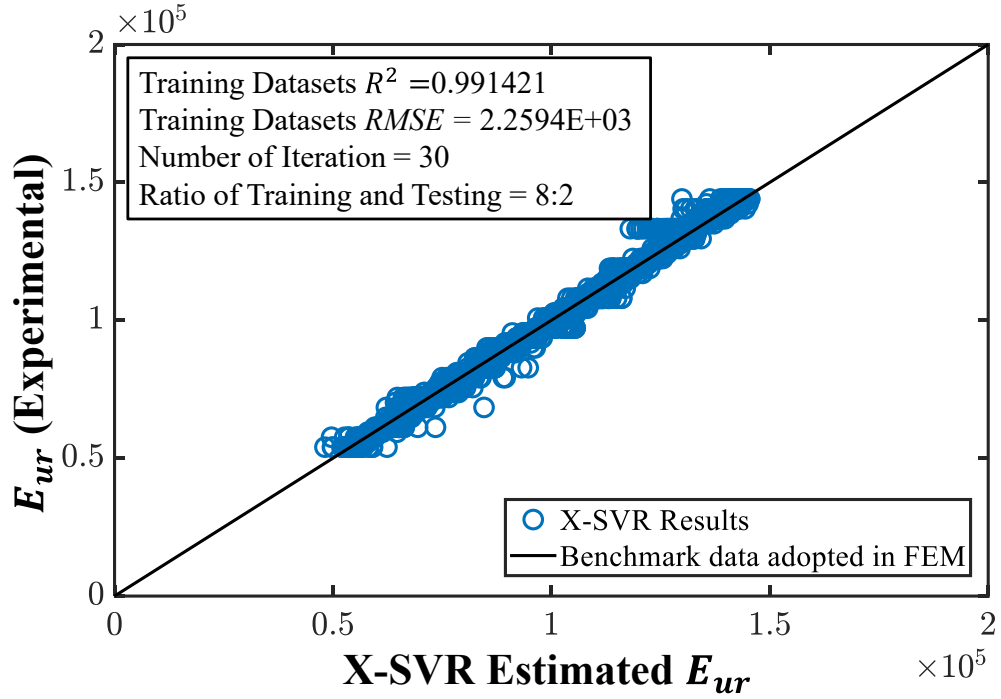

(a)

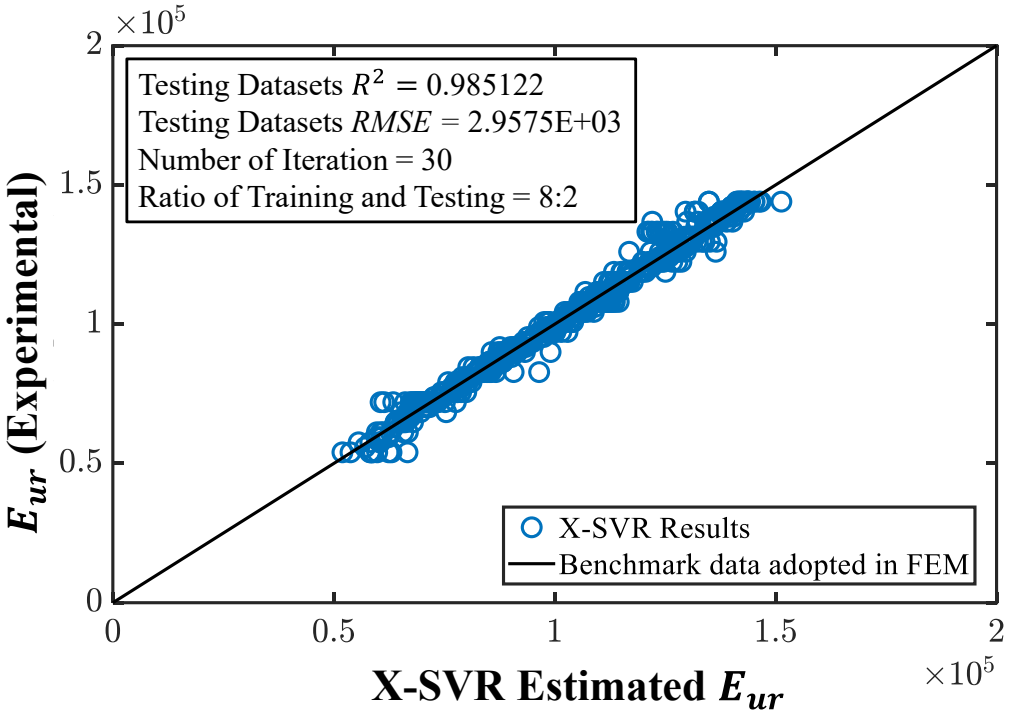

(b)

Figure 0.6 Comparison of double-layered soil numerical modelling outputs (experiment) by the Gaussian kernelised X-SVR (a) training datasets, and (b) predicting datasets

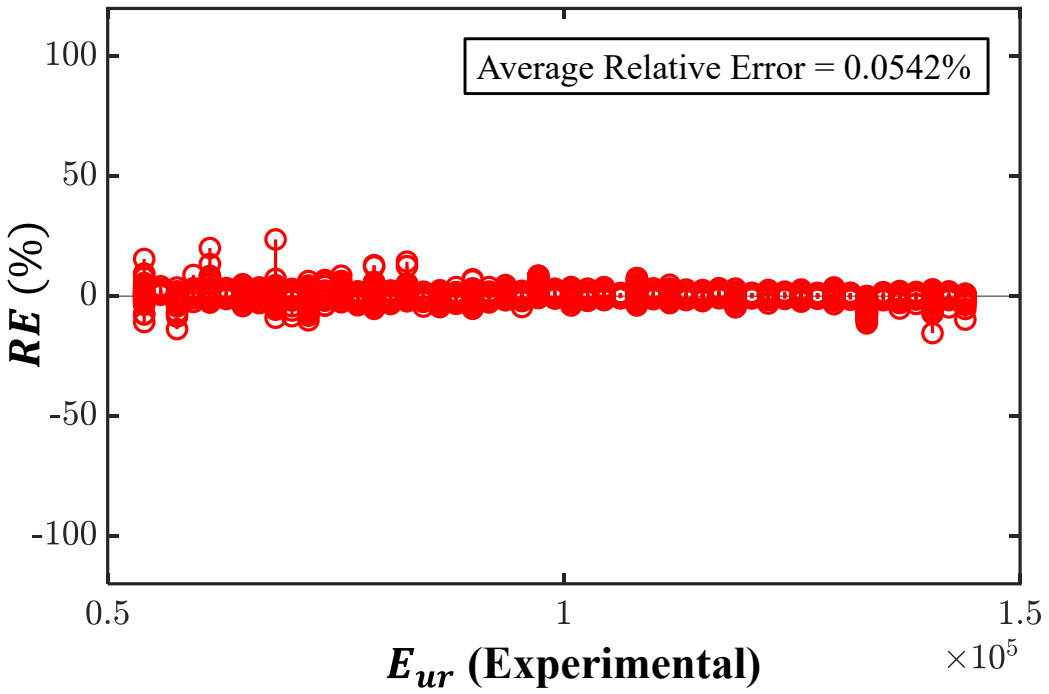

(a)

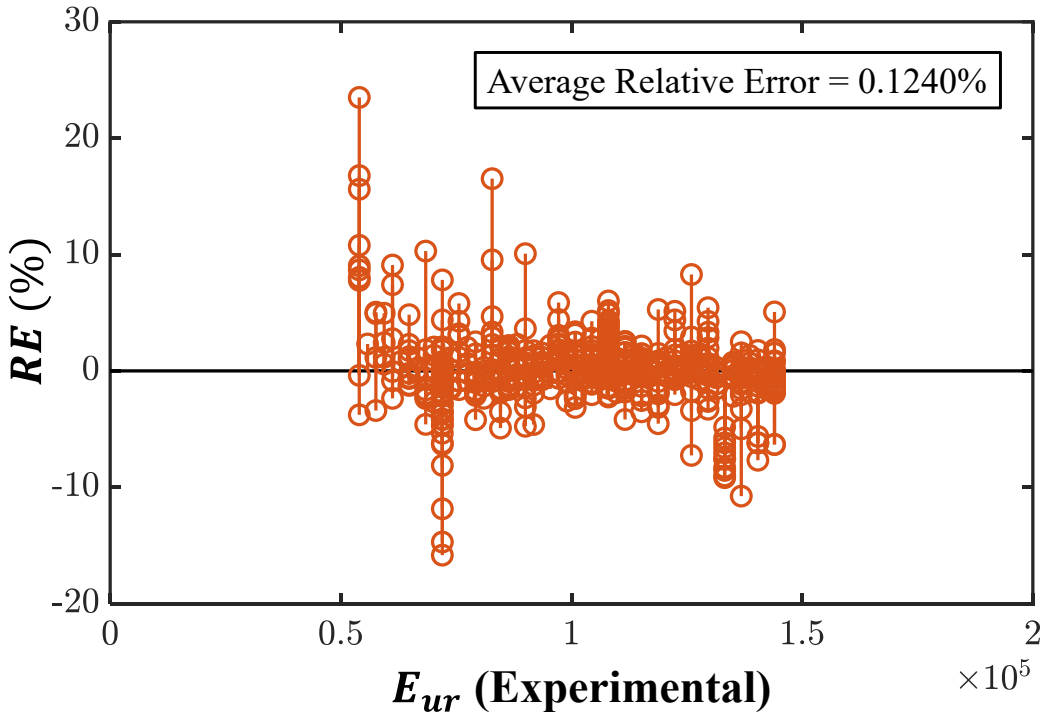

(b)

Figure 0.7 The relative error (RE) by the Gaussian kernelised X-SVR approach (a) training datasets, and (b) predicting datasets

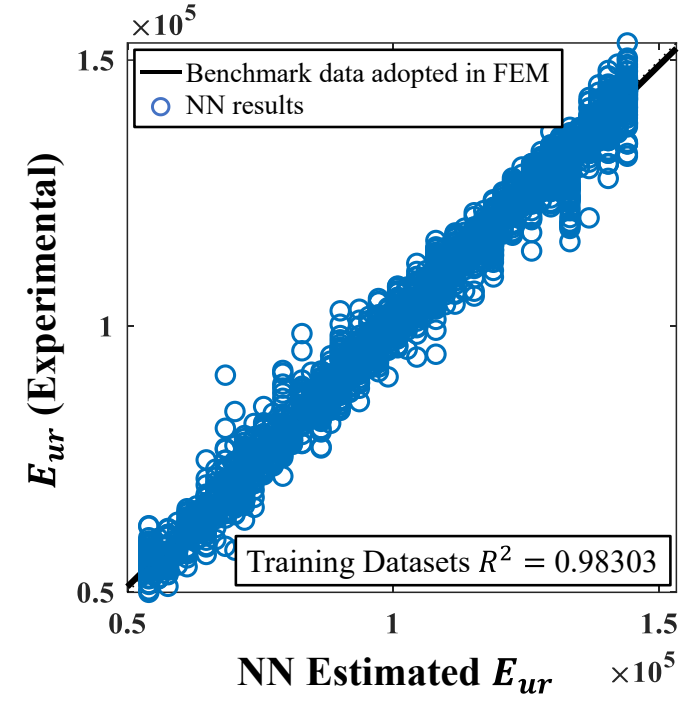

(a)

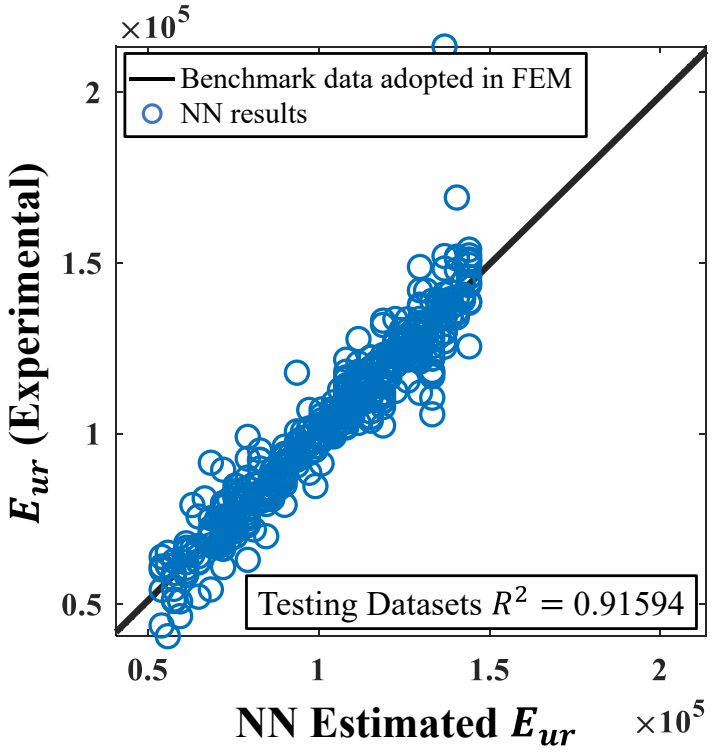

(b)

Figure 0.8 Comparison of two-layer soil numerical modelling outputs (experiment) with Neural Network (NN) results (a) training data, and (b) testing data

It should be noted that the primary limitation of the current intelligent compaction technology is that the predicted soil modulus derived from the vibratory roller, corresponds to an average composite modulus within an effective depth of say 1.2 m (Mooney and Facas, 2013). Compared with the commonly applied thickness of compacted layer ranging from 150-500 mm (Hu et al., 2017; Anderegg and Kaufmann, 2004; Kenneally et al., 2015), the impact depth of a vibratory roller is considerably greater than a single compacted layer.

Thus, it would be highly practical for site engineers to have a tool to determine the properties of compacted pavement with the independent prediction of each layer modulus for QA purposes (Mooney and Facas, 2013). Several investigators in the past have attempted to determine individual soil stiffness values of the composite soil profile. For example, Mooney and Facas (2013) applied the forward approach with finite element modelling and boundary element modelling as well as the real-time inverse analysis to back-calculate the multi-layered soil stiffness from IC roller under the linear elastic constitutive model.

Moreover, Wang et al. (2021) proposed a method to obtain the stiffness matrix for two pavement layers to extract the independent stiffness of double-layered isotropic elastic materials under complete contact between the layers and structure conditions. Although, the aforementioned predicted results demonstrated reasonable agreement with the measured data, they are limited to the simplified constitutive model, which cannot fully capture the dynamic response of the soil. Therefore, a comprehensive study incorporating various factors with advanced machine learning technology is proposed to analyse the roller responses and the quality of compaction.

Evaluation of the degree of compaction is important in real practice to control the compaction quality, and an indication of that can be captured from the dynamic interaction between the vibratory drum and soil (Briaud and Seo, 2003; Van Susante and Mooney, 2008). Nevertheless, the previous correlations between the physical parameters and compacted soil modulus are limited to particular circumstances. Thus, the adopted X-SVR aided the extraction of compacted soil modulus, providing a sampling scheme to represent the statistical analysis (e.g., the standard deviation, the relative error, the root mean square error, the coefficient of determination), as well as predict unloading-reloading modulus based on the roller behaviour.

In addition, the identical size of training datasets could be preset in X-SVR (Wang et al., 2020; Wang et al., 2022a), which can be utilised to determine the proper training size in the field to decrease the operation time and achieve the real-time stiffness calculation with a high accuracy regression model.

6.4.2. Effects of the Distribution of Training and Testing Data on Predictions

The computational time of the machine learning algorithm depends on the proportion of the training and testing data, as well as the number of iterations. Achieving a shorter processing time while having sufficient accuracy is beneficial for site engineers to assess the compaction quality in real-time. Figure 6.9 summarised the influence of different training and predicting data proportions on the model accuracy and the computational time.

Evidently, the R^2 gradually increased as the size of training data for the inverse solver increased, and beyond 60% of training data, insignificant differences were

observed in the coefficient of determination. Even though allocating 60% of the training data for analysis exhibited a sound prediction, the computational time rapidly increased beyond 40% of the training data. As an example, the computational time of the former (i.e. 60% training data) was 3.5 times greater than the latter (i.e. 40% training data).

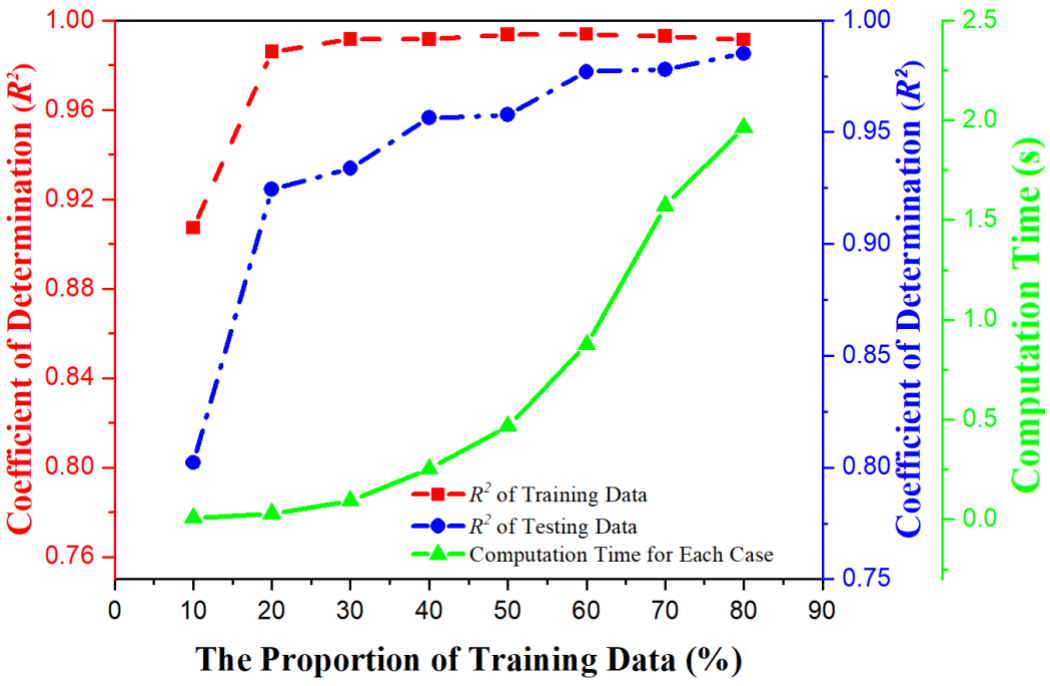

Figure 0.9 R^2 and computation time of Gaussian kernelised X-SVR approach against the proportion of training data

Referring to the results presented in Figure 6.9, the observations suggest that when applying Gaussian kernelised X-SVR to train the predicted model, the proportion of selected training data greater than or equal to 40% is reasonable. Thus, the selection of 40% of data for training was optimum in terms of satisfying both accuracy and minimised computational time.

Figure 6.10 indicated the variation of R^2 for the different number of iterations of predicted and experimental E_{ur} when 40% of training data was selected in the X-

SVR algorithm applying the Gaussian kernel function. The R^2 and computation time were utilised to confirm the acceptable number of iterations. Furthermore, Figure 6.10 demonstrated that when the number of iterations was equal to 25, the testing data correlated well with the actual compacted soil modulus (R^2 = 0.9484) and yielded a rather low RMSE value ($RMSE$ = *5.68E+03*).

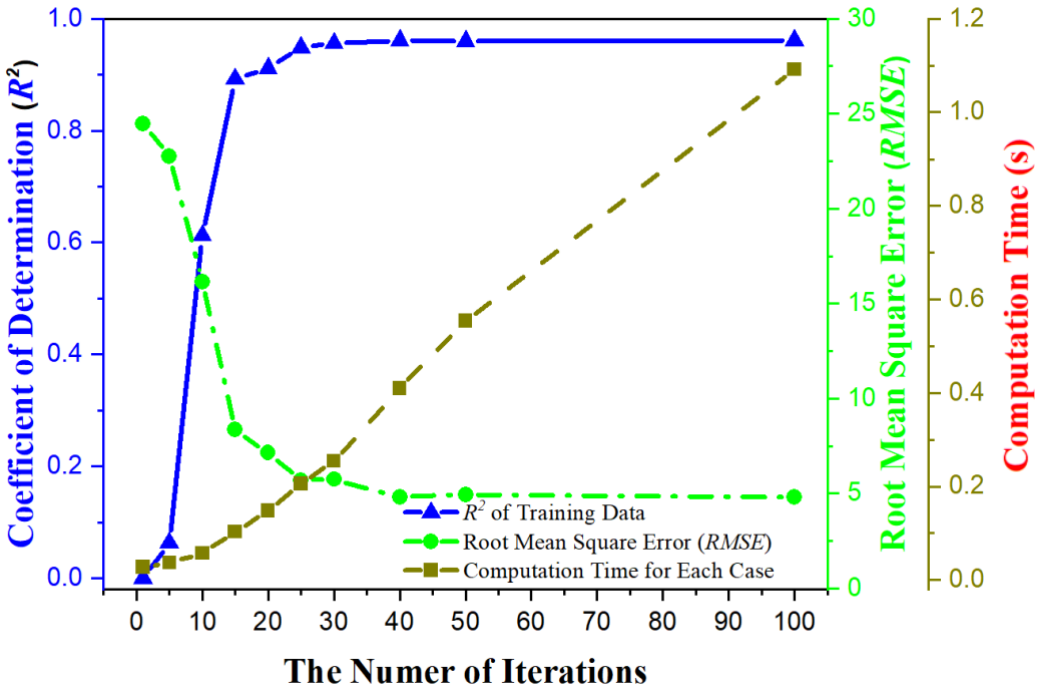

Figure 0.10 Variations of R^2, RMSE and computation time of Gaussian kernelised X-SVR approach verse the number of iterations

6.4.3. Effects of Stiffness Ratio

To evaluate the influences of soil modulus ratio of double-layered soil on vibratory drum response, a parametric study was conducted. For this purpose, a 10,000 kg roller, resting on a soil layer with 500 mm lift thickness was considered, while the unloading-reloading modulus of the underlying layer was selected as 50 MPa, 80 MPa and 110 MPa, and the E_{ur}^1/E_{ur}^2 ratio changed between 0.5 and 2.0 incrementally.

Figure 6.11 exhibited the results of the vertical soil settlement (z_d) versus modulus ratio. The absolute z_d value decreased with E_{ur}^1/E_{ur}^2, which was consistent with Lundberg theory (Lundberg, 1939), while as expected, the soil settlement was inversely proportional to soil modulus.

It should be noted that for a given underlying soil condition (i.e. E_{ur}^2 remaining constant), soil surface settlement z_d became less sensitive to vibration as E_{ur}^1/E_{ur}^2 increased. This finding could be considered by practicing engineers, when compacting the soil with a higher E_{ur}^1/E_{ur}^2 ratio. In addition, a critical modulus line is shown in Figure 6.11, illustrated that the critical modulus ratio decreased with E_{ur}^2 or relatively density of the underlying layer.

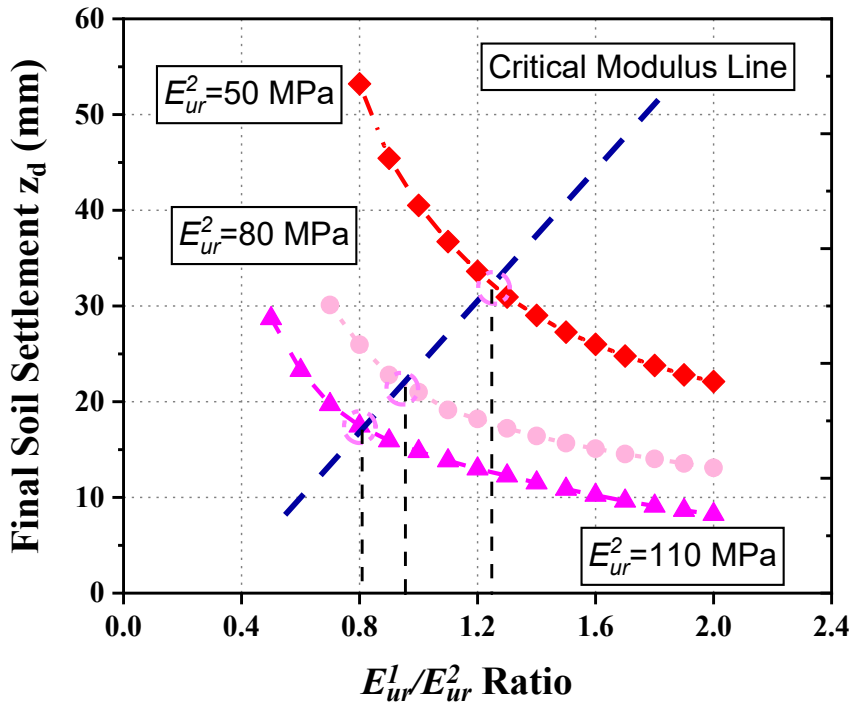

Figure 0.11 Final soil settlement verses modulus ratio for different underlying soil modulus

Referring to Figure 6.11, the critical E_{ur}^1/E_{ur}^2 in the range 0.8 – 1.25 was observed beyond which the variations of the soil settlement was insignificant. These results

can facilitate in selection of data size and number of iterations, which could be employed as a preliminary study to establish a robust and efficient correlation models to extract the compacted soil stiffness and achieve real-time feedback control during the compaction procedure.

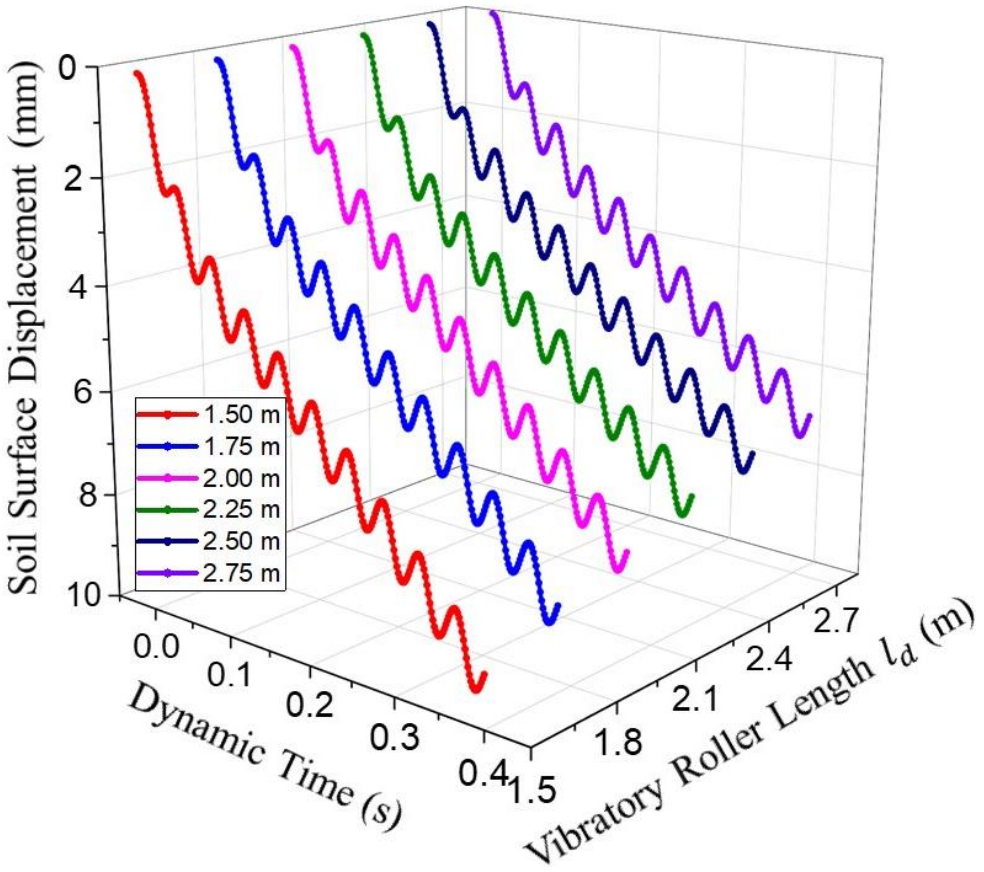

Figure 0.12 The vibratory roller vertical displacement versus different vibratory roller length

In addition, the impacts of the drum length (l_d) on the vertical soil settlement while other roller characteristics were keeping the same were also investigated. To observe the sensitivity of the interaction between drum and soil to l_d, a double-layered drum-soil system was explicitly modeled with E_{ur}^1= 60 MPa, E_{ur}^2 = 110 MPa, and l_d varied from 1.5 m to 2.75 m as reported in Figure 6.12. Soil settlement was accumulated gradually due to cyclic loading with the largest settlement observed when drum

length l_d = 1.5 m. A reduction in the cumulative displacement was observed as a result of a decrease in the roller length.

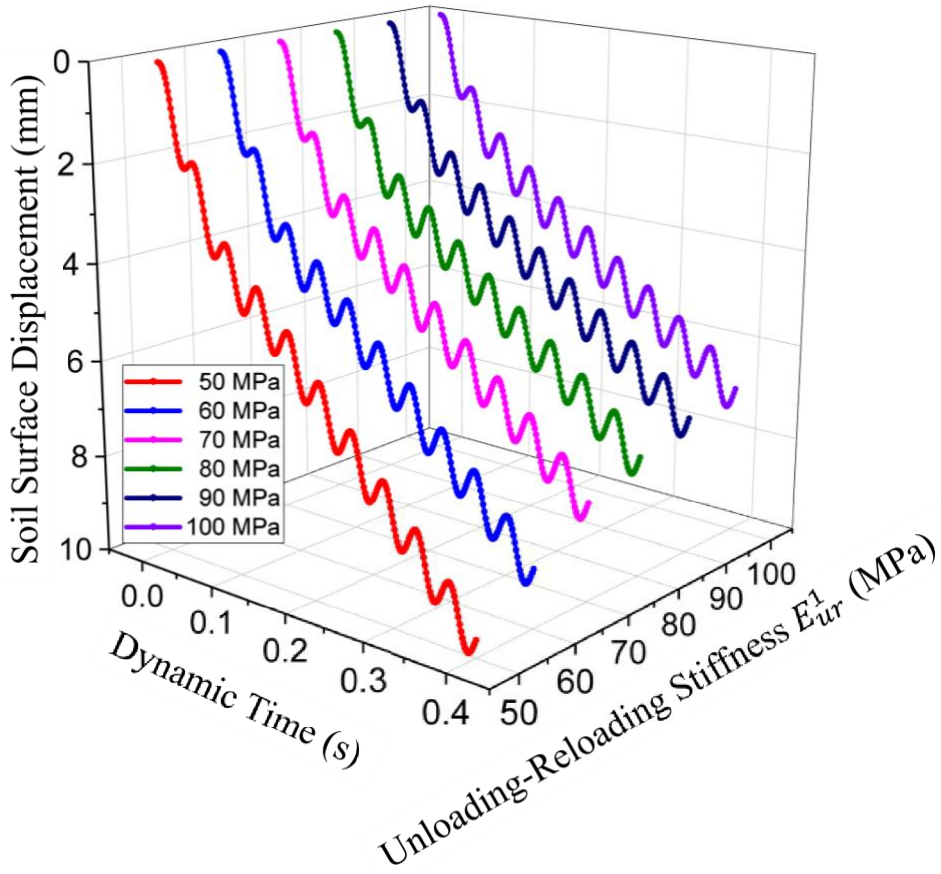

Figure 0.13 The vibratory roller vertical displacement versus different unloading-reloading soil stiffness of the top layer

Furthermore, the time history of the vertical soil settlement with variable E_{ur}^1 was studied to observe the influences of the unloading-reloading soil stiffness of the top layer on the interaction between soil and drum, with the magnitude of the E_{ur}^1 changed from 50 MPa to 100 MPa. Figure 6.13 demonstrated the vertical dynamic displacement beneath the drum under the condition of different magnitudes of the upper layer modulus, while considering a constant bottom layer modulus (110 MPa) and a constant excitation force (i.e. $f = 25$ Hz and $m_e e_e = 4$ kg. m). The observation showed that an increase in the upper layer modulus resulted in gradually

deceased accumulation of vertical surface settlement. Moreover, it can be found in numerical predictions that the optimum underlying soil compaction degree for the adopted soil was accomplished when the E_{ur}^{1} equals to 50 MPa, which explained that the particles of compacted material is hard to change when the modulus goes up, and it is consistent with observation made by Wang et al. (2021).

6.5. Summary

In modelling the double-layered three-dimensional finite element model, the isotropic hardening elastoplastic hysteretic model was conducted to predict the underlying soil modulus subjected to the vibratory compaction to explicitly capture the dissipative soil characteristics. Approximately 3,000 sets of 3D comprehensive numerical dataset composed of the roller acceleration response and ground characteristics is then applied to correlate the predicted soil stiffness by the newly proposed X-SVR approach. The adopted machine learning method incorporating Gaussian kernel and Generalised Gegenbauer kernel functions can reasonably predict the double-layered soil modulus during roller compaction.

Moreover, a further study was implemented to determine a suggested proportion of the selected training data to quickly develop the predictive model for achieving the real-time quality control to be used by site engineers. The critical E_{ur}^{1}/E_{ur}^{2} in the range 0.8 – 1.25 was observed beyond which the variations of the soil settlement were less significant. In addition, the influences of the relative modulus ratio, drum lengths and top layer modulus have influences on the soil surface dynamic displacement.

Chapter 7

Conclusions and Recommendations

7.1. General Conclusions

The key purpose of this study has been prediction of real-time layered soil stiffness during compaction operations. To establish a reliable relationship, the results of a large dataset, generated by the proposed finite element methods, were employed to investigate the interaction of vibratory roller and compacted soil. True scale three-dimensional models with the isotropic hardening elastoplastic hysteretic model were implemented to carefully simulate the boundary conditions and soil behaviour subjected to cyclic loading.

The finite element method can simulate the nonlinear behaviour of soil subjected to dynamic loading, particularly variations of soil stiffness and damping with the cyclic shear strain induced by the applied load. Therefore, the predictions of the numerical method can be utilised as potential guidance by practicing engineers and construction

teams on selecting the best roller vibration frequency and amplitude choice to achieve high-quality compaction. In addition, the developed numerical models are associated with varying roller characteristics and different soil properties to cover a comprehensive dataset, correlating the predicted soil modulus via an advanced machine learning approach. The outcomes of this study could be applied for practicing engineers to interpret roller drum acceleration data to estimate the level of compaction and ground stiffness during compaction.

7.2. Numerical Assessment of Impacts of Vibrating Roller Characteristics on Acceleration Response of Drum Used for IC

IC technology has emerged to provide uniform and high-quality compaction with real-time feedback. As an integrated mechanism, the magnitudes of roller parameters can be initiatively optimised to achieve the most efficient compaction effort. The characteristics of roller using a three-dimensional finite element simulation to represent the drum-soil interaction, while capturing soil hardening with small-strain stiffness variations was investigated in this chapter. The effects of the vibration of frequency and the amplitude as well as the weight of roller on soil compaction process and the roller response were analysed and discussed via the numerical modelling predictions.

The numerical predictions in this study has indicated that while the vibration frequency was changed between 24 Hz and 34 Hz for a given eccentric mass moment of $m_0 e_0$ = 2 kg.m, the optimal compaction was achieved when vibration frequency of 34 Hz was adopted. Indeed, this vibration frequency (i.e. 34 Hz) was the closest

to the natural first mode frequency of the effective soil deposit beneath the roller. Furthermore, the initial soil settlement due to self-weight of the roller was larger than the soil expansion after removal of roller since the loading stage comprised of both elastic and plastic components, whereas the unloading stage comprised of only elastic component.

The observations based on the conducted numerical modelling in this study exhibited that for the $m_0 e_0$ ranging from 1 to 4 kg.m, the maximum contact force was reached when $m_0 e_0$ = 4 kg. m, wherein the drum experienced the maximum acceleration with time. Thus, the largest final settlement was observed for $m_0 e_0$ = 4 kg. m, and it is not recommended to operate the roller under high eccentric mass moment in the finishing passes to avoid over-compaction. Furthermore, among rollers with different weights considered and for a given eccentric mass moment, the lightest roller experienced the highest acceleration and thus resulted in the largest final settlement due to the highest induced acceleration.

Although, the numerical predictions were comparable to the previously published data, further field experiments would assist to further assess the suitability of the established numerical model for interpretation of intelligent compaction measurements. The numerical results of this study suggest that the proposed 3D finite element model, which incorporates a nonlinear elastic-plastic soil model accounting for soil hardening and damping variations with shear strain, has the potential to simulate the soil-drum interaction behaviour, interpret intelligent compaction results, and optimise the compaction process. Indeed, this study can be used as a potential guidance by practitioners and construction professionals on selecting the best choice

of roller vibration frequency, eccentric mass moment and weight of roller during compaction process to achieve a high-quality final product.

7.3. Real-Time Determination of Sandy Soil Stiffness During Vibratory Compaction Incorporating Machine Learning Method for Intelligent Compaction

Many of the existing models employed simplified soil models as well as discrete dynamic analysis, while they cannot model hysteretic damping, stiffness degradation, cyclic loading and dissipative properties of the geomaterials. Since the continuum nature of the geomaterials cannot be explicitly described by mass-elastic spring-linear dashpot system often used in the literature, accurately back calculation of the real soil parameters during the compaction process remains a great challenge for practicing engineers.

This chapter presented details of a 3D numerical model to simulate the interaction between the vibratory roller drum and the soil beneath to be used for real-time back calculation of the soil stiffness. The effects of the amplitude, frequency and the weight of roller were assessed numerically and used to develop a comprehensive database for machine learning. The database was used to train the inverse solver using a newly proposed kernel-based X-SVR approach to predict the unloading/reloading modulus of underlying geomaterial according to the acceleration response of the drum during compaction.

More than a thousand 3D dynamic analyses were implemented to assess the influences of different drum parameters on the drum response and soil deformations

during compaction. The modified model adopted a typical drum size based on the practice in Australia, which was 2.1 m in length and 1.5 m in diameter, sitting on uniform soil. The characteristics of compacted soil used in the numerical modelling were very diverse, covering a wide range from loose to dense states of granular soils, corresponding to relative densities ranging from 20% to 90%.

The FEM predictions showed that the eccentric force amplitude greatly impacted the soil surface settlement right below the drum. Indeed, an eccentric mass m_0 rotating along the axle of the drum with an effective moment arm e_0 induced the centrifugal force corresponding to $m_0 e_0$ altering between 1 kg.m and 9 kg.m in this study. When the constant weight of the roller and operation frequency was applied, the excitation force was directly influenced by the eccentric mass amplitude. Therefore, a higher degree of compaction could be achieved by adopting a high eccentric mass moment. Considering the importance of the frequency of roller vibration in the compaction process, this study also investigated the effects of operation frequency in the common range of 20-35 Hz. The simulated results showed that the vibratory compaction could result in more compaction effort when the roller frequency was closer to the natural frequency of the soil.

The recently proposed kernel-based X-SVR method integrated with the IC system was proposed in this study for real-time extraction of underlying soil modulus during compaction process. The proposed method could predict the soil stiffness based on the X-SVR algorithm with the Gegenbauer kernel using the acceleration response of the drum and basic roller properties. Both training and testing unloading/reloading moduli (E_{ur}) obtained from the machine learning method correlated well with the 3D finite element predictions considering the nonlinear elastoplastic soil model and

dynamic soil-drum interaction. It is evident that the inverse solver developed in this study could predict the soil stiffness utilising the novel kernel-based X-SVR machine learning accurately and in the reasonably short time required for real-time quality control by practicing engineers.

7.4. Double-Layered Granular Soil Modulus Extraction for Intelligent Compaction Using X-SVR for Machine Learning Considering Soil-Structure Interaction

Approximately 3,000 sets of 3D numerical simulations were run and processed to capture the effects of different variables, namely the dynamic acceleration time-history response of the drum ($a_{rd} - t$ or $\ddot{z}_{rd}$- t), the excitation force of the roller (F_{EF}), the unloading-reloading modulus of the underlying layer (i.e. E_{ur}^{2}) and the ratio of roller mass to drum length ($R_{Ml} = M/l$), and the lift thickness of the compacted top layer (h_{top}). The extensive generated datasets were used for training and testing the X-SVR machine learning algorithm to validate the reliability of the correlated model.

The X-SVR method, in conjunction with Gaussian kernel and GGK functions, was adopted for real-time prediction of the double-layered soil stiffness during roller compaction. The proposed X-SVR with both kernels could predict the double-layered soil stiffness. Both training and predicting unloading-reloading modulus correlated well with adopted parameters in the 3D finite element model. In addition, a further study was conducted to analyse the proper selected training proportion to quickly and accurately establish a predictive model. It was observed that selection of 40% of data for training was the optimum in terms of satisfying both accuracy and minimised computational time. Furthermore, another study was conducted to

research the impacts of double-layer soil modulus ratio (E_{ur}^{1}/E_{ur}^{2}) of the soil settlement. A critical E_{ur}^{1}/E_{ur}^{2} in the range of 0.8 – 1.25 was observed beyond which the variations of the soil settlement was less significant. It was also observed that that for a given underlying soil condition, soil surface settlement z_d became less sensitive to vibration as modulus ratio increased. Furthermore, a reduction in the cumulative displacement was observed as a result of a decrease in the roller length and an increase in the upper layer modulus resulted in gradually deceased accumulation of vertical surface settlement.

7.5. Recommendations for Future Research

The current study used three-dimensional finite element models in conjunction with an advanced machine learning technique to instantaneously predict the soil modulus during compaction procedure. It should be noted that the total stress analysis was used, and the back-calculated soil stiffness is for the entire soil matrix representing the equivalent value, as it is in situ and in the total stress domain. The soil water content impacts the soil stiffness characteristics and the response of the roller. Thus, the soil stiffness should be determined based on the corresponding soil moisture content and total density on the site. To further expand this research study, the following recommendations can be made:

- During a long compaction process, the soil matric suction can change and in turn impact the soil stiffness. Thus, further research studies on capturing variations of soil suction and net stress during vibratory compaction are required.

- Response of unsaturated soils subjected to dynamic loading is complex, and it is recommended that more rigorous soil constitutive models for unsaturated soils should be adopted for future research studies; for example, advanced constitutive models such as the extended Barcelona model (BBMx) (Pedroso and Farias, 2011), Barcelona basic model (BBM) (Alonso et al., 1990) and SFG model (Sheng et al., 2008) can be some options to be explored in future research studies.
- Since both of single-layered and double-layered soil were adopted in the finite element modelling in this research study, the results can be used as a preliminary evaluation of the equivalent soil parameters below the roller. Further studies are required to obtain the individual soil layer stiffness values for multi-layered soil profiles.
- Since a large number of simulations and a thorough sensitivity analysis have been conducted to compensate the limitations of absence of the field work. A further field experiments are required, which would facilitate to verify the suitability of the established model for interpretation of intelligent compaction measurements.

References

Adam, D., Continuous compaction control (CCC) with vibratory rollers. Environmental geotechnics, 1997. 245-250.

Adam, D., 2007. Roller-integrated continuous compaction control (CCC). Design and construction of pavements and rail tracks: Geotechnical aspects and processed materials**,** 111.

Adam, D. & Kopf, F., 2004. Operational devices for compaction optimization and quality control (continuous compaction control & light falling weight device), na.

Adam, D. & Pistrol, J., 2016. Dynamic roller compaction for earthworks and roller-integrated continuous compaction control: State of the art overview and recent developments. Proc. Conferenze di Geotecnica di Torino, XXIV Ciclio**,** 1-41.

Aghayarzadeh, M., Khabbaz, H., Fatahi, B. & Terzaghi, S., 2020. Interpretation of dynamic pile load testing for open-ended tubular piles using finite-element method. International Journal of Geomechanics, 20**,** 04019169.

Alonso, E. E., Gens, A. & Josa, A., 1990. A constitutive model for partially saturated soils. Géotechnique, 40**,** 405-430.

Alshibli, K. A., Abu-Farsakh, M. & Seyman, E., 2005. Laboratory evaluation of the geogauge and light falling weight deflectometer as construction control tools. Journal of materials in civil engineering, 17**,** 560-569.

Alzabeebee, S., 2021. Influence of soil model complexity on the seismic response of shallow foundations. Geomech. Eng, 24**,** 193-203.

An, Z., Liu, T., Zhang, Z., Zhang, Q., Huangfu, Z. & Li, Q., 2020. Dynamic optimization of compaction process for rockfill materials. Automation in Construction, 110**,** 103038.

Anderegg, R., 1997. Nichtlineare schwingungen bei dynamischen bodenverdichtern. ETH Zurich.

Anderegg, R. & Kaufmann, K., 2004. Intelligent compaction with vibratory rollers: Feedback control systems in automatic compaction and compaction control. Transportation Research Record, 1868**,** 124-134.

Asif Imran, S., Barman, M., Commuri, S., Zaman, M. & Nazari, M., 2018. Artificial neural network–based intelligent compaction analyzer for real-time estimation of subgrade quality. International Journal of Geomechanics, 18**,** 04018048.

Asli, C., Feng, Z.-Q., Porcher, G. & Rincent, J.-J., 2012. Back-calculation of elastic modulus of soil and subgrade from portable falling weight deflectometer measurements. Engineering Structures, 34**,** 1-7.

Bai, Y. & Bai, Q., 2005. Subsea pipelines and risers, Elsevier.

Bard, E., 1993. Comportement des matériaux granulaires secs et à liant hydrocarboné. Châtenay-Malabry, Ecole centrale de Paris.

Beainy, F., Commuri, S. & Zaman, M., 2014. Dynamical response of vibratory rollers during the compaction of asphalt pavements. Journal of Engineering Mechanics, 140**,** 04014039.

Bekker, M. G., 1956. Theory of land locomotion.

Bekker, M. G., 1969. Introduction to terrain-vehicle systems. part i: The terrain. part ii: The vehicle. Michigan Univ Ann Arbor.

Bell, J., 1977. Compaction energy relationships of cohesive soils. Transportation Research Record, 641**,** 29-34.

Benz, T., 2007. Small-strain stiffness of soils and its numerical consequences. PhD Thesis

Benz, T., Vermeer, P. & Schwab, R., 2009. A small-strain overlay model. International journal for numerical and analytical methods in geomechanics, 33**,** 25-44.

Bhandari, S., Fatahi, B., Khabbaz, H., Lee, J., Xu, Z. & Zhong, J., 2022. Evaluating the Influence of Soil Plasticity on the Vibratory Roller—Soil Interaction for Intelligent Compaction. Advances in Transportation Geotechnics IV. Springer.

Briaud, J.-L. & Seo, J., 2003. Intelligent compaction: overview and research needs. Texas A&M University**,** 1-84.

Brinkgreve, R., Engin, E. & Engin, H. K., 2010a. Validation of empirical formulas to derive model parameters for sands. Numerical methods in geotechnical engineering. Hong Kong.

Brinkgreve, R., Engin, E. & Engin, H. K., 2010b. Validation of empirical formulas to derive model parameters for sands. Numerical methods in geotechnical engineering, 137**,** 142.

Brinkgreve, R., Kappert, M. & Bonnier, P., 2007. Hysteretic damping in a small-strain stiffness model. Proc. of Num. Mod. in Geomech., NUMOG X, Rhodes**,** 737-742.

Brinkgreve, R., Kumarswamy, S., Swolfs, W., Waterman, D., Chesaru, A. & Bonnier, P., 2016. PLAXIS 2016. PLAXIS bv, the Netherlands.

Buechler, S. R., Mustoe, G. G., Berger, J. R. & Mooney, M. A., 2012. Understanding the soil contact problem for the LWD and static drum roller by using the DEM. Journal of engineering mechanics, 138**,** 124-132.

Burland, J., 1989. 'Small is beautiful'–the stiffness of soils at small strains: Ninth Laurits Bjerrum Memorial Lecture. Canadian Geotechnical Journal, 26**,** 499-516.

Cao, L., Zhou, J., Li, T., Chen, F. & Dong, Z., 2021. Influence of roller-related factors on compaction meter value and its prediction utilizing artificial neural network. Construction and Building Materials, 268**,** 121078.

Cao, Y.-W., Liang, N.-X., Qin, M. & Lu, Z.-F., 2010. Research on the correlation between vibration acceleration of roller and compaction degree of subgrade soil. ICCTP 2010: Integrated Transportation Systems: Green, Intelligent, Reliable.

Carrasco, C., Terado, C. & Wang, H., 2014. Numerical simulation of intelligent compaction technology for construction quality control. Rutgers University. Center for Advanced Infrastructure and Transportation.

Chang, G. & Gallivan, V. L., 2011. Accelerated implementation of intelligent compaction technology for embankment subgrade soils, aggregate base, and asphalt pavement materials. United States. Federal Highway Administration.

Cheng, K., Lu, Z., Wei, Y., Shi, Y. & Zhou, Y., 2017. Mixed kernel function support vector regression for global sensitivity analysis. Mechanical Systems and Signal Processing, 96**,** 201-214.

Costigliola, R. M., Mancuso, C., Pagano, L. & Silvestri, F., 2022. Prediction of permanent settlements of an upstream faced earth dam. Computers and Geotechnics, 144**,** 104594.

Cundall, P. A., A computer model for simulating progressive, large-scale movement in blocky rock system. Proceedings of the International Symposium on Rock Mechanics, 1971, 1971.

Dos Santos, J. & Correia, A. G., Reference threshold shear strain of soil. Its application to obtain an unique strain-dependent shear modulus curve for soil. Proceedings of the Fifteenth International Conference on Soil Mechanics and Geotechnical Engineering, Istanbul, Turkey, 27-31 August 2001. Volumes 1-3, 2001. AA Balkema, 267-270.

Drucker, H., Burges, C. J., Kaufman, L., Smola, A. & Vapnik, V., 1996. Support vector regression machines. Adv. Neural. Inf Process Syst., 9.

Dunbar, M., Murray, J. M., Cysique, L. A., Brew, B. J. & Jeyakumar, V., 2010. Simultaneous classification and feature selection via convex quadratic programming with application to HIV-associated neurocognitive disorder assessment. European journal of operational research, 206**,** 470-478.

Erdmann, P. & Adam, D., Numerical simulation of dynamic soil compaction with vibratory compaction equipment. Proceedings of the XV Danube—European Conference on Geotechnical Engineering (DECGE 2014), 2014. 243-248.

Facas, N. W., Van Susante, P. J. & Mooney, M. A., 2010. Influence of rocking motion on vibratory roller-based measurement of soil stiffness. Journal of engineering mechanics, 136**,** 898-905.

Fatahi, B., Basack, S., Ryan, P., Zhou, W.-H. & Khabbaz, H., 2014. Performance of laterally loaded piles considering soil and interface parameters. Geomechanics and Engineering.

Fatahi, B., Huang, B., Yeganeh, N., Terzaghi, S. & Banerjee, S., 2020. Three-dimensional simulation of seismic slope–foundation–structure interaction for buildings near shallow slopes. International Journal of Geomechanics, 20**,** 04019140.

Fatahi, B., Van Nguyen, Q., Xu, R. & Sun, W.-J., 2018. Three-dimensional response of neighboring buildings sitting on pile foundations to seismic pounding. International Journal of Geomechanics, 18**,** 04018007.

Fathi, A., 2020. Extracting mechanical properties of compacted geomaterials using intelligent compaction technology. The University of Texas at El Paso.

Fathi, A., Mazari, M., Saghafi, M., Hosseini, A. & Kumar, S., 2019. Parametric study of pavement deterioration using machine learning algorithms. Airfield and highway pavements, 2019**,** 31-41.

Fathi, A., Tirado, C., Gholamy, A., Lemus, L., Mazari, M. & Nazarian, S., 2018. Consideration of depth of influence in implementation of intelligent compaction in earthwork quality management.

Fathi, A., Tirado, C., Rocha, S., Mazari, M. & Nazarian, S., 2021a. Assessing depth of influence of intelligent compaction rollers by integrating laboratory testing and field measurements. Transportation Geotechnics, 28**,** 100509.

Fathi, A., Tirado, C., Rocha, S., Mazari, M. & Nazarian, S., 2021b. A Machine-Learning Approach for Extracting Modulus of Compacted Unbound Aggregate Base and Subgrade Materials Using Intelligent Compaction Technology. Infrastructures, 6**,** 142.

Fathi, A., Tirado, C., Rocha, S., Mazari, M. & Nazarian, S., 2022. A Stress–Dependent Approach for Estimation of Drum–Soil Contact Area. Advances in Transportation Geotechnics IV. Springer.

Feng, J., Liu, L., Wu, D., Li, G., Beer, M. & Gao, W., 2019. Dynamic reliability analysis using the extended support vector regression (X-SVR). Mechanical Systems and Signal Processing, 126**,** 368-391.

Fleming, P. R., Frost, M. W. & Lambert, J. P., 2007. Review of lightweight deflectometer for routine in situ assessment of pavement material stiffness. Transportation Research Record, 2004**,** 80-87.

Floss, R., Bräu, G. & Gahbauer, M., 1991. Dynamische Verdichtungsprüfung bei Erd-und Straßenbauten. Forschung Straßenbau und Straßenverkehrstechnik.

Forssblad, L., Compaction meter on vibrating rollers for improved compaction control. Proceedings of International Conference on Compaction, 1980. 541-546.

Gallivan, V. L., Chang, G. K. & Horan, D. R., 2011. Intelligent compaction for improving roadway construction. Emerging Technologies for Material, Design, Rehabilitation, and Inspection of Roadway Pavements.

Gomes Correia, A., Cortez, P., Tinoco, J. & Marques, R., 2013. Artificial intelligence applications in transportation geotechnics. Geotechnical and Geological Engineering, 31**,** 861-879.

Gong, C., Ding, W. & Xie, D., 2020. Twin EPB tunneling-induced deformation and assessment of a historical masonry building on Shanghai soft clay. Tunnelling and Underground Space Technology, 98**,** 103300.

Han, B., Zdravkovic, L., Kontoe, S. & Taborda, D. M., 2016. Numerical investigation of the response of the Yele rockfill dam during the 2008 Wenchuan earthquake. Soil Dynamics and Earthquake Engineering, 88**,** 124-142.

Hardin, B. O. & Drnevich, V. P., 1972. Shear modulus and damping in soils: design equations and curves. Journal of the Soil mechanics and Foundations Division, 98**,** 667-692.

He, S. & Zhou, W., Research on the settlement prediction of immersed tunnel based on the physics-informed machine learning. Proceedings of The 25th Annual Conference of HKSTAM 2022 The 17th Jiangsu–Hong Kong Forum on Mechanics and Its Application, 2022. 63.

Hejazi, Y., Dias, D. & Kastner, R., 2008. Impact of constitutive models on the numerical analysis of underground constructions. Acta Geotechnica, 3**,** 251-258.

Herrera, C., Costa, P. A. & Caicedo, B., 2018. Numerical modelling and inverse analysis of continuous compaction control. Transportation Geotechnics, 17**,** 165-177.

Hertz, H., 1882. Über die Berührung fester elastischer Körper. Journal für die reine und angewandte Mathematik, 92**,** 22.

Ho, L., Fatahi, B. & Khabbaz, H., 2018. Analytical solution to one-dimensional consolidation in unsaturated soil deposit incorporating time-dependent diurnal temperature variation. International Journal of Geomechanics, 18**,** 04018029.

Hofmann, T., Schölkopf, B. & Smola, A. J., 2008. Kernel methods in machine learning. The annals of statistics, 36**,** 1171-1220.

Hu, W., 2018. Evaluation of intelligent compaction technology in asphalt pavement construction and laboratory compaction.

Hu, W., Huang, B., Shu, X. & Woods, M., 2017. Utilising intelligent compaction meter values to evaluate construction quality of asphalt pavement layers. Road Materials and Pavement Design, 18**,** 980-991.

Hu, W., Jia, X., Zhu, X., Gong, H., Xue, G. & Huang, B., 2019. Investigating key factors of intelligent compaction for asphalt paving: A comparative case study. Construction and Building Materials, 229**,** 116876.

Hua, T., Yang, X., Yao, Q. & Li, H., 2018. Assessment of real-time compaction quality test indexes for rockfill material based on roller vibratory acceleration analysis. Advances in Materials Science and Engineering, 2018.

Huynh, Q. T., Lai, V. Q., Boonyatee, T. & Keawsawasvong, S., 2022. Verification of soil parameters of hardening soil model with small-strain stiffness for deep excavations in medium dense sand in Ho Chi Minh City, Vietnam. Innovative Infrastructure Solutions, 7**,** 1-20.

Jin, Y.-F., Yin, Z.-Y., Zhou, W.-H. & Huang, H.-W., 2019. Multi-objective optimization-based updating of predictions during excavation. Engineering Applications of Artificial Intelligence, 78**,** 102-123.

Kawa, M., Puła, W. & Truty, A., 2021. Probabilistic analysis of the diaphragm wall using the hardening soil-small (HSs) model. Engineering Structures, 232**,** 111869.

Kenneally, B., Musimbi, O. M., Wang, J. & Mooney, M. A., 2015. Finite element analysis of vibratory roller response on layered soil systems. Computers and Geotechnics, 67**,** 73-82.

Kim, K., 2010. Numerical Simulation of Impact Rollers for Estimating the Influence Depth of Soil Compaction. MASTER OF SCIENCE, Texas A&M University.

Kim, M., Tutumluer, E. & Kwon, J., 2009. Nonlinear pavement foundation modeling for three-dimensional finite-element analysis of flexible pavements. International Journal of Geomechanics, 9**,** 195-208.

Kontoe, S., Zdravkovic, L., Potts, D. & Menkiti, C., 2011. On the relative merits of simple and advanced constitutive models in dynamic analysis of tunnels. Géotechnique, 61**,** 815-829.

Krober, W., Floss, E. R. & Wallrath, W., Dynamic soil stiffness as quality criterion for soil compaction. Geotechnics for roads, rail tracks and earth structures, 2001. 189-199.

Kumar, S. A., Aldouri, R., Nazarian, S. & Si, J., 2016. Accelerated assessment of quality of compacted geomaterials with intelligent compaction technology. Construction and Building Materials, 113**,** 824-834.

Kuwano, R., 2018. Advanced laboratory stress-strain testing of geomaterials, Routledge.

Lanzano, G., Visone, C., Bilotta, E. & Santucci De Magistris, F., 2016. Experimental assessment of the stress–strain behaviour of Leighton Buzzard sand for the calibration of a constitutive model. Geotechnical and Geological Engineering, 34**,** 991-1012.

Lavin, P., 2003. Asphalt pavements: a practical guide to design, production and maintenance for engineers and architects, CRC Press.

Li, J., Lu, L., Zhou, Z. & Xu, L., Dynamic modeling simulation and analysis of amplitude frequency characteristics on Tandem-Heavy oscillating rollers. IOP Conference Series: Materials Science and Engineering, 2018. IOP Publishing, 032040.

Li, S. & Hu, C., Study on dynamic model of vibratory roller-soil system. IOP conference series: earth and environmental science, 2018. IOP Publishing, 012187.

Li, S. & Su, Y., 2014. Three Dimensional Finite Element Simulation of Vibratory Roller Impact on Subgrade Settlement. Electronic Journal of Geotechnical Engineering, 19**,** 6193-6200.

Lin, Z., Ji, K., Kang, M., Leng, X. & Zou, H., 2017. Deep convolutional highway unit network for SAR target classification with limited labeled training data. IEEE Geoscience and Remote Sensing Letters, 14**,** 1091-1095.

Liu, D., Lin, M. & Li, S., 2016. Real-time quality monitoring and control of highway compaction. Automation in Construction, 62**,** 114-123.

Liu, H., Zou, D. & Liu, J., 2014. Constitutive modeling of dense gravelly soils subjected to cyclic loading. International Journal for Numerical and Analytical Methods in Geomechanics, 38**,** 1503-1518.

Lundberg, V. G., 1939. Elastische berührung zweier halbräume. Forschung auf dem Gebiet des Ingenieurwesens A, 10**,** 201-211.

Lysmer, J. & Kuhlemeyer, R. L., 1969. Finite dynamic model for infinite media. Journal of the engineering mechanics division, 95**,** 859-877.

Ma, Q. & Shi, L.-W., 2022. Dynamic Response of Two-Dimensional Double-Layered Unsaturated Soil Foundations Under a Strip Load. Journal of Vibration Engineering & Technologies, 10**,** 1221-1233.

Ma, Y., Wang, Z. & Zhang, Y., 2021. Research on numerical simulation of intelligent compaction of subgrade secondary development based on ABAQUS finite element. J. Civ. Eng., 9**,** 1424-1437.

Mangasarian, O. L. & Musicant, D. R., 2001. Lagrangian support vector machines. Journal of Machine Learning Research, 1**,** 161-177.

Masad, E., Scarpas, A., Rajagopal, K. R., Kassem, E., Koneru, S. & Kasbergen, C., 2016. Finite element modelling of field compaction of hot mix asphalt. Part II: Applications. International Journal of Pavement Engineering, 17**,** 24-38.

Mccabe, B. A. & Sheil, B. B., 2015. Pile group settlement estimation: suitability of nonlinear. International Journal of Geomechanics, 13**,** 3.

Micaelo, R., Azevedo, M., Azevedo, N. & Ribeiro, J., 2010. HMA Compaction Study: Two Different Approaches.

Moghaddam, V. H. & Hamidzadeh, J., 2016. New Hermite orthogonal polynomial kernel and combined kernels in support vector machine classifier. Pattern Recognition, 60**,** 921-935.

Mooney, M. & Adam, D., 2007. Vibratory roller integrated measurement of earthwork compaction: An overview. 7th FMGM 2007: Field Measurements in Geomechanics**,** 1-12.

Mooney, M. A., 2010. Intelligent soil compaction systems, Transportation Research Board.

Mooney, M. A. & Facas, N. W., 2013. Extraction of Layer Properties from Intelligent compaction data.

Mooney, M. A. & Rinehart, R. V., 2009. In situ soil response to vibratory loading and its relationship to roller-measured soil stiffness. Journal of geotechnical and geoenvironmental engineering, 135**,** 1022-1031.

Mooney, R. R. & Ma, 2009. Measurement depth of vibratory roller-measured soil stiffness. Géotechnique, 59**,** 609-619.

Musimbi, O., Rinehart, R. & Mooney, M., 2010. Comparison of measured and BEM computed contact area between roller drum and layered soil. GeoFlorida 2010: Advances in Analysis, Modeling & Design.

Nazarian, S., A. Fathi, C. Tirado, V. Kreinovich, S. Rocha, and M. Mazari, 2020. Evaluating Mechanical Properties of Earth Material During Intelligent Compaction. Transportation Research Board.

Noh, G. & Bathe, K.-J., 2019. For direct time integrations: A comparison of the Newmark and ρ∞-Bathe schemes. Computers & Structures, 225**,** 106079.

Ooi, P. S., Archilla, A. R. & Sandefur, K. G., 2004. Resilient modulus models for compacted cohesive soils. Transportation research record, 1874**,** 115-124.

Ozer, S., Chen, C. H. & Cirpan, H. A., 2011. A set of new Chebyshev kernel functions for support vector machine pattern classification. Pattern Recognition, 44**,** 1435-1447.

Paulmichl, I., Adam, C. & Adam, D., 2019. Analytical modeling of the stick-slip motion of an oscillation drum. Acta Mechanica, 230**,** 3103-3126.

Pedroso, D. M. & Farias, M. M., 2011. Extended Barcelona basic model for unsaturated soils under cyclic loadings. Computers and Geotechnics, 38**,** 731-740.

Pei, T. & Yang, X., 2018. Compaction-induced stress in geosynthetic-reinforced granular base course–A discrete element model. Journal of Rock Mechanics and Geotechnical Engineering, 10**,** 669-677.

Pietzsch, D. & Poppy, W., 1992. Simulation of soil compaction with vibratory rollers. Journal of Terramechanics, 29**,** 585-597.

Pistrol, J., Adam, D., Villwock, S., Völkel, W. & Kopf, F., 2015. Movement of vibrating and oscillating drums and its influence on soil compaction.

Pistrol, J., Kopf, F., Adam, D., Villwock, S. & Völkel, W., Ambient vibration of oscillating and vibrating rollers. Proceedings of the Vienna congress on recent advances in earthquake engineering and structural dynamics, 2013. 514-521.

Ranasinghe, R., Jaksa, M., Kuo, Y. & Nejad, F. P., 2017. Application of artificial neural networks for predicting the impact of rolling dynamic compaction using dynamic cone penetrometer test results. Journal of Rock Mechanics and Geotechnical Engineering, 9**,** 340-349.

Rao, S. S., 2017. The finite element method in engineering, Butterworth-heinemann.

Rinehart, R. V. & Mooney, M. A., 2008. Instrumentation of a roller compactor to monitor vibration behavior during earthwork compaction. Automation in Construction, 17**,** 144-150.

Roberts, F. L., Kandhal, P. S., Brown, E. R., Lee, D.-Y. & Kennedy, T. W., 1991. Hot mix asphalt materials, mixture design and construction.

Ryden, N. & Mooney, M. A., 2009. Analysis of surface waves from the light weight deflectometer. Soil Dynamics and Earthquake Engineering, 29**,** 1134-1142.

Saberi, M., Annan, C.-D. & Konrad, J.-M., 2020. Three-dimensional constitutive model for cyclic behavior of soil-structure interfaces. Soil Dynamics and Earthquake Engineering, 134**,** 106162.

Sandström, Å., 1994. Numerical simulation of a vibratory roller on cohesionless soil. Geodynamik Report, Stockholm**,** 22.

Schanz, T., Vermeer, P. & Bonnier, P. G., 1999. The hardening soil model: formulation and verification. Beyond 2000 in computational geotechnics. Routledge.

Scherocman, J. A., Rakowski, S. & Uchiyama, K., Intelligent compaction, does it exist? Fifty-Second Annual Conference of the Canadian Technical Asphalt Association (CTAA) Canadian Technical Asphalt Association, 2007.

Scholkopf, B., Mika, S., Burges, C. J., Knirsch, P., Muller, K.-R., Ratsch, G. & Smola, A. J., 1999. Input space versus feature space in kernel-based methods. IEEE transactions on neural networks, 10**,** 1000-1017.

Schölkopf, B., Smola, A. J. & Bach, F., 2002. Learning with kernels: support vector machines, regularization, optimization, and beyond, MIT press.

Scott, B. T., Jaksa, M. B. & Mitchell, P. W., 2020. Influence of towing speed on effectiveness of rolling dynamic compaction. Journal of Rock Mechanics and Geotechnical Engineering, 12**,** 126-134.

Sharma, V. & Kumar, A., 2018. Behavior of ring footing resting on reinforced sand subjected to eccentric-inclined loading. Journal of Rock Mechanics and Geotechnical Engineering, 10**,** 347-357.

Sheng, D., Fredlund, D. G. & Gens, A., 2008. A new modelling approach for unsaturated soils using independent stress variables. Canadian Geotechnical Journal, 45**,** 511-534.

Siekmeier, J. A., Young, D. & Beberg, D., 2000. Comparison of the dynamic cone penetrometer with other tests during subgrade and granular base characterization in Minnesota. ASTM Special Technical Publication, 1375**,** 175-188.

Skels, P. & Bondars, K., 2017. Applicability of small strain stiffness parameters for pile settlement calculation. Procedia Engineering, 172**,** 999-1006.

Sluys, L. J., 1994. Wave propagation, localisation and dispersion in softening solids.

Smith, W. & Peng, H., 2013. Modeling of wheel–soil interaction over rough terrain using the discrete element method. Journal of Terramechanics, 50**,** 277-287.

Snoek, J., Larochelle, H. & Adams, R. P., 2012. Practical bayesian optimization of machine learning algorithms. Advances in neural information processing systems, 25.

Stein, E. M. & Weiss, G., 2016. Introduction to Fourier Analysis on Euclidean Spaces (PMS-32), Volume 32. Introduction to Fourier Analysis on Euclidean Spaces (PMS-32), Volume 32. Princeton university press.

Tavarez, F. A. & Plesha, M. E., 2007. Discrete element method for modelling solid and particulate materials. International journal for numerical methods in engineering, 70**,** 379-404.

Tehrani, F. S., 2009. An investigation of continuous compaction control systems, University of Delaware.

Thurner, H., The compactometer principle: Contribution to the discussion in Session IV. Proc., Intl. Conf. on Compaction, 1980.

Thurner, H. & Sandstrom, A., Continuous compaction control, CCC. European Workshop Compaction of Soils and Granular Materials, Presses Ponts et Chaussées, Paris, France, 2000. 237-246.

Ti, K. S., Huat, B. B. K., Noorzaei, J., Jaafar, M. D. S. & Sew, G. S., 2009. A Review of Basic Soil Constitutive Models for Geotechnical Application. Electronic Journal of Geotechnical Engineering, 14.

Torres, A. & Arasteh, M., 2017. Intelligent Compaction Measurement Values (ICMV)-A Road Map. Technical Brief, Fhwa-Hif-17-046.

Uzan, J., Witczak, M. W., Scullion, T., & Lytton, R. L. 1992. Development and validation of realistic pavement response models. International Conference on Asphalt Pavements, Nottingham, United Kingdom, 7th, 1992. 1.

Van Susante, P. J. & Mooney, M. A., 2008. Capturing nonlinear vibratory roller compactor behavior through lumped parameter modeling. Journal of engineering mechanics, 134**,** 684-693.

Vapnik, V., 1999. The nature of statistical learning theory, Springer science & business media.

Viggiani, G. & Atkinson, J., 1995. Stiffness of fine-grained soil at very small strains. Géotechnique, 45**,** 249-265.

Von Quintus, H. L., 2010. Evaluation of intelligent compaction technology for densification of roadway subgrades and structural layers, Wisconsin Highway Research Program.

Wang, L., Zhang, B., Wang, D. & Yue, Z., 2007. Fundamental mechanics of asphalt compaction through FEM and DEM modeling. Analysis of asphalt pavement materials and systems: Engineering methods.

Wang, L., Zhu, J. & Zou, H., 2006. The doubly regularized support vector machine. Statistica Sinica**,** 589-615.

Wang, Q., Feng, Y., Wu, D., Li, G., Liu, Z. & Gao, W., 2022a. Polymorphic uncertainty quantification for engineering structures via a hyperplane modelling technique. Computer Methods in Applied Mechanics and Engineering, 398**,** 115250.

Wang, Q., Li, Q., Wu, D., Yu, Y., Tin-Loi, F., Ma, J. & Gao, W., 2020. Machine learning aided static structural reliability analysis for functionally graded frame structures. Applied Mathematical Modelling, 78**,** 792-815.

Wang, Q., Wu, D., Tin-Loi, F. & Gao, W., 2019. Machine learning aided stochastic structural free vibration analysis for functionally graded bar-type structures. Thin-Walled Structures, 144**,** 106315.

Wang, S.-P., Dan, H.-C., Li, L., Liu, X. & Zhang, Z., 2021. Dynamic response of asphalt pavement under vibration rolling load: theory and calibration. Soil Dynamics and Earthquake Engineering, 143**,** 106633.

Wang, X., Dong, X., Zhang, Z., Zhang, J., Ma, G. & Yang, X., 2022b. Compaction quality evaluation of subgrade based on soil characteristics assessment using machine learning. Transportation Geotechnics, 32**,** 100703.

Wehnert, M. & Vermeer, P., 2004. Numerical analyses of load tests on bored piles. Numerical methods in geomechanics–NUMOG IX**,** 505-511.

Wersäll, C. & Larsson, S., Influence of force ratio and frequency on vibratory surface compaction. 3rd International Conference on Geotechnics for Sustainable Infrastructure Development, Hanoi, 24th-25th Nov 2016, Vietnam, 2016.

Wersäll, C., Nordfelt, I. & Larsson, S., 2017. Soil compaction by vibratory roller with variable frequency. Geotechnique, 67**,** 272-278.

Wersäll, C., Nordfelt, I. & Larsson, S., 2020. Roller compaction of rock-fill with automatic frequency control. Proceedings of the Institution of Civil Engineers-Geotechnical Engineering, 173**,** 339-347.

White, D. J., Jaselskis, E. J., Schaefer, V. R. & Cackler, E. T., 2005. Real-time compaction monitoring in cohesive soils from machine response. Transportation research record, 1936**,** 172-180.

White, D. J. & Vennapusa, P. K., 2010. A review of roller-integrated compaction monitoring technologies for earthworks. Final Report ER10-04**,** 1-36.

Wu, C.-L., Ma, X.-P. & Fang, T., 2006. A complementary note on Gegenbauer polynomial approximation for random response problem of stochastic structure. Probabilistic engineering mechanics, 21**,** 410-419.

Wu, W., 1990. The behaviour of very loose sand in the triaxial compression test: Discussion. Canadian Geotechnical Journal, 27**,** 159-162.

Xu, Q. & Chang, G. K., 2013. Evaluation of intelligent compaction for asphalt materials. Automation in Construction, 30**,** 104-112.

Xu, Q., Chang, G. K. & Gallivan, V. L., 2012. Development of a systematic method for intelligent compaction data analysis and management. Construction and Building Materials, 37**,** 470-480.

Xu, Z., Khabbaz, H., Fatahi, B., Lee, J. & Bhandari, S., 2022a. Numerical Assessment of Impacts of Vibrating Roller Characteristics on Acceleration Response of Drum Used for Intelligent Compaction. Advances in Transportation Geotechnics IV. Springer.

Xu, Z., Khabbaz, H., Fatahi, B. & Wu, D., 2022b. Real-time determination of sandy soil stiffness during vibratory compaction incorporating machine learning method for intelligent compaction. Journal of Rock Mechanics and Geotechnical Engineering, 14**,** 1609-1625.

Ye, N., Sun, R., Liu, Y. & Cao, L., Support vector machine with orthogonal Chebyshev kernel. 18th International Conference on Pattern Recognition (ICPR'06), 2006. IEEE, 752-755.

Yesuf, G. Y., 2014. Influence of Subsoil Conditionson the Design and Performance of Flexible Pavements.

Yin, S., Yu, D., Yin, H. & Xia, B., 2016. Interval and random analysis for structure–acoustic systems with large uncertain-but-bounded parameters. Computer Methods in Applied Mechanics and Engineering, 305**,** 910-935.

Yoo, T.-S. & Selig, E. T., 1979. Dynamics of vibratory-roller compaction. Journal of the Geotechnical Engineering Division, 105**,** 1211-1231.

Yoo, T. & Selig, E., New concepts for vibratory compaction of soil. Proc., Int. Conf. on Compaction, 1980. ENPC, 703-707.

Zainudin, S., Jasim, D. S. & Bakar, A. A., 2016. Comparative analysis of data mining techniques for Malaysian rainfall prediction. Int. J. Adv. Sci. Eng. Inf. Technol, 6**,** 1148-1153.

Zhang, F. & Kimura, M., 2002. Numerical prediction of the dynamic behaviors of an RC group-pile foundation. Soils and Foundations, 42**,** 77-92.

Zhang, Q., Liu, T., Zhang, Z., Huangfu, Z., Li, Q. & An, Z., 2019. Compaction quality assessment of rockfill materials using roller-integrated acoustic wave detection technique. Automation in Construction, 97**,** 110-121.

Zhang, W., Khan, A. R., Yoon, S., Lee, J., Zhang, R. & Zeng, K., 2021. Investigation of the correlations between the field pavement in-place density and the intelligent compaction measure value (ICMV) of asphalt layers. Construction and Building Materials, 292**,** 123439.

Zhu, X., Bai, S., Xue, G., Yang, J., Cai, Y., Hu, W., Jia, X. & Huang, B., 2018. Assessment of compaction quality of multi-layer pavement structure based on intelligent compaction technology. Construction and Building Materials, 161**,** 316-329.